© 2020 by Jonathan M. Wang. All rights reserved.

IGNITION AND HYDRODYNAMIC EJECTIONS BY LASER-INDUCED BREAKDOWNS

BY

JONATHAN M. WANG

DISSERTATION

Submitted in partial fulfillment of the requirements
for the degree of Doctor of Philosophy in Theoretical and Applied Mechanics
in the Graduate College of the
University of Illinois at Urbana–Champaign, 2020

Urbana, Illinois

Doctoral Committee

Professor Jonathan B. Freund, Chair and Director of Research
Associate Professor Marco Panesi
Assistant Professor Kelly A. Stephani
Professor Sascha Hilgenfeldt

Abstract

A focused laser can cause optical breakdown of gas, forming a high-temperature plasma that rapidly absorbs laser energy. As a source of heat and radical species, laser-based energy deposition can be an effective ignition source, and its relative versatility and precision make it an attractive alternative to conventional ignition methods. Understanding of the breakdown-induced flow, its dependence on details of the plasma generation, and how it can alter and tailor ignition and subsequent flame growth will facilitate incorporation into engineering applications such as internal combustion engines and supersonic propulsion systems.

Direct numerical simulation with five gas models, in conjunction with an energy-deposition model that reproduces key experimental observations, are used to analyze the post-breakdown flow and ignition dynamics by direct numerical simulation. A perfect-gas model shows that the breakdown-induced flow occurs primarily by hydrodynamic processes that explains a curious experimental observation: hot gas ejects from the breakdown region along the laser axis, traveling up to distances several times the plasma kernel size, and can reverse direction for small changes in breakdown conditions. Vorticity-generating mechanisms are quantified and shown to be sensitive to asymmetries in the kernel's hydrodynamic expansion, and changes to the kernel geometry can lead to the observed ejection or its reversal. Even subtle alterations — such as a 20% increase in aspect ratio — can lead to qualitative differences in the vorticity dynamics and ultimate flow pattern.

Rich flow phenomenology is caused by dual-pulse configurations, and mechanisms by which the ejection can be disrupted or enhanced by the second deposition are analyzed. For simultaneous depositions, vorticity generation can be suppressed by even a small secondary kernel, preventing the ejection from forming, whereas for time-delayed depositions, asymmetry in the kernel expansion can amplify ejection or precipitate its reversal. The time delay and spatial offset between two depositions are controlled to enhance the dispersal of hot gas, which is shown to increase the burning rate of a nascent hydrogen flame.

This sensitivity of the breakdown-induced flow to energy deposition warrants an assessment of nonequilibrium-

plasma effects on the hydrodynamics, which are analyzed using a two-temperature argon-plasma model. We show that electron recombination can occur on the time scale of the plasma's hydrodynamic expansion and provide an avenue for formation energy of ions to be converted to mechanical work on the gas, thereby enhancing the expansion and altering the vorticity distribution.

Finally, we analyze how these flow mechanisms can couple with ignition of a fuel–oxidizer interface. We first consider detailed hydrogen-combustion model, and results are generalized to heavy fuels with a reduced model. Heat release by radical recombination is a primary mechanism by which the ejected gas maintains temperature ignition threshold as it is transported towards fuel. For depositions close to a fuel lighter than oxygen, the expanding kernel interacts with the mixture density mismatch to produce a flow that repels hot gas away, in some cases leading to ignition failure. This flow pattern is absent for heavy fuels, which more readily ignite in this nonpremixed configuration due to suppression of the adverse flow response.

Acknowledgments

My primary thanks goes to my advisor Professor Jonathan Freund who — with his incisive and challenging questions, wealth of knowledge, insightful yet measured guidance, and genuine enthusiasm — has enabled me to complete this work. I will miss our "bonus-question" chats.

I would like to thank the defense committee, Professors Sascha Hilgenfeldt, Marco Panesi, and Kelly Stephani, for their time and critical eye in reviewing this dissertation.

I am grateful to members of Professor Greg Elliott's research group, including Jonathan Retter, Matt Koll, and Munetake Nishihara, for providing invaluable experimental data.

Fellow lab-mates in Prof. Freund's research group and XPACC — including David Buchta, Jonathan MacArt, Esteban Cisneros-Garibay, Seung Whan Chung, Wyatt Hagen, Andrea Alberti, and Joel Krehbiel — have played an important role in this work, as they were always willing to offer their time and perspective on any particularly sticky question I had. I am grateful for both their companionship and our many fruitful discussions.

I would also like to thank my friend Aaron Kitchin for our less-than-rigorous scientific escapades that, I'd like to think, has inspired my research in some indirect way.

This work would not have been possible without the support of my parents, Shouping and Jane, and my always-curious brother Dennis. I cherished our time together and our weekly calls, which have sustained me in ways that they may not realize. Lastly, the unwavering support and optimism of my fiancée Meghna has had a profound impact on my ability to complete this work, as she was able to summon happiness and encouragement even on our most stressful days.

This material is based in part upon work supported by the Department of Energy, National Nuclear Security Administration, under Award Number DE-NA0002374.

To my parents.

Contents

List of Figures

List of Tables

Chapter 1

Introduction

1.1 Laser-induced breakdown

A focused laser pulse with sufficient energy can cause optical breakdown of a gas and produce a high-temperature volume of ionized species [1]. The process is initiated with the formation of free electrons by photon impact, triggering a cascade process by which the gas, which is otherwise nearly transparent to the laser light, becomes highly absorptive and heats rapidly [2, 3]. By the end of the laser pulse, approximately 10 ns in duration and depositing 10–100 mJ of energy for the applications considered, the plasma kernel is typically 1–4 mm long and 0.2–1 mm wide and appears axisymmetric about the laser axis but often asymmetric in the direction of the laser [4, 5, 6]. The kernel is estimated to attain temperatures in the range 10^4–10^5 K [7, 8]. This high-pressure gas expands and produces a strong shock wave that decouples from the kernel after approximately 1 μs and decays to a spherical acoustic wave as it propagates into the ambient fluid. The expansion also induces a complex flow in the breakdown region that mixes the surrounding gas. In some cases, hot gas ejects from the laser-focal region 10–100 μs after breakdown and propagates along the laser axis, achieving velocities of 10–50 m/s [7, 9].

Laser-based energy deposition has promising applications in a broad range of environments due to its non-intrusiveness and relatively precise controllability [10]. For example, laser-induced cavitation bubbles can produce varied fragmentation phenomenologies of liquid droplets [11, 12, 13]. In the biomedical field, focused laser deposition has been used for transport of living cells [14] and even proposed as a means of producing a highly focused liquid microjet in a needle-free drug injection system [15, 16]. Gas-phase breakdowns have been shown under certain conditions to reduce drag on a supersonic blunt body by modifying the upstream

shock structure with a laser-based energy deposition [17, 18], and studies suggest that certain localized but extreme load on aerodynamic vehicles may be mitigated using similarly targeted depositions [5, 19]. As a source of both heat and radical species, laser-induced can also be an effective ignition-seeding approach and attractive alternative to conventional spark-ignition systems [20].

1.2 Key motivating observations

1.2.1 Breakdown-induced flow

We focus on gas-phase breakdowns and, in particular, the late-time ($t \gtrsim 100\,\mu$s) ejection of gas, such as that shown in figure 1.1(a). This flow pattern has been observed in other similarly rapid and small energy depositions. For electrode discharges, a toroidal flow structure transports hot gas away from the breakdown region [21, 22, 23]. Kono et al. [21] attributed this to low pressure in the spark gap caused by over-expansion of the plasma kernel, which induces an inward flow and production of vorticity that then propagates outward. In laser-induced breakdowns, low pressure produced by kernel over-expansion and an associated rarefaction wave were hypothesized to lead to a similar toroidal structure [24, 25, 26, 27]. However, the specifics of how any low-pressure region leads to ejection or its reversal, especially its dependence on kernel shape (for example) remain unclear. Laser ablation of a solid surface produces a plume that ejects hot gas away from the target, which has also been attributed to over-expansion [28]. A different proposal is that the curved shock generated by the expanding plasma produces the vorticity [29], which was subsequently developed into a model for ejections from laser-induced breakdowns [30]. The relative contributions of the curved shock and over-expansion, however, have not been studied quantitatively, and the connection between the early kernel geometry, vorticity generation, and ultimate formation or reversal of the ejection remains unclear.

Even the qualitative character of the laser-induced ejection depends on local gas conditions. In multiple gases, Brieschenk et al. [9] observed ejection towards the laser source at pressure $p = 1\,$atm, while at elevated pressure the ejection pattern varied, with some reversing direction or not forming. In subsequent work, a similar reversal in ejection direction was observed for relatively mild changes in pressure (0.59 to 1 atm), as shown in figure 1.1 (J. E. Retter and G. S. Elliott, personal communication). Though precise measurements of the energy deposition are difficult to obtain, these early-time luminosity images suggest that the reversal coincides with changes in the shape of kernel and that the underlying mechanism depends on the early-time energy distribution.

Although there are some apparent similarities with jetting by bubble collapse [e.g. 31], the source of the driving pressure difference is fundamentally different. It has long been known that a collapsing bubble can

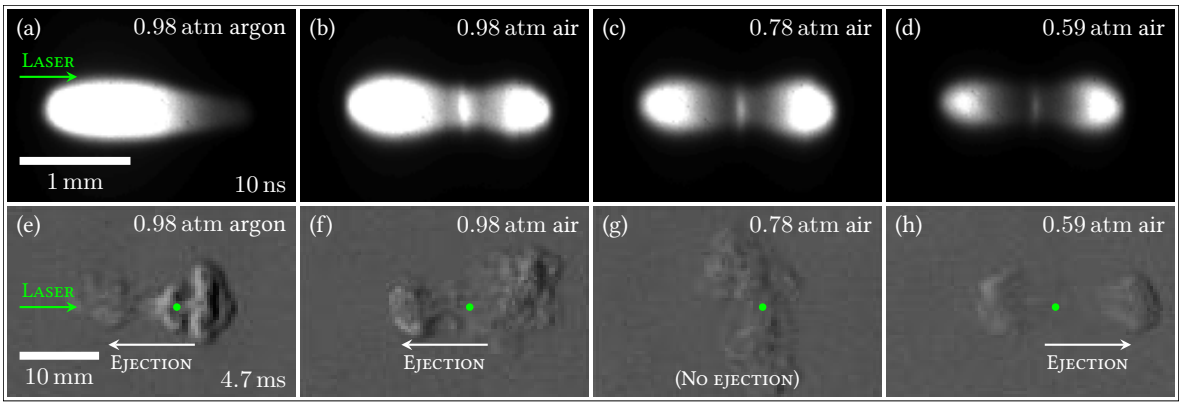

Figure 1.1: Top row: plasma luminosity in argon and air 10 ns after the laser pulse for a range of pressures. Bottom row: corresponding Schlieren images 4.7 ms after the laser pulse showing ejection reversal (J. E. Retter and G. S. Elliott, personal communication). A 50 mJ, 532 nm single-mode laser with a focal length of 75 mm and pulse FWHM of 7.7 ns was used. Emissions images were filtered with a central wavelength of 500 nm.

become unstable [32], though it is unclear whether the gas-phase laser ejection, with its rapidly expanding hot plasma kernel and only weak subsequent contraction, can be described by similar mechanisms. We focus on mechanisms of vorticity generation. In the course of analyzing the ensuing dynamics, we will draw qualitative analogies to the well-understood motion of uniform-density vortex rings (as in, for example, Picone and Boris [33] and Ranjan et al. [34]). Although density variations persist locally, by the time this description becomes useful the flow speed is subsonic with only weak compressibility effects.

1.2.2 Ignition by laser-induced breakdown

In a combustible mixture, the high temperature and significant concentrations of radical species can ignite the gas and lead to a sustained flame. Such laser-seeded ignition is attractive because it deposits energy and radicals within a flow, away from material that might degrade, and with relatively precise control over timing and location [10, 20]. Ignition in various flow configurations has been studied [35, 36, 37, 38].

Ignition by laser-induced breakdown can be affected by the post-breakdown flow characteristics. The ejection in particular, appearing as the so-called third lobe in combustible mixtures, can both enhance the rate of flame growth by increasing its surface area, yet also inhibit ignition by high strain rates [20, 39]. Supporting this, Dumitrache et al. [40] observed enhanced flame growth after suppressing the ejection with a pre-ionization pulse, which was thought to reduce flame stretching. Similarly, Torikai et al. [41] showed that the ejection can extinguish a methane flame. In contrast, figure 1.2 shows that hot gas carried by the ejection can ignite gas at a distance from the breakdown, which can be important in an inhomogeneous mixture with length scales comparable to the size of the ejection.

Studies of forced ignition of nonpremixed flows and stratified mixtures indicate that successful ignition

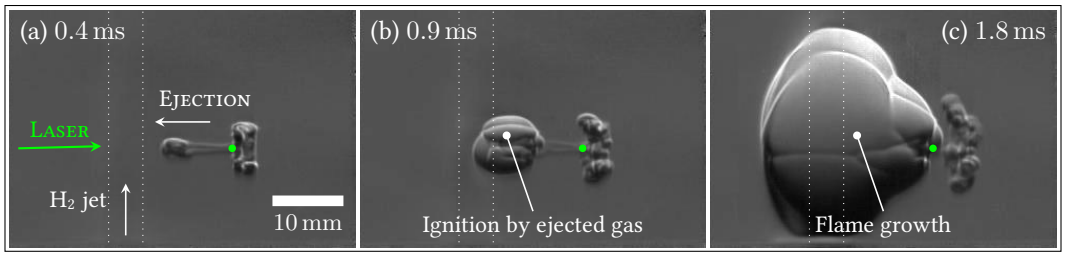

Figure 1.2: Laser-induced breakdown above an H_2, 4.8 mm-diameter jet into atmospheric-pressure air [42]. (a) The ejected hot gas (b) ignites the H_2/air mixture roughly 10 mm from the breakdown location, indicated by the green dot, leading to (c) flame growth.

depends on the energy deposited, local composition, and size of the ignition source relative to background flow gradients [43]. Propagation of the nascent flame competes with local flow strain, such as in a turbulent flow field, and is more likely to extinguish either in the presence of flame curvature, which suppresses its propagation speed, or with a smaller ignition source, for which rapid dissipation precludes transition to sustained combustion [44, 45, 46, 47, 48]. Experiments of spark ignition of a turbulent mixing layer [49] confirm the edge-flame structure predicted by simulations and the fact that successful ignition depends on the flame propagation speed. Ignition is also possible even if energy is deposited in a non-flammable region of the flow, which can convect the hot gas to the fuel [50].

While these simulation efforts have provided closer inspection of the flame dynamics, the typical ignition source deposits energy significantly slower than a laser-induced breakdown, which in contrast occurs over just $\sim$10 ns. This results in rapid expansion of the plasma kernel and a strong shock wave. We anticipate that this key difference can significantly alter the breakdown-induced flow in inhomogeneous mixtures and that these flow dynamics depend on the molecular weight of the fuel, though such an effect has yet to be explored in detail.

One approach to alter post-breakdown dynamics is to use dual laser pulses to deposit energy in close proximity, which has been studied in simulation efforts [51, 52, 53] and multiple experimental configurations. Changing the timing [54, 55] or the relative intensity [56, 57] of two pulses in air can suppress the ejection. Similarly, supplying electrons to the breakdown region with an initial femtosecond laser pulse can lead to reversal of the ejection as well as a decrease in breakdown threshold [58, 59]. In a combustible mixture, a pre-ionization ultraviolet pulse can lead to changes in the flame kernel morphology and enhance flame growth, presumably resulting from reduced flame stretching [40, 60]. Dual-pulsing can also promote mixing and lead to enhanced flame propagation [61, 62], while multi-channel electrode sparks have been shown to increase ignition probability for certain configurations [63]. Complementary to these studies, laser devices have been developed to produce simultaneous breakdowns at multiple points, in some cases with a tunable spatial distribution [64, 65, 66]. A series of many pulses with tunable frequency has also been shown to en-

hance ignition probability [67]. Furthermore, in a fuel spray, a focused laser beam can lead to many points of apparent plasma initiation in close proximity [68], and hundreds of simultaneous breakdowns can be achieved with an intense laser sheet [69]. Such advances in laser-induced breakdown techniques, their potential to improve multi-point ignition systems, and growing interest in more complex configurations warrant a greater understanding of multi-kernel dynamics.

1.3 Overview of dissertation

1.3.1 Objectives and outline

The post-breakdown flow and ignition characteristics are analyzed with direct numerical simulations. The laser-plasma physics of the breakdown are complex [8, 18, 70] and would be restrictive due to their expense, but their detailed representation is unnecessary for the current analysis of post-breakdown dynamics and substituted by an idealized energy-deposition model, which will be shown to reproduce key features in multiple configurations. The simulation methodology and breakdown model are described in chapter 2.

Given the apparent connection between the early-time kernel asymmetry and flow pattern (e.g. figure 1.1), the first objective is to analyze the principal mechanisms leading to ejection and quantify sensitivity to the kernel geometry. In chapter 3, detailed simulations with a perfect-gas model, shown to produce both ejection reversal and general agreement with experimental vorticity measurements, are used to analyze mechanisms of vorticity generation by the expanding kernel. A semi-infinite analog is introduced to isolate these mechanisms, and results are generalized to the finite-length geometry. The kernel asymmetry is found to be a central determinant of the ultimate ejection pattern, and we analyze how even subtle geometric alterations can change the relative strength and position of ring-like vortical structures produced by the breakdown and lead to ejection or its reversal.

In chapter 4, we examine how the post-breakdown flow pattern can be altered with a second pulse. Two dual-pulse configurations are analyzed, both with accompanying experiments that confirm key flow features. In the first configuration, a weak secondary pulse is shown capable of disrupting vorticity generation by the primary energy deposition, thereby suppressing the ejection or, in some cases, even leading to double ejections. A second configuration is used to analyze the effect of spatial and temporal offsets between the two pulses, which can be controlled to produce qualitative changes in the flow characteristics and an increase in the burning rate in a lean hydrogen-oxygen mixture.

While these perfect-gas analyses confirm that the post-breakdown flow pattern occurs primarily by hydro-

dynamic processes, the sensitivity to relatively small asymmetries in the kernel expansion motivates an assessment of how plasma physics can alter its development. In particular, we anticipate that potential overlap of time scales of electron recombination, thermal relaxation, or electron diffusion with those of the hydrodynamic expansion could introduce coupling mechanisms that alter the flow. In chapter 5, a two-temperature argon-plasma model is used to analyze how the nonequilibrium plasma physics might alter the hydrodynamic development. Effects are isolated by comparison with a two-species model based on the perfect-gas description, and we show that electron recombination can occur on the time scale of the hydrodynamic expansion and enhance it.

Finally, in chapter 6 we analyze how ignition can be qualitatively altered by the post-breakdown flow. The nonpremixed configuration targets the post-breakdown hydrodynamic interaction with a mixture gradient and consists of an energy deposition near a fuel–oxidizer interface. Ignition phenomenology is first demonstrated with a 9-species detailed H_2–O_2 combustion model, for ignition by the ejection, such as that observed in figure 1.2, a reduced model is used to quantify the thermal effect of radical recombination. For depositions close to the fuel interface, it shown that the hydrodynamic interaction between the fuel and expanding kernel results in a pronounced flow that suppresses ignition. The reduced model is used to generalize results to heavy fuels, for which ignition is more readily achieved due to absence of the ignition-suppressing flow response.

1.3.2 Summary of principal findings

- An instantaneous energy-deposition model of the breakdown and perfect-gas description of the subsequent flow dynamics are shown to reproduce key features of the post-breakdown flow (chapter 3).
- Vorticity is generated by baroclinic torque primarily along the kernel boundary; generation by the shock accounts for a relatively small portion (15% for some cases) of the vorticity of the ejection due to cancellation immediately behind the shock front (chapter 3).
- The ejection direction and strength are determined by a competition between vorticity generated at the ends of the kernel, which is strongly sensitive to asymmetries in the kernel geometry (chapter 3).
- Observations of ejection suppression in dual-pulse experiments [71] are consistent with the generation of opposing vorticity that results from the biased early-time expansion of the primary kernel due to the secondary pulse (chapter 4).
- The spatial and temporal offset between dual pulses can be adjusted to disperse hot gas and increase the burning rate in a lean hydrogen–oxygen mixture by a factor of 2 relative to a single pulse of equal total

energy (chapter 4), supporting the proposition that increased flame kernel surface area is a primary mechanism for the observed enhanced ignition characteristics with multiple depositions [62, 63].

- Electron recombination occurs on the time scale of the hydrodynamic expansion (in $p_\infty = 0.5\,\mathrm{atm}$ argon) and is an avenue by which ion formation energy is subsequently converted to mechanical work, thereby enhancing its expansion (chapter 5).
- Successful ignition by energy deposition in proximity to a sufficiently strong mixture gradient depends on the molecular weight of the fuel; for fuels much lighter or heavier than oxygen, the breakdown-induced flow differs qualitatively depending on where the energy is deposited and in some cases critically leads to ignition failure (chapter 6).

Chapter 2

Simulation methodology and models

2.1 Breakdown model

The model is based on early-time ($t < 100\,\mathrm{ns}$) imaging of plasma kernels. The specific geometric details of the resulting kernel can depend on the pulse energy [3], ambient pressure [6], gas composition (figure 1.1), as well as the mode of laser operation, which can lead to multiple points of apparent plasma initiation and alter the plasma boundary growth [72]. Simulations of the breakdown also show how the complex laser–plasma interaction can lead to the observed asymmetric structure [18, 73]. In all these studies, the kernel is an approximately axisymmetric and elongated region with varying front–rear asymmetry. This consistent morphology motivates the model kernel introduced in figure 2.1: a high-temperature, high-pressure gas in a region constructed from two spherical caps joined by a conical section. The overall aspect ratio α and ratio of cap radii β are

$$\alpha \equiv \frac{L}{2R_1} \qquad \text{and} \qquad \beta \equiv \frac{R_1}{R_2}.$$

Because the laser-induced breakdown occurs significantly faster ($t \sim 10\,\mathrm{ns}$) than the dynamics analyzed here, it is modeled as an instantaneous addition of internal energy,

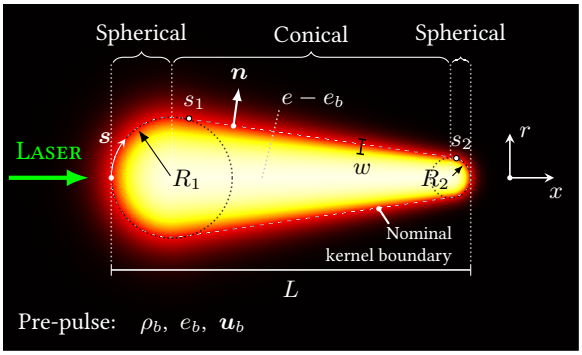

Figure 2.1: The model breakdown kernel has peak temperature peak temperature T_0 and consists of two spherical caps joined by a conical section. The contact boundary thickness $w \in [R_2, R_1]$ varies with s, and the energy $e - e_b \in [0, \Delta e_{\text{LIB}}]$ varies with n.

$$e - e_b = \Delta e_{\text{LIB}} f(n), \tag{2.1}$$

where $f(n) \equiv \frac{1}{2}\left[1 - \tanh(\sigma n)\right]$ and σ is set so $f(w/2) = 0.1$ and $f(-w/2) = 0.9$. Properties before the laser pulse are denoted by $(\ )_b$, and the initial peak temperature is T_0. Neither the pre-pulse density ρ_b nor the velocity $\boldsymbol{u}_b$ is modified by this model breakdown, which conserves both mass and momentum. The energy distribution blends smoothly with the ambient over local length scale w, which varies along the tangential coordinate s as

$$w(s) = \begin{cases} R_1, & s < s_1, \\ \dfrac{s - s_2}{s_1 - s_2} R_1 + \dfrac{s - s_1}{s_2 - s_1} R_2; & s_1 \le s \le s_2, \\ R_2, & s_2 < s, \end{cases}$$

where s_1 and s_2 are set so the spherical sections are tangent to the conical section. For single-pulse depositions in a homogeneous gas (chapters 3 and 5), the pre-pulse state is uniformly equal to its ambient value, so $\rho_b = \rho_\infty$, $e_b = e_\infty$, and $\boldsymbol{u}_b = \boldsymbol{0}$. For depositions near a fuel interface (chapter 6) and for the second pulse in dual-pulse configurations (chapter 4), the pre-pulse state is non-uniform. The total energy deposited $E \equiv \int \rho_b (e - e_b)\, \mathrm{d}V$ depends on the background density ρ_b, as denser regions of the flow absorb more energy per volume. This is consistent with observations that gas at elevated pressure, and therefore higher number density, absorbs more laser energy [6].

A passive scalar ξ is used to track the evolving kernel, especially its boundary as labeled in figure 2.1. It is

initialized with the signed distance $\xi(t=0) = n$ from the $n = 0$ boundary and subsequently advects:

$$\frac{\partial(\rho\xi)}{\partial t} + \nabla \cdot (\rho\xi \boldsymbol{u}) = 0. \tag{2.2}$$

The evolution of the nominal contact boundary is thus defined by

$$\mathrm{CB} \equiv \left\{ (x, r) \,|\, \xi(x, r, t) = 0 \right\}. \tag{2.3}$$

2.2 Gas models

Five gas models are used to analyze various aspects of the post-breakdown flow and ignition dynamics. They are summarized in table 2.1 and detailed separately in sections 3.1, 5.1.1, 5.1.2, 6.1.1, and 6.1.2.

	Temperatures	Species	Transport	Specific heats
Perfect gas	T	Single-component	Constant	Constant
Two-species	T	A, I	T-dependent	Constant in T
Nonequilibrium plasma	T_h, T_e	A, A^+, e^-	T_h, T_e-dependent	T_e-dependent
Detailed combustion	T	9 species for H_2/O_2 combustion	T-dependent	T-dependent
Reduced combustion	T	F, O, R, P	T-dependent	Constant in T

Table 2.1: Summary of gas models.

2.3 Discretization

The governing equations for all gas models are solved in axisymmetric cylindrical coordinates and advanced with an explicit fourth-order Runge-Kutta scheme. They are discretized with nine-point eighth-order centered finite difference schemes,

$$f'_j = \frac{4}{5}(f_{j+1} - f_{j-1}) - \frac{1}{5}(f_{j+2} - f_{j-2}) + \frac{4}{105}(f_{j+3} - f_{j-3}) - \frac{1}{280}(f_{j+4} - f_{j-4}) \tag{2.4}$$

$$f''_j = -\frac{205}{72} f_j + \frac{8}{5}(f_{j+1} + f_{j-1}) - \frac{1}{5}(f_{j+2} + f_{j-2}) + \frac{8}{135}(f_{j+3} + f_{j-3}) - \frac{1}{560}(f_{j+4} + f_{j-4}) \tag{2.5}$$

for first- and second-order derivatives, respectively. An eighth-order explicit filter is applied at each time step,

$$\hat{f}_j = \frac{93}{128} f_j + \frac{7}{32}(f_{j+1} + f_{j-1}) - \frac{7}{64}(f_{j+2} + f_{j-2}) + \frac{1}{32}(f_{j+3} + f_{j-3}) - \frac{1}{256}(f_{j+4} + f_{j-4}) \tag{2.6}$$

while for some cases the corresponding implicit filter

$$\begin{aligned} \hat{f}_j + \alpha_f(\hat{f}_{j+1} + \hat{f}_{j-1}) = &\frac{93 + 70\alpha_f}{128} f_j + \frac{7 + 18\alpha_f}{32}(f_{j+1} + f_{j-1}) + \frac{-7 + 14\alpha_f}{64}(f_{j+2} + f_{j-2}) \\ &+ \frac{1 - 2\alpha_f}{32}(f_{j+3} + f_{j-3}) + \frac{-1 + 2\alpha_f}{256}(f_{j+4} + f_{j-4}) \end{aligned} \tag{2.7}$$

is used with $\alpha_f = 0.495$ [74, 75] (see chapters 5 and 6). For the implicit filter, asymmetric stencils [76] are employed at the domain boundaries, excluding $r = 0$.

At the $r = 0$ coordinate singularity the governing equations are evaluated in their $r \to 0$ limit with

$$u_r = 0\,, \quad \frac{\partial \rho}{\partial r} = 0\,, \quad \frac{\partial p}{\partial r} = 0\,, \quad \frac{\partial u_x}{\partial r} = 0\,, \quad \frac{\partial^2 u_r}{\partial r^2} = 0\,, \quad \text{and} \quad \frac{\partial Y_k}{\partial r} = 0\,, \tag{2.8}$$

based on continuity and differentiability at $r = 0$ (e.g. Liu and Wang [77]), where u_x is the axial velocity, u_r is the radial velocity, ρ is the fluid density, p is the pressure, and Y_k is the species mass fraction. The $r = 0$ equations are given in appendix A. The same centered stencils of the interior are also employed at $r = 0$ and constrained to enforce (2.8) using the fact that ρ, u_x, p, and Y_k are even functions of r and that u_r is an odd function of r. Thus the same spatial accuracy is achieved at $r = 0$ as on the interior of the simulation domain. Details on the verification of the discretized equations are given in appendix B.

All analysis is performed in an essentially uniform region of a Cartesian stretched grid where the mesh spacing Δx and Δr are both within 1% of their minima $\Delta x_{\min} = \Delta r_{\min}$. The stretched coordinates are mapped independently from $z_{1,2} \in [0, 1]$ to (x, r) using

$$\begin{aligned} x =& \frac{x_{\max} - x_{\min}}{g} \left\{ \frac{a}{2b} \left[\log\Big(\cosh\big[b(z_1 - 1)\big]\Big) - \log\big(\cosh[bz_1]\big) - \log(\cosh b) \right] + (1 + a) z_1 \right\} + x_{\min} \\ r =& \frac{2 r_{\max}}{g} \left\{ \frac{a}{2b} \left[\log\Big(\cosh\Big[b \frac{z_2 - 1}{2}\Big]\Big) - \log\Big(\cosh\Big[b \frac{z_2 + 1}{2}\Big]\Big) - \log(\cosh b) \right] + (1 + a) \frac{z_2 + 1}{2} \right\} - r_{\max}, \end{aligned} \tag{2.9}$$

where

$$g \equiv 1 + a - \frac{a}{b} \log\left(\cosh b\right), \tag{2.10}$$

and a and b are used to adjust the resolution and extents of the essentially uniform region. In the stretched outer region, the difference between any two adjacent points is no greater than 3.5%. A buffer zone [78, 79], with a source term added to the flow equations $\boldsymbol{Q}_t + \mathcal{N}(\boldsymbol{Q}) = \boldsymbol{0}$, is used with support near the boundary to reduce shock reflection:

$$\boldsymbol{Q}_t + \mathcal{N}(\boldsymbol{Q}) = \max(\sigma_x, \sigma_r)(\boldsymbol{Q}_\infty - \boldsymbol{Q}). \tag{2.11}$$

The strength of the source term is determined by

$$\sigma_x = \begin{cases} \sigma\left(\frac{x_1 - x}{x_1 - x_{\min}} - 1\right)^2, & x < x_1 \\ \sigma\left(\frac{x - x_2}{x_{\max} - x_2} - 1\right)^2, & x > x_2 \\ 0, & \text{otherwise} \end{cases} \qquad \sigma_r = \begin{cases} \sigma\left(\frac{r - r_1}{r_{\max} - r_1} - 1\right)^2, & r > r_1 \\ 0, & \text{otherwise} \end{cases}$$

where $\boldsymbol{Q}_\infty$ is the ambient value of the flow variables, $x \in [x_1, x_2]$ and $r \in [0, r_1]$ define the essentially uniform region, and σ is typically taken to be $\sigma = L/a_\infty$. Characteristics boundary conditions [80] are used with the pressure-based stabilization procedure of Poinsot and Lele [81]. The mesh extents, mesh resolution, and other discretization details vary depending on the gas model being simulated; more details are given in their respective sections.

Chapter 3

Ejection and its reversal in a perfect gas

3.1 Perfect-gas model

The post-breakdown flow is modeled by the compressible Navier–Stokes equations for an ideal gas,

$$\frac{\partial \rho}{\partial t} + \nabla \cdot (\rho \boldsymbol{u}) = 0 \tag{3.1}$$

$$\frac{\partial \rho \boldsymbol{u}}{\partial t} + \nabla \cdot (\rho \boldsymbol{u}\boldsymbol{u}) = -\nabla p + \nabla \cdot \boldsymbol{\tau} \tag{3.2}$$

$$\frac{\partial \rho (e + |\boldsymbol{u}|^2/2)}{\partial t} + \nabla \cdot [\rho (e + |\boldsymbol{u}|^2/2)\boldsymbol{u}] = -\nabla \cdot (p\boldsymbol{u}) + \nabla \cdot (\boldsymbol{\tau}\boldsymbol{u}) + \nabla \cdot \boldsymbol{q} \tag{3.3}$$

$$p = \rho \frac{\overline{R}}{W} T \tag{3.4}$$

where ρ, $\boldsymbol{u}$, e, p, T, W, and $\overline{R}$ are the density, velocity, internal energy, pressure, temperature, molecular weight, and gas constant, respectively. The stress tensor $\boldsymbol{\tau}$ and heat flux $\boldsymbol{q}$ are

$$\boldsymbol{\tau} = \mu \left(\nabla \boldsymbol{u} + \nabla \boldsymbol{u}^T \right) + \left(\mu_B - \frac{2}{3} \right) (\nabla \cdot \boldsymbol{u}) \boldsymbol{I}, \tag{3.5}$$

$$\boldsymbol{q} = \lambda \nabla T \tag{3.6}$$

where the viscosity μ and thermal conductivity λ are taken to be uniformly equal to their ambient values $\mu = \mu_\infty$ and $\lambda = \lambda_\infty$, and the bulk viscosity is taken to be $\mu_B = 0.6\mu$ as a model for air [82]. Constant μ and λ is clearly an approximation, especially in the hot plasma core. This reduced model is used to represent the range of possible phenomenologies and elucidate underlying hydrodynamic mechanisms rather than provide full quantitative detail at these extreme conditions. The model will be shown to reproduce key experimental observations in section 3.3.1, and viscous effects are assessed in more detail in section 3.4.5. Temperature-dependent transport properties are included in the combustion and nonequilibrium-plasma models (sections 5.1.1 and 6.1.1).

The equations are nondimensionalized by the kernel length L and ambient density ρ_∞ and speed of sound $a_\infty = \sqrt{\gamma p_\infty/\rho_\infty}$:

$$\hat{t} = \frac{t a_\infty}{L}\,, \qquad \hat{\boldsymbol{x}} = \frac{\boldsymbol{x}}{L}\,, \qquad \hat{\rho} = \frac{\rho}{\rho_\infty}\,, \qquad \hat{\boldsymbol{u}} = \frac{\boldsymbol{u}}{a_\infty}\,, \qquad \hat{p} = \frac{p}{\gamma p_\infty}\,, \qquad \hat{T} = \frac{T}{(\gamma-1)T_\infty}\,, \qquad \hat{e} = \frac{e}{a_\infty^2}\,, \tag{3.7}$$

where γ is the specific heat ratio. The nondimensional equations are

$$\frac{\partial \hat{\rho}}{\partial \hat{t}} + \hat{\nabla}\cdot(\hat{\rho}\hat{\boldsymbol{u}}) = 0 \tag{3.8}$$

$$\frac{\partial \hat{\rho}\hat{\boldsymbol{u}}}{\partial \hat{t}} + \hat{\nabla}\cdot(\hat{\rho}\hat{\boldsymbol{u}}\hat{\boldsymbol{u}}) = -\hat{\nabla}\hat{p} + \hat{\nabla}\cdot\hat{\boldsymbol{\tau}} \tag{3.9}$$

$$\frac{\partial \hat{\rho}(\hat{e}+|\hat{\boldsymbol{u}}|^2/2)}{\partial \hat{t}} + \hat{\nabla}\cdot[\hat{\rho}(\hat{e}+|\hat{\boldsymbol{u}}|^2/2)\hat{\boldsymbol{u}}] = -\hat{\nabla}\cdot(\hat{p}\hat{\boldsymbol{u}}) + \hat{\nabla}\cdot(\hat{\boldsymbol{\tau}}\hat{\boldsymbol{u}}) + \hat{\nabla}\cdot\hat{\boldsymbol{q}} \tag{3.10}$$

$$\hat{p} = \frac{\gamma-1}{\gamma}\hat{\rho}\hat{T} \tag{3.11}$$

where $\hat{\nabla}$ is the derivative operator nondimensionalized by L and

$$\hat{\boldsymbol{\tau}} = \frac{1}{\mathrm{Re}}\left[\left(\hat{\nabla}\hat{\boldsymbol{u}} + \hat{\nabla}\hat{\boldsymbol{u}}^T\right) + \left(\hat{\mu}_B - \frac{2}{3}\right)(\hat{\nabla}\cdot\hat{\boldsymbol{u}})\boldsymbol{I}\right], \qquad \hat{\boldsymbol{q}} = \frac{1}{\mathrm{Re}\,\mathrm{Pr}}\hat{\nabla}T\,.$$

The Reynolds and Prandtl numbers are

$$\mathrm{Re} = \frac{\rho_\infty a_\infty L}{\mu_\infty}, \qquad \mathrm{Pr} = \frac{c_p \mu_\infty}{\lambda_\infty},$$

and $\hat{\mu}_B = \mu_B/\mu_\infty = 0.6$. The equations are solved with specific heat ratio $\gamma = 1.4$. Unless otherwise noted, in all perfect-gas simulations the Reynolds number $\mathrm{Re} = 4.4 \times 10^4$ and Prandtl number $\mathrm{Pr} = 0.72$ correspond to an $L = 2\,\mathrm{mm}$ kernel in $p_\infty = 1\,\mathrm{atm}$ air at $T_\infty = 298\,\mathrm{K}$. For cases in which the perfect-gas model is exercised, the shocks generated are relatively weak and modeled in the Navier–Stokes limit, with confirmed mesh independence; no shock-capturing is used in conjunction with this model.

3.2 Discretization details for perfect-gas simulations

Each flow solution is computed from three simulations on successively coarser meshes with larger extents. The finest mesh is necessary when the shock is strongest, and results are interpolated onto the next mesh using bicubic polynomial splines when the shock reaches the simulation boundary. Shocks are modeled in their Navier–Stokes limit, with confirmed mesh independence; for example, doubling the mesh density resulted in less than 1% change in the net circulation and maximum flow velocity for $T_{\mathrm{LIB}} = 26.9T_\infty$. No shock-capturing is used for perfect-gas simulations. For the most intense cases in section 3.4.4, greater resolution ($1.25 \times 10^{-4}L$) was required for this degree of mesh independence; for those conditions it was further verified that the post-shock pressure and velocity agree with the one-dimensional equivalent Riemann problem to within 0.4% (appendix B.3). To further assess accuracy, particularly for analysis of shock-generated vorticity (section 3.4.2), a still finer spacing is used ($2.5 \times 10^{-5}L$), which confirmed insensitivity to the mesh.

The meshes are summarized in table 3.1. Simulations are advanced with an explicit fourth-order Runge–Kutta scheme using a time step

$$\Delta t = \min_{(x,r)} \frac{\mathrm{CFL}}{\frac{|u_x|+a}{\Delta x} + \frac{|u_r|+a}{\Delta r}}\,, \tag{3.12}$$

where a is the local speed of sound. In the majority of perfect-gas simulations, the Reynolds number is sufficiently high that the inviscid criterion (3.12) is sufficient, and $\mathrm{CFL} = 0.8$ is used. For low Reynolds numbers cases (section 3.4.5), a lower CFL is used to maintain stability.

	Type	Mesh spacing	Extents	Uniform region	Size	Simulated time
1	Uniform	$5 \times 10^{-4}L$	$3.06L \times 1.25L$	$3.06L \times 1.25L$	6120×2500	$ta_\infty/L \lesssim 0.5$
2	Uniform	$1 \times 10^{-3}L$	$6.12L \times 2.5L$	$6.12L \times 2.5L$	6120×2500	$0.5 \lesssim ta_\infty/L \lesssim 2.0$
3	Stretched	$3 \times 10^{-3}L$	$40L \times 20L$	$20L \times 10L$	7380×3690	$ta_\infty/L \gtrsim 2.0$

Table 3.1: Meshes used to compute each perfect-gas flow solution. The simulated time depends on the when the shock reaches the boundaries of meshes 1 and 2 and varies across cases.

3.3 Ejection phenomenology

3.3.1 Comparison with experiment

We first confirm that the model reproduces key experimental observations. For this, the model parameters α, β, and L are based on early-time imaging—figure 3.1 shows the fitting process—and T_0 is chosen such that the energy deposited matches measurement. Given the assumptions (idealized geometry, uniform and instantaneous energy deposition, ideal gas properties), we have no expectation of precise agreement. Still, figure 3.2 shows that the vorticity agrees qualitatively with measurement: the predominantly $\omega_\theta < 0$ vorticity is ejected leftward, whereas the predominantly $\omega_\theta > 0$ vorticity is located farther from the axis and, in this case, moves slowly rightward. There is quantitative agreement in net circulation until at least 200 μs, consistent with the similar auto-advection speeds of the ejection. By 500 μs the on-average axisymmetry is apparently disrupted by shot-to-shot variation. Onset of three-dimensional instabilities will affect this late-time development, though the degree of comparison here suggests that it does not alter the mechanisms of vorticity production leading to the organized motion, which will be shown to occur well before the times of figure 3.2. The relative temperature distribution in figure 3.3 shows similar agreement with different measurements [7]: the ambient gas breaches the kernel at approximately 50 μs, and the hottest gas is pushed outward from the symmetry axis.

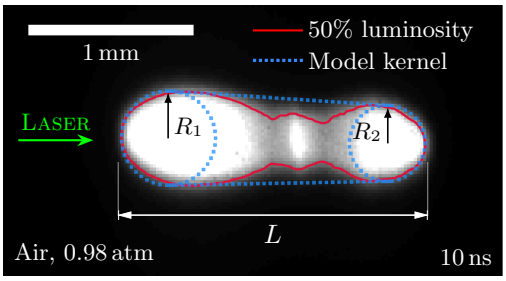

Figure 3.1: The model kernel is fit to the 50% normalized luminosity level of the early-time kernel image, reproduced here from figure 1.1(b). R_1 and R_2 are chosen as the maximum radial extents of the left and right halves, respectively, with their centers chosen such that the model kernel matches in length.

3.3.2 Kernel evolution and ejection

A case with $\alpha = 3$ and $\beta = 3$ is described here in detail. The geometric parameters are based on general observations of luminous regions in experiments, and a full range is considered subsequently. Figure 3.4 shows the kernel volume, based on the nominal contact boundary (2.3), and its mean interior pressure and temperature, defined as

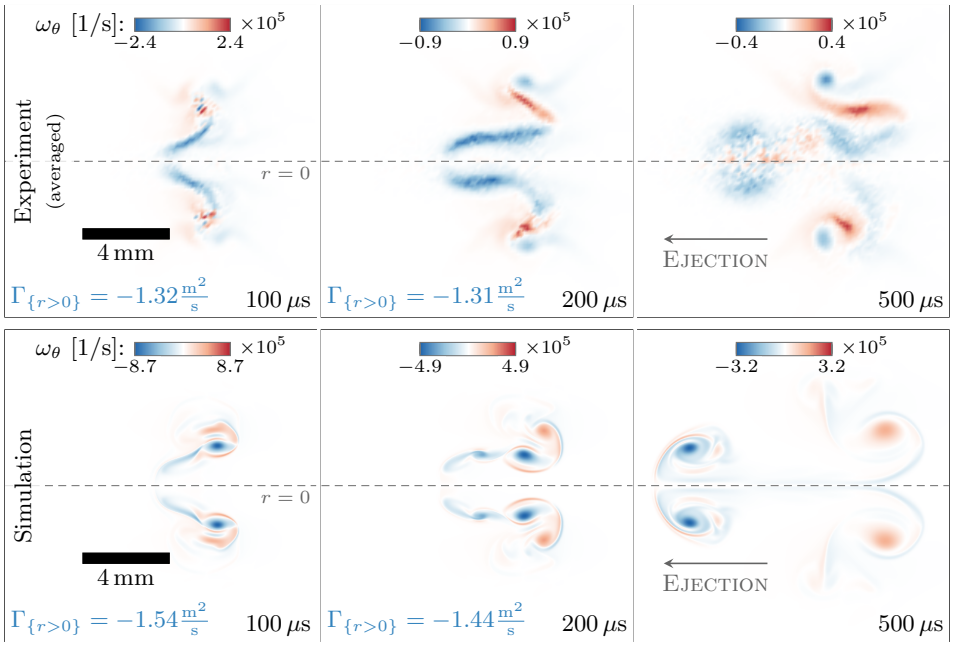

Figure 3.2: Top row: PIV-measured azimuthal vorticity averaged over 100 breakdowns in 1 atm air [83], with the same laser configuration as in figure 1.1. Bottom row: simulation with the present model using $\alpha = 3.23$, $\beta = 1.24$, and $L = 1.84$ mm based on figure 3.1. Though simulation of an individual breakdown leads to sharper features than the averaged experimental data (note the different color levels), the net circulation $\Gamma \equiv \int\int \omega_\theta \, \mathrm{d}x \, \mathrm{d}r$ in the $r > 0$ half-plane matches to within 10% at 200 μs, with $\Gamma_{\{r>0\}}$ and $\Gamma_{\{r<0\}}$ differing by less than 1% in the experiment.

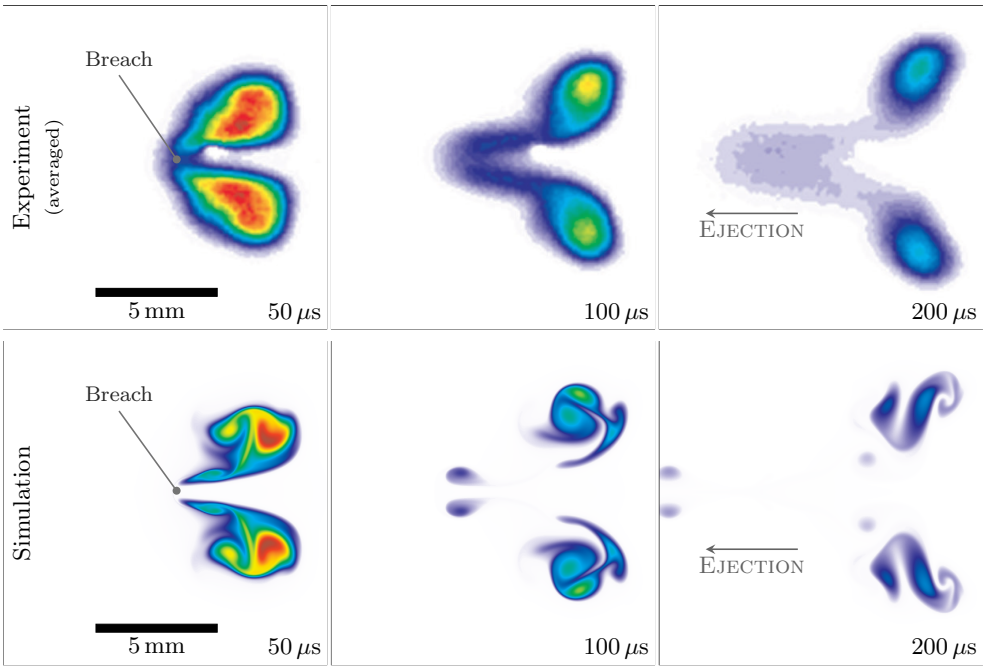

Figure 3.3: Top row: temperature averaged over 200 breakdowns in 0.97 atm air [7], adapted here with permission. Bottom row: simulation with the present model using $\alpha = 3.24$, $\beta = 1.92$, and $L = 2.71$ mm based on plasma kernel imaging at 25 ns in their corresponding experiments. A direct comparison of temperature values is not informative for the perfect gas model of the present simulations.

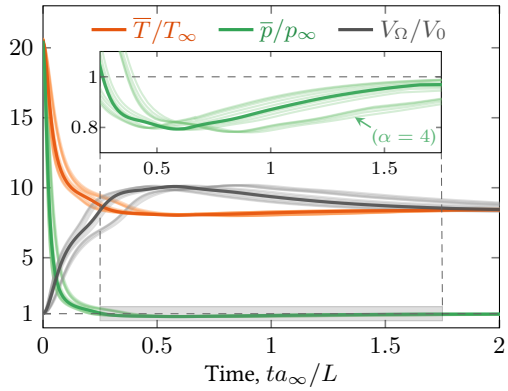

Figure 3.4: Relative mean pressure and temperature (3.13) and kernel volume, with V_0 the initial volume. Fainter lines show only mild variation due to geometry ($\alpha \in [2, 4]$, $\beta \in [1.2, 3.0]$) relative to the $\alpha = 3$, $\beta = 3$ baseline case; $\alpha = 4$ kernels attain $\min \overline{p}$ and $\max V$ later in time.

$$\overline{p} \equiv \frac{\gamma - 1}{\gamma} c_p \overline{\rho}\,\overline{T} \qquad \text{and} \qquad \overline{T} \equiv \frac{\gamma}{c_p}\overline{e}, \tag{3.13}$$

where

$$\overline{\rho} \equiv \frac{1}{V}\int_{\mathcal{V}} \rho \,\mathrm{d}V \qquad \text{and} \qquad \overline{e} \equiv \frac{1}{\overline{\rho}V}\int_{\mathcal{V}} \rho e \,\mathrm{d}V',$$

$\mathcal{V}$ the region enclosed by the contact boundary (2.3) and V is its volume. Both $\overline{T}$ and $\overline{p}$ decrease rapidly as the kernel expands, producing the shock wave visualized in figure 3.5(a). The part of this shock emanating from the conical section of the model geometry, approximately normal to the axis, is strongest, which is consistent with experimental observations [84]. The kernel reaches its maximum volume at $t \approx 0.5L/a_\infty$, at which point the interior pressure has dropped below p_∞ and subsequently begins to equilibrate.

These early dynamics induce the complex flow shown in figure 3.5(b), which marks the beginning of the ejection. A region of negative-x momentum near $r = 0$ on the right side of the kernel is associated with negative vorticity, which can be interpreted as auto-advecting leftward. Most of this momentum is in the dense inward-flowing ambient gas outside the kernel boundary. It breaches the hot, low-density ($\rho \approx \rho_\infty/8$) kernel at $t \approx 9.0L/a_\infty$, as shown in figure 3.5(c).

Figure 3.6 shows the circulation,

$$\Gamma \equiv \int\int \omega \,\mathrm{d}r \,\mathrm{d}x, \tag{3.14}$$

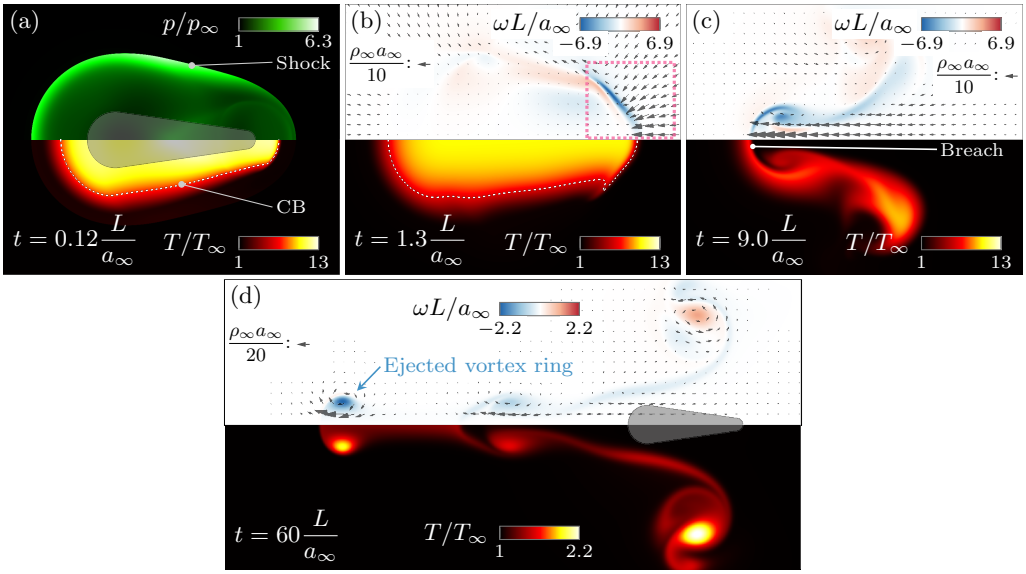

Figure 3.5: Formation of a leftward ejection with $\alpha = 3$ and $\beta = 3$. (a) The shock, visualized with the pressure, propagates outwards from the contact boundary (CB); the initial kernel is shown in grey. (b–d) The vorticity distribution, $\rho\boldsymbol{u}$ vectors, and ejection as labeled. The dotted box in (b) highlights the region of negative x-momentum leading to the ejection. Momentum instead of velocity vectors are shown due to the density variation.

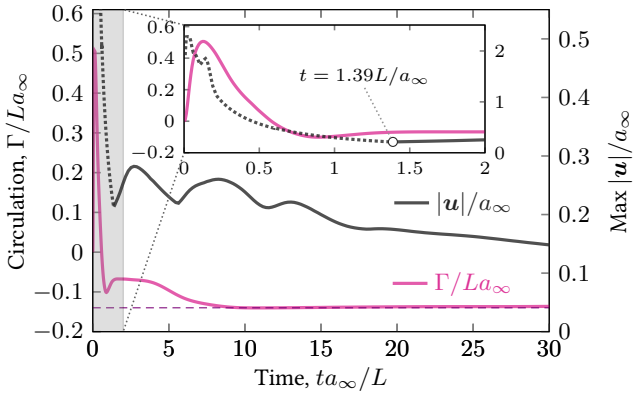

Figure 3.6: Circulation and maximum speed. The dashed line at $\Gamma = -0.14La_\infty$ is shown for reference. Before $t = 1.39L/a_\infty$, $\max|\boldsymbol{u}|$ is associated with the shock and marked by a dotted line.

where

$$\omega \equiv \omega_\theta = \frac{\partial u_r}{\partial x} - \frac{\partial u_x}{\partial r}.$$

Rapid production of circulation occurs before $t = 2L/a_\infty$, which coincides with the changes in pressure seen in figure 3.4. Beyond this time the flow is subsonic and qualitatively consistent with auto-advection of existing vorticity, albeit in a variable-density fluid. This is not expected to be significant in interpreting the evolution since 79% of the volume within L of the kernel center has $\rho > 0.8\rho_\infty$. After the kernel is

breached at $t \approx 9L/a_\infty$ (figure 3.5c), the circulation remains approximately constant, and the negative vorticity separates from the nominal breakdown location and propagates as a hot vortex ring (figure 3.5d). By $t = 60L/a_\infty$ its speed is within 20% of the standard auto-advection speed U of an incompressible and constant-density vortex ring,

$$U = \frac{\Gamma_0}{4\pi r_0}\left[\ln\left(\frac{8r_0}{a}\right) - \frac{1}{4}\right]. \tag{3.15}$$

For making this estimate, its nominal position (x_0, r_0) is marked by the peak vorticity ω_0, the circulation Γ_0 is the total within $x \in [x_0 - 2r_0, x_0 + 2r_0]$ (as in Archer et al. 85), and the radius $a = \sqrt{\Gamma_0/\pi\omega_0}$ is such that a uniform vortex core with $\omega = \omega_0$ would have the same circulation. The specific sources of vorticity will be analyzed in detail in sections 3.4 and 3.5.

3.3.3 Dependence on kernel geometry

The hydrodynamic development depends on the initial kernel geometry, which we vary over $\alpha \in [2, 12]$ and $\beta \in [1/3, 3]$ to include a range of observations [6, 42]. Figure 3.7 shows that the net circulation Γ changes sign with both α and β, with corresponding reversals in the ejection, quantified by its length L_E. Fore-aft symmetry effects ($\beta \lessgtr 1$), which appear to correspond to early-time luminosity imaging (figures 1.1b–d), can obviously lead to reversal, with more asymmetric kernels (larger β or $1/\beta$) producing greater circulation and a more pronounced ejection. Closer inspection also suggests that the ejected vortex ring of such kernels has a smaller radius and propagates faster (e.g. $\beta = 1.5$ versus $\beta = 3$), consistent with (3.15). For near-symmetric kernels ($1/1.2 \lesssim \beta \lesssim 1.2$) a distinct ejection is not observed, and the vorticity instead collects into a ring pair that travels outward from the symmetry axis. More curiously, increasing the aspect ratio beyond $\alpha \approx 5$ also leads to reversal, though the rightward ejection is somewhat weaker than its leftward counterpart. Details of the ejection failure at $\beta \approx 1.2$ and the reversal at $\alpha \approx 5$ will be discussed in section 3.6.

3.4 Mechanisms of vorticity generation: a semi-infinite analog

3.4.1 Configuration

An analogous, semi-infinite geometry (figure 3.8) is introduced here to isolate vorticity-generating mechanisms from subsequent vortex formation and interaction dynamics, which are considered in more detail subsequently. The thermal initial condition (2.1) is used for a cylindrical section that extends effectively

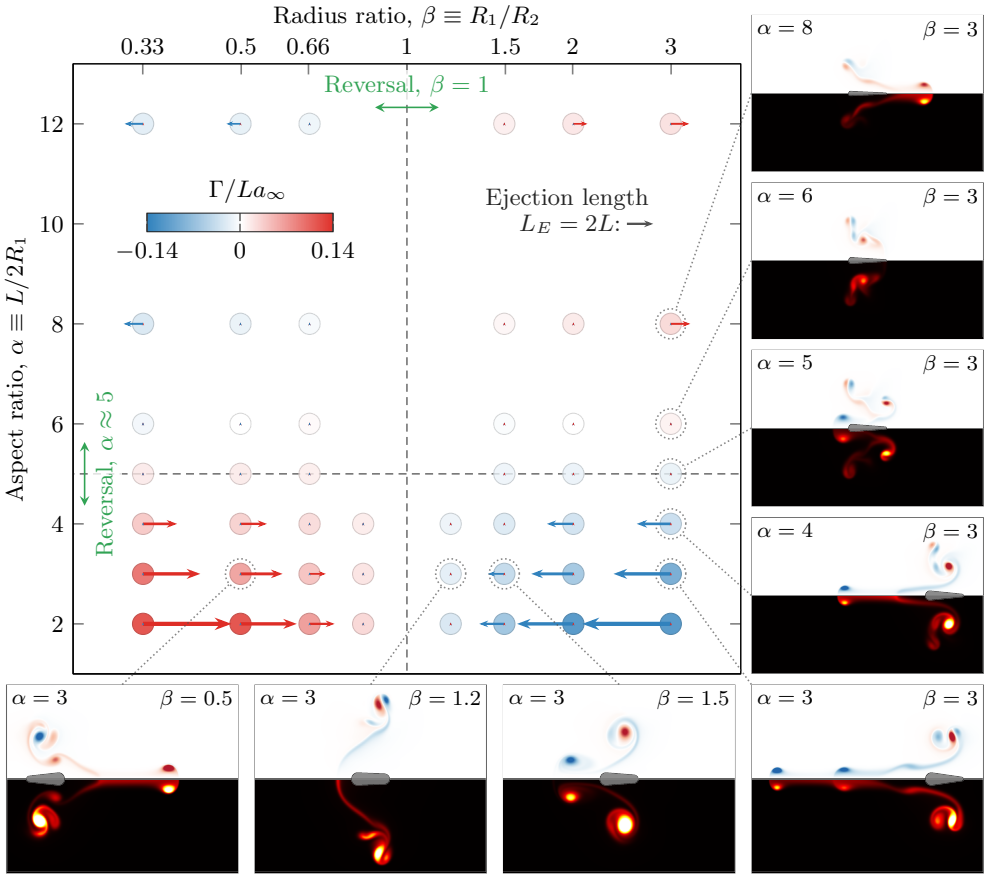

Figure 3.7: Dependence of the ejection character on α and β, visualized with the vorticity and temperature at $t = 100L/a_\infty$, with the initial kernel in grey. Each data point is colored by the net circulation Γ (3.14), and arrows correspond to the ejection length L_E, taken to be the axial distance from the center of the initial kernel to the point of peak vorticity $\max|\omega|$. Only $L_E > L$ arrows are shown to indicate cases in which a clear ejection is observed.

to $x \to -\infty$ and capped by a hemisphere at $x = 0$. Practically, this configuration was implemented in a sufficiently long domain to preclude interactions between the ends for the times considered. Without a length scale analogous to L, we use $\mathrm{Re}_{R_2} \equiv \rho_\infty a_\infty R_2/\mu = 2400$ to be consistent with the baseline $\alpha = 3$, $\beta = 3$ geometry for which $L = 18R_2$. This configuration has four nondimensional parameters (Re_{R_2}, T_0/T_∞, γ, Pr), which is simplifying since it avoids the α and β parameters of section 3.3.3. Dependence on Re_{R_2} is quantified in section 3.4.5.

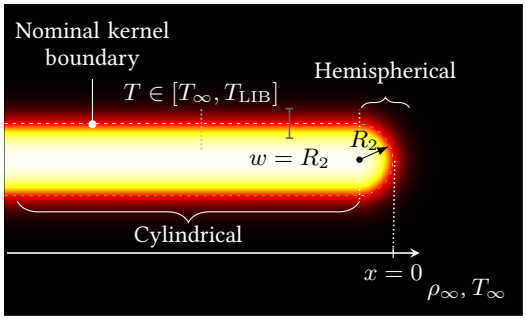

Figure 3.8: The semi-infinite geometry consists of an infinitely long cylindrical section and a hemispherical cap.

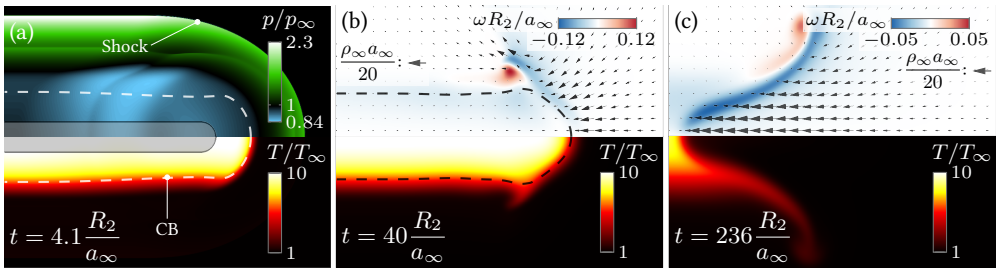

Figure 3.9: (a) The shock decouples from the kernel, initially in the grey region, and (b) leaves behind a region of negative vorticity that (c) penetrates into the hot, low-density kernel. Vectors correspond to $\rho\boldsymbol{u}$.

The flow generated by this configuration is shown in figure 3.9. As for the finite-L cases, the expanding kernel produces a shock, behind which there is transient sub-ambient pressure near the kernel (figure 3.9a). By $t = 40R_2/a_\infty$ (figure 3.9b), obvious negative vorticity has been produced near the end, and by $t = 236R_2/a_\infty$ the associated negative-x flow at the end of the kernel has penetrated into the low-density kernel (figure 3.9c). The evolution after this point is phenomenologically consistent with auto-advection of the vorticity, with a maximum velocity less than $0.1a_\infty$. The faster vorticity advection near the axis resembles that of the finite-length cases (figure 3.5c).

3.4.2 Vorticity generation by the shock

By $t = 1.19R_2/a_\infty$, the kernel has cooled from $26.9T_\infty$ initally to a peak of $13.0T_\infty$, and the shock has decoupled from the hot gas, as shown in figure 3.10(a), leaving a triangle-like region of negative vorticity behind it. Positive vorticity is also produced along the contact boundary during this early expansion, though this is largely canceled by a subsequent mechanism, which will be discussed in section 3.4.3.

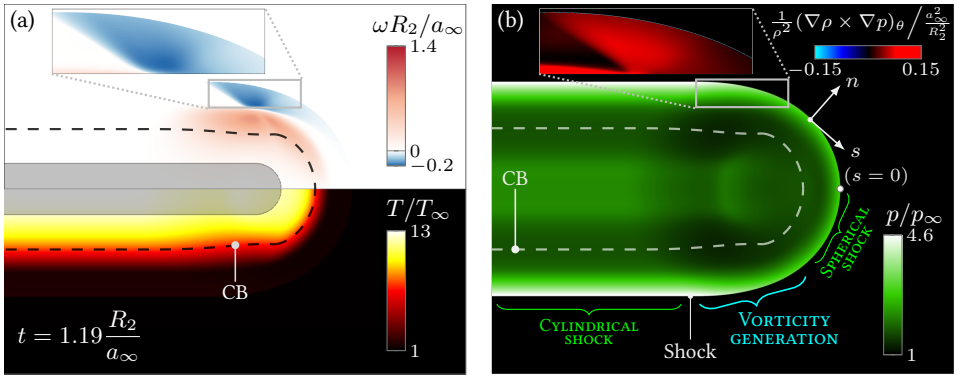

Figure 3.10: (a) Negative vorticity generation by the shock at $t = 1.19R_2/a_\infty$ is (b) partially canceled by positive baroclinic torque. The initial kernel is shaded gray in (a).

The dominant source of the negative vorticity is tangential variation in the shock strength, quantified by the pressure immediately behind the shock (figure 3.11). Away from the cylindrical–spherical junction, it matches the pressure at these short times for corresponding spherical and cylindrical cases. It is the faster

decay of the spherical shock that leads to the pressure gradient between the two regions.

Theoretical estimates for shock-generated vorticity were independently derived by Truesdell [86] and Lighthill [87] and generalized by Hayes [88]. For an unsteady, axisymmetric shock of varying strength,

$$\omega = \frac{\rho_s}{\rho_\infty}\left(1 - \frac{\rho_\infty}{\rho_s}\right)^2 \frac{\partial U}{\partial s},$$

where ρ_s is the density behind the shock, U is the shock speed, and s is the local tangent coordinate. Applying shock-jump relations yields

$$\omega = \frac{\gamma+1}{4\gamma}\frac{\rho_s}{\rho_\infty}\left(1 - \frac{\rho_\infty}{\rho_s}\right)^2 \frac{1}{\sqrt{\frac{\gamma-1}{2\gamma} + \frac{\gamma+1}{2\gamma}\frac{p_s}{p_\infty}}}\frac{a_\infty}{p_\infty}\frac{\mathrm{d}p_s}{\mathrm{d}s}, \tag{3.16}$$

where p_s is the pressure behind the shock. Thus, the region of negative vorticity in figure 3.10 is produced by the tangential pressure gradient in figure 3.11(a) and grows in size as this region grows along the shock front.

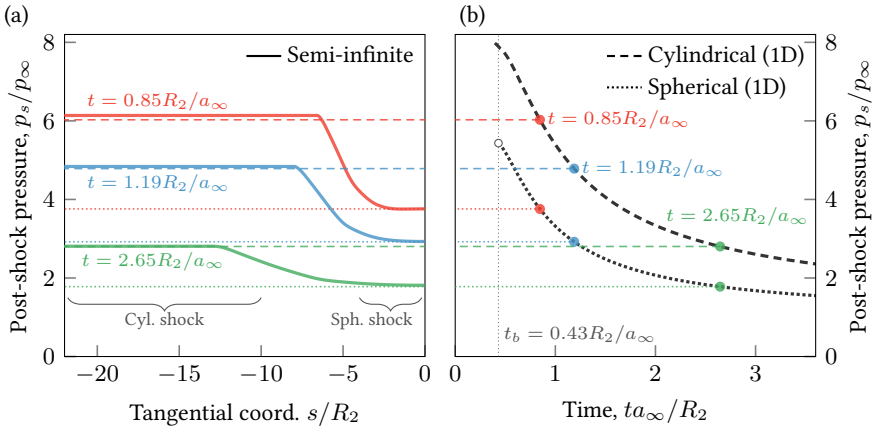

Figure 3.11: Pressure behind the shock for the (a) axisymmetric semi-infinite kernel and (b) corresponding spherically and cylindrically symmetric cases.

In figure 3.10(b), it is also evident that a distributed baroclinic torque behind the shock acts to cancel the shock-generated vorticity. The misalignment of $\nabla\rho$ and ∇p that drives this is illustrated schematically in figure 3.12(a). In the effectively spherical and cylindrical regions, pressure and density closely match the corresponding one-dimensional case and therefore have parallel gradients. Between these regions, the higher pressure behind the cylindrical shock (figure 3.12b) leads to misalignment.

The net effect of these two vorticity sources—negative at the shock and positive behind the shock—is

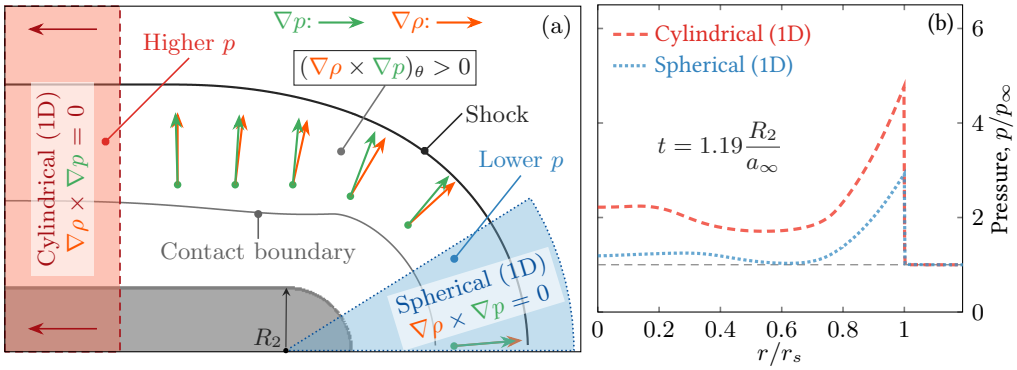

Figure 3.12: (a) Schematic showing the post-shock misalignment of $\nabla\rho$ and ∇p between the effectively one-dimensional regions, and (b) corresponding pressure profiles, where r_s is the position of the shock.

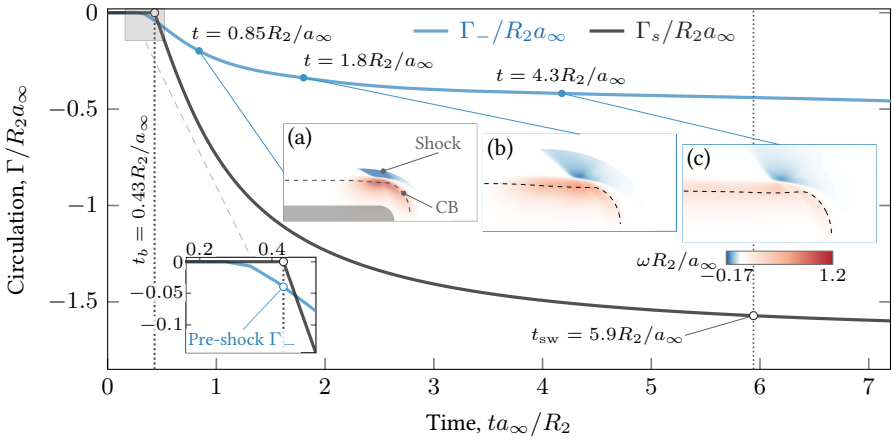

Figure 3.13: Total negative circulation Γ_- (3.17) and shock-generated circulation Γ_s (3.18).

quantified by the negative circulation Γ_-,

$$\Gamma_-(t) \equiv \int\int_{\omega<0} \omega(t)\,\mathrm{d}x\,\mathrm{d}r, \tag{3.17}$$

shown in figure 3.13, which decreases monotonically as the shock propagates. Their respective contributions can be estimated by integrating (3.16) for the shock-generated circulation,

$$\Gamma_s(t) \equiv \int\int \omega(t)\,\mathrm{d}n\,\mathrm{d}s,$$

using the shock speed for $\mathrm{d}n = U\,\mathrm{d}t$, which upon applying the shock-jump relation as in (3.16) yields

$$\Gamma_s(t) = \frac{\gamma+1}{4\gamma} \int_{\tau=t_b}^{t} \int_{-\infty}^{0} \frac{\rho_s}{\rho_\infty} \left(1 - \frac{\rho_\infty}{\rho_s}\right)^2 \frac{a_\infty^2}{p_\infty} \frac{\mathrm{d}p_s}{\mathrm{d}s}\, \mathrm{d}s\, \mathrm{d}\tau.$$

Because $p_s = p_s(s)$, the s-integration can be recast as

$$\Gamma_s(t) = \frac{\gamma+1}{4\gamma} \int_{t_b}^{t} \int_{p_{\mathrm{cyl}}(\tau)}^{p_{\mathrm{sph}}(\tau)} \frac{\rho_s}{\rho_\infty} \left(1 - \frac{\rho_\infty}{\rho_s}\right)^2 \frac{a_\infty^2}{p_\infty}\, \mathrm{d}p_s\, \mathrm{d}\tau, \tag{3.18}$$

where p_{cyl} and p_{sph} are the corresponding cylindrical and spherical shock pressures. The shock formation time t_b is the time at which the compression wave steepens into a shock, as marked by ρ reaching its maximum value, which always occurs on the shock in these simulations. t_b is calculated from the spherical configuration; the cylindrical shock forms only about 10% earlier (figure 3.11b). Conclusions do not depend on this choice since the pre-shock generation of vorticity is small, as seen in the figure 3.13 inset.

By time $t = t_{\mathrm{sw}}$, with $\dot{\Gamma}_s t_{\mathrm{sw}} < 0.1\Gamma_s$ signifying the nominal end of significant shock-driven vorticity generation, the shock is too weak to produce even 10% additional circulation. By this time it is approximately $10R_2$ from the kernel, so it is also unclear that any small addition would couple with the ejection dynamics. The negative circulation remaining after the post-shock cancellation, which removes 72% of Γ_s by t_{sw} (figure 3.13), will be shown to constitute a relatively small portion of the peak negative circulation, attained as the ambient gas begins to penetrate into the kernel (section 3.4.3).

Vorticity generation by the differential blast strength has been connected to vorticity production in other configurations as well [23, 29]; for the present case, analysis indicates that a large portion is cancelled by the post-shock rarefaction. We also note that while this idealized spherical–cylindrical geometry facilitates analysis, shock-generation of vorticity does not depend on it specifically, only on the increasing shock strength away from the end of the kernel. This key behavior is supported by experiments, in which measured shock speeds are faster in r than in x [84], consistent with the observation that the shock evolves from elongated to spherical [3, 71].

3.4.3 Baroclinic generation at the kernel boundary

The second mechanism we consider operates over a longer time than the shock, until $t \approx 87R_2/a_\infty = 15t_{\mathrm{sw}}$. A low-pressure region around the hot kernel remnant leads to ∇p that is approximately perpendicular to the strong $\nabla\rho$ associated with the kernel boundary (figure 3.14). Pressure traces show the important x-

component of this gradient and the trailing rarefaction behind the shock. The corresponding evolution of Γ_- in figure 3.15 indicates that this baroclinic torque produces more vorticity than the net left behind the shock. Approximately 28% of the peak negative circulation $\Gamma^-_{\max}$, attained at $t = 87R_2/a_\infty$, is produced by the shock before $t_{\rm sw}$. However, unlike the shock, which deposits vorticity in the dense ambient gas, this mechanism produces vorticity in hot gas with $\rho \lesssim \rho_\infty/5$, so its long-term contribution to the flow is anticipated to be somewhat suppressed. The vorticity from the shock, though deposited at early times, persists and appears unaffected by the baroclinic generation near the contact boundary.

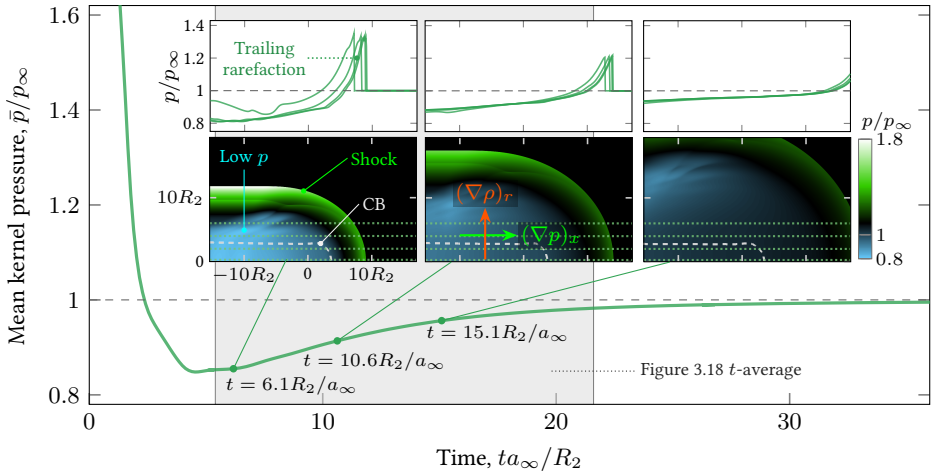

Figure 3.14: Evolution of the mean kernel pressure (3.13) and pressure field, with slices at $r/R_2 = 0$, 2, 4, and 6 showing the x-component of its gradient. $\bar{p}$ is computed by integration over $x \geq -9R_2$ only, which corresponds to right half of the $\alpha = 3$, $\beta = 3$ kernel in which $L = 18R_2$.

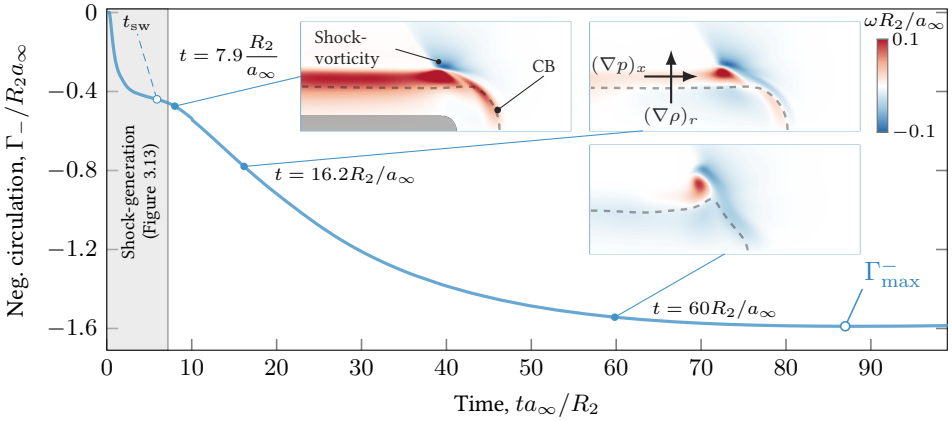

Figure 3.15: Vorticity production near the contact boundary. The short time window of figure 3.13 covering the period of significant generation by the shock is indicated for reference. The peak negative circulation $\Gamma^-_{\max}$ is attained at $t = 87R_2/a_\infty$.

The low-pressure region in figure 3.14 is due to the expansion following the shock. Figure 3.16(a) depicts Cartesian, cylindrical, and spherical analogues, which all produce a shock with a trailing rarefaction shown in figure 3.16(b). In the cylindrical and spherical geometries, this region, including the kernel itself (figure 3.16c),

has $p < p_\infty$ before equilibrating, which corresponds to the low pressure in figure 3.14.

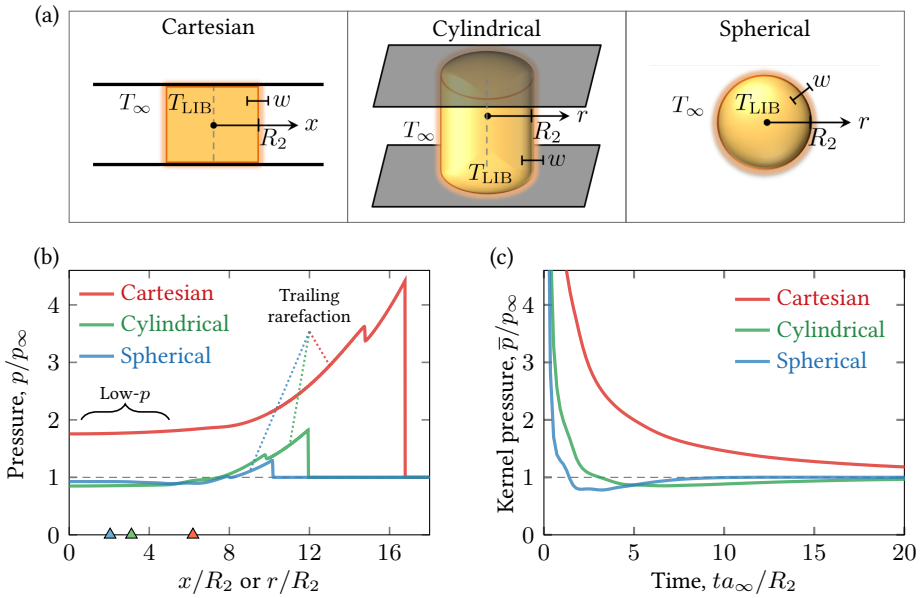

Figure 3.16: (a) Analogous one-dimensional configurations produce (b) a trailing rarefaction behind the shock and low-pressure region around the kernel, whose (c) mean pressure can become sub-ambient. Profiles in (b) are shown at $t = 6.3R_2/a_\infty$, with triangle symbols marking the location of the contact boundary.

The mechanism by which expansion waves lead to this low pressure is illustrated for the simpler one-dimensional case in Figure 3.17. Figure 3.17(a) shows the pressure and characteristic velocities at $x = 0$. For clarity a sharpened-boundary case $w = R_2/100$ is also shown to better highlight the distinct expansions that progressively decrease the pressure. Each expansion phase corresponds to a rarefaction reaching $x = 0$ (figure 3.17b), with the first originating at the kernel boundary and subsequent rarefactions produced by reflection. Between expansions, the state of the gas at $x = 0$ is constant. Figure 3.17(a) also shows that a kernel with a diffuse boundary, matching our simulations with $w = R_2$, tracks this behavior though with the overlapping rarefactions smoothing the profiles. Viscous effects are sufficiently weak that increasing Re_{R_2} by a factor of 2 results in less than 1% change in p and $u \pm a$ in figure 3.17(a).

The same mechanism produces low pressure near the origin in the radial configurations. However, a rarefaction wave propagating towards $r = 0$ must expand outward-travelling gas into a larger volume than a corresponding wave in a Cartesian geometry [89], resulting in $p < p_\infty$ as noted in figure 3.16(b).

Though direct correspondence to the one-dimensional cases diminishes rapidly in time, a nearly one-dimensional character holds during the expansion in approximately cylindrical and spherical regions, where there is only weak misalignment of $\nabla\rho$ and ∇p (figure 3.18). It is interacting rarefactions between these regions that ultimately lead to baroclinic generation in the full model, with nearly perpendicular $\nabla\rho$ and ∇p.

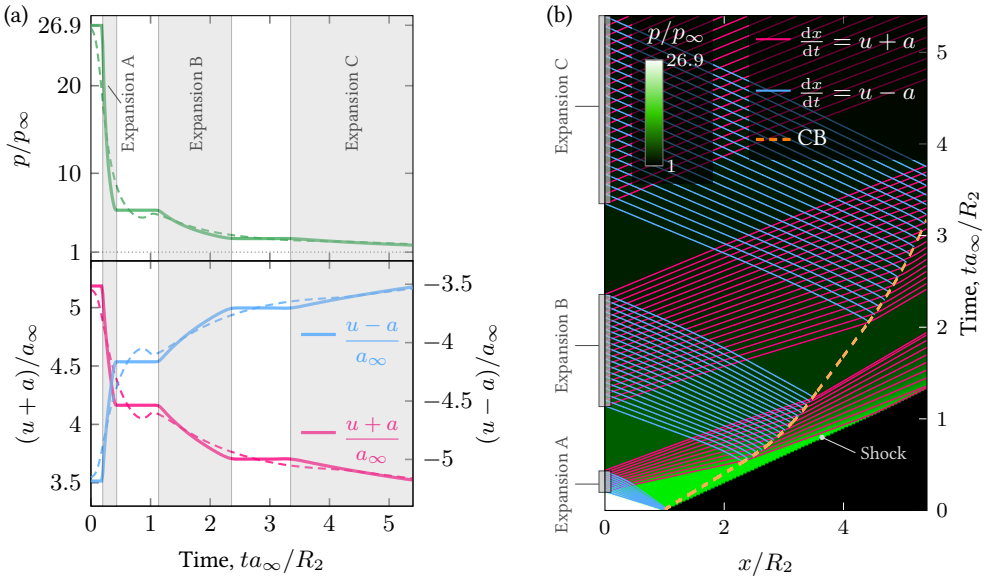

Figure 3.17: (a) Evolution of pressure and characteristic velocities at $x = 0$ for the Cartesian configuration, showing a series of expansions that cause the pressure to decrease, both for a sharp boundary (——) $w = R_2/100$ and for the simulated CB scale (- - -) $w = R_2$. (b) Pressure evolution in x–t ($w = R_2/100$) and subset of characteristics.

We note that though over-expansion is intrinsic to the radial expansion and has been studied in spherical blasts [89, 90, 91, 92] and associated with post-breakdown ejections [25, 26], the resulting $\overline{p} < p_\infty$ is not necessary for vorticity generation. The mechanism requires only that rarefactions behind the shock, which decrease the kernel pressure by reflection at $r = 0$, produce a misaligned pressure gradient across the kernel boundary.

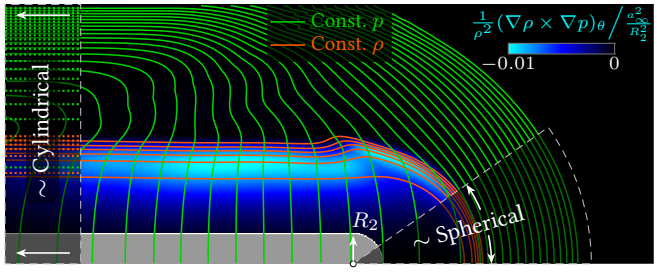

Figure 3.18: Pressure, density, and baroclinic torque averaged over $ta_\infty/R_2 \in [5.4, 21.6]$ (indicated in figure 3.14), with $p/p_\infty \in [0.91, 0.98]$ and $\rho/\rho_\infty \in [0.15, 0.70]$ contour levels. The time interval is chosen to emphasize the trailing rarefaction over early-time shock-generation ($t_{sw} = 5.9R_2/a_\infty$); the relative distribution of torque is insensitive to averaging beyond $21.6R_2/a_\infty$. Dotted (·····) contour levels show the corresponding 1D cylindrical configuration for reference.

3.4.4 Dependence on T_0/T_∞

Shock-generation is confirmed to be the increasingly weaker mechanism for increasing T_0/T_∞ in figure 3.19. The shock-generated negative circulation $\Gamma^-_{sw} \equiv \Gamma_-(t_{sw})$ is consistently smaller than the peak Γ^-_{max}, with the shock's relative contribution decreasing with higher T_0. Baroclinic generation in the trailing rarefaction

is thus anticipated to be the dominant mechanism for most cases of interest.

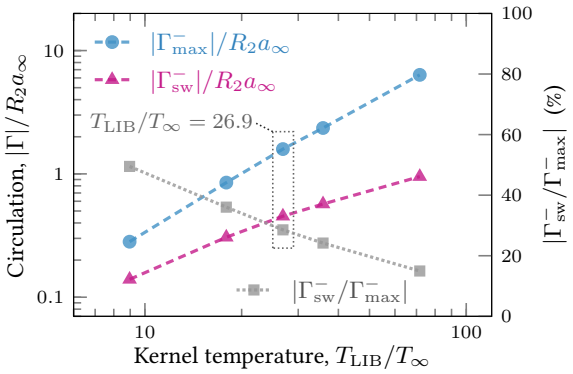

Figure 3.19: Dependence of the peak negative circulation $\Gamma^-_{\max}$ and shock-generated $\Gamma^-_{\rm sw} \equiv \Gamma_-(t_{\rm sw})$ on T_0/T_∞. For the most intense case, meshes with four times finer spacing than those in table 3.1 were required to establish mesh independence.

3.4.5 Dependence on R_2

With R_2 the only length scale, it is straightforward to assess viscous effects in this configuration. Focusing on the circulation,

$$\frac{\Gamma}{R_2 a_\infty} = f\left(\frac{t a_\infty}{R_2}, \mathrm{Re}_{R_2}, \frac{T_0}{T_\infty}, \gamma, \mathrm{Pr}\right),$$

figure 3.20 shows that Γ/R_2a_∞ and Γ_-/R_2a_∞ are Re_{R_2}-independent for $\mathrm{Re}_{R_2} \gtrsim 2000$, implying

$$\Gamma = R_2 a_\infty f\left(\frac{T_0}{T_\infty}\right) \tag{3.19}$$

at a fixed ta_∞/R_2 and constant γ and Pr. Thus for $\mathrm{Re}_{R_2} \gtrsim 2000$, larger R_2 leads to proportionally greater circulation, which will inform the finite-L kernel discussion for high aspect ratios α in section 3.5.

3.5 Vorticity generation for finite L

Shock-generation of vorticity occurs at each end of the finite-L kernel by the same mechanism as in the semi-infinite configuration (section 3.4.2). However, because it derives from a relatively short-lived pressure gradient along the shock front (e.g. $t_{\rm sw} = 0.33L/a_\infty$ for R_2 with $\alpha = 3$, $\beta = 3$), which quickly separates from the kernel, we do not anticipate, nor have we observed, that it is qualitatively changed by disturbances

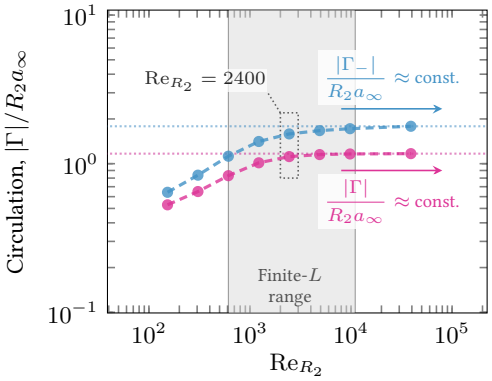

Figure 3.20: Dependence of $|\Gamma|$ and $|\Gamma_-|$ on Re_{R_2} in the semi-infinite configuration at $t = 100R_2/a_\infty$, by which time Γ is only slowly varying. All analysis in sections 3.4.2 and 3.4.3 is conducted at $\mathrm{Re}_{R_2} = 2400$; the slight slope in $|\Gamma_-|$ for $\mathrm{Re}_{R_2} > 2400$ corresponds to only 10% change over one decade. The range of Re_{R_1} and Re_{R_2} corresponding to the finite-L cases in section 3.5 is shown here for reference.

from the other end. As will be shown, the kernel asymmetry primarily affects baroclinic generation along the contact boundary, which appears to leave shock-vorticity outside the boundary unaffected (as seen in figure 3.15). Furthermore, based on the semi-infinite cases shown in figure 3.19, shock generation is expected to be the weaker mechanism for finite-L kernels as well.

We therefore focus on generation by the trailing rarefaction, which is significantly affected by kernel asymmetry. Figures 3.21(a) and (c) show that increasing β leads to increased negative torque at the smaller R_2 end, which is consistent with the greater negative circulation $\Gamma^-_{\{x>0\}}$ on the R_2 side at $t = 1.5L/a_\infty$ shown in figures 3.21(b) and (d). Relative to the kernel center, the centerpoint of the shock (and consequently its rarefaction) is biased towards the larger R_1 side, where more energy is deposited, leaving it misaligned with the kernel center, as suggested by Bradley et al. [27]. This x-offset between the apparent shock center and kernel is greater for the more asymmetric $\beta = 3$ kernel and augments $\nabla p \times \nabla \rho$ near the smaller end. For the $\alpha = 3$, $\beta = 3$ case, as an example, this leads to $\Gamma < 0$ (see figure 3.6).

Figure 3.22 shows this effect more broadly: at each α, a larger energy centroid offset $|x_E|$, corresponding to a more asymmetric kernel, consistently produces a larger shock–kernel offset (figure 3.22a), which is associated with greater negative circulation on the R_2 side (figure 3.22b). The nondimensionalization $\Gamma^-_{\{x>0\}}/R_2a_\infty$ removes the increase in $\Gamma^-_{\{x>0\}}$ due solely to larger R_2, as shown in the semi-infinite configuration (figure 3.20). With the $\alpha = 12$ cases having $\mathrm{Re}_{R_2} \in [600, 1200]$, this smaller-end intensification appears to persist even for the low-Re_{R_2} cases.

This offset effect increases $\Gamma^-_{\{x>0\}}$ for all $\beta > 1$ but is countered by a competing effect for $\alpha \geq 5$ that leads to the transition in the relative circulation produced at either end, seen in figure 3.23. This is also reflected in the circulation time traces (figure 3.24), which also indicates that Γ is approximately constant for all cases by

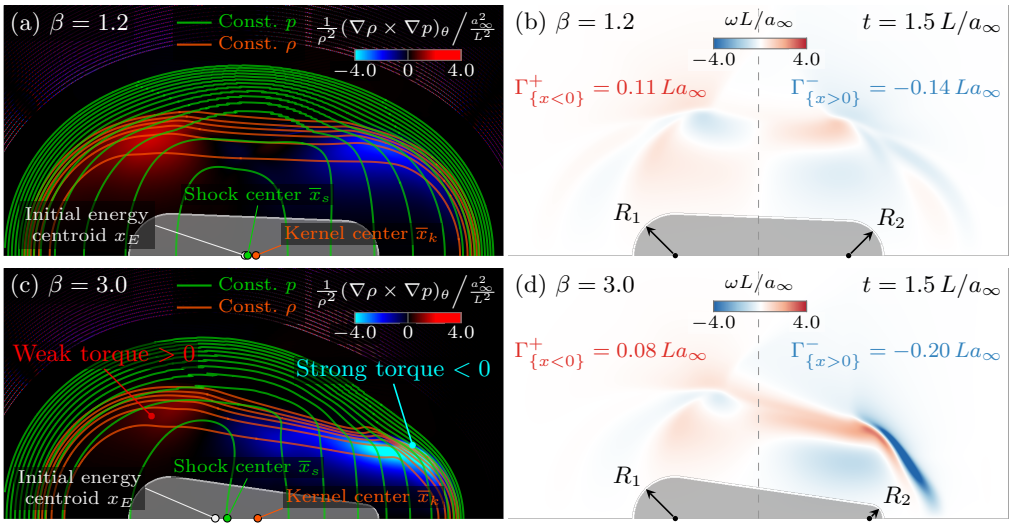

Figure 3.21: Pressure, density, and baroclinic torque averaged over $ta_\infty/L \in [0.3, 1.5]$, with $p/p_\infty \in [0.84, 0.94]$ and $\rho/\rho_\infty \in [0.15, 0.70]$ contour levels, and instantaneous vorticity field for (a,b) $\beta = 1.2$ and (c,d) $\beta = 3.0$, both with $\alpha = 3$. The time interval is chosen to emphasize the trailing rarefaction over early-time shock-generation; the relative distribution of torque is insensitive to averaging beyond $1.5L/a_\infty$. The shock and kernel centers (t-averages $\overline{x}_s$ and $\overline{x}_k$ shown) are the midpoints of their respective x-extents at $r = 0$; their offset varies by $0.05L$ over the time interval. The initial energy centroid is $\int x\rho_\infty(e - e_\infty)\,\mathrm{d}V / \int \rho_\infty(e - e_\infty)\,\mathrm{d}V$. Positive and negative circulation in $x < 0$ and $x > 0$, respectively, as marked in (b) and (d).

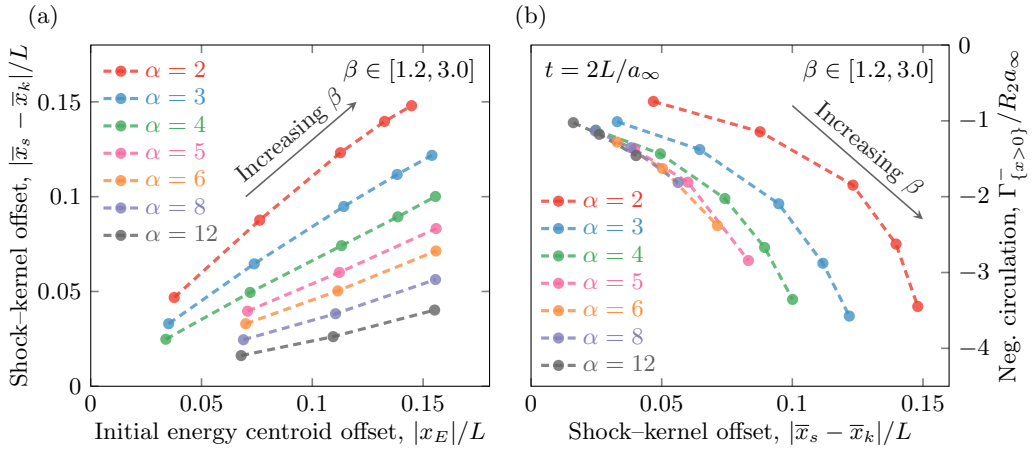

Figure 3.22: (a) Larger $x_E \equiv \int x\rho_\infty(e - e_\infty)\,\mathrm{d}V / \int \rho_\infty(e - e_\infty)\,\mathrm{d}V$ leads to a greater shock–kernel offset and (b) stronger $\Gamma^-_{\{x>0\}}$ at $t = 2L/a_\infty$, by which time Γ is approximately constant for all cases. The shock and kernel centers ($\overline{x}_s$ and $\overline{x}_k$ respectively) are averaged over $t \in [0.3, 2]L/a_\infty$ to emphasize generation by the trailing rarefaction over early-time shock-generation.

$t = 2L/a_\infty$. For larger α, the shock–kernel offset is relatively small, and the associated increase in negative circulation weak (figure 3.22b). Though finite-L effects hamper direct comparison, the dynamics of each end of an elongated kernel more closely resemble those of the semi-infinite configuration, in which smaller R_2 produce less circulation (figure 3.20). Thus the sign change of Γ results from the positive vorticity of the larger R_1 end simply overwhelming the negative vorticity of the R_2 end. For sufficiently large α the effect is compounded by viscosity further decreasing the circulation at the R_2 end.

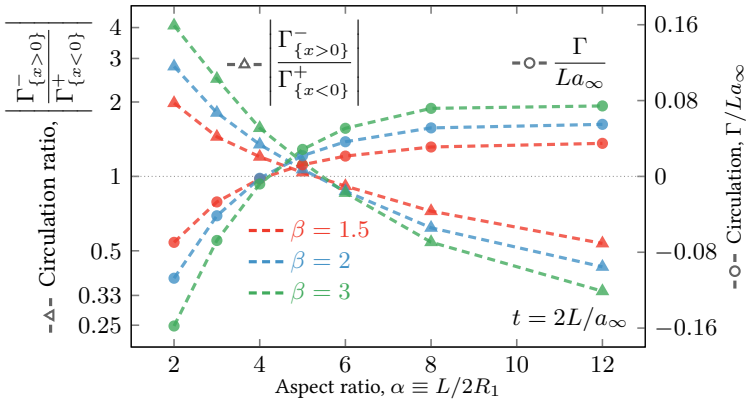

Figure 3.23: Dependence of net circulation and circulation ratio on α at $t = 2L/a_\infty$.

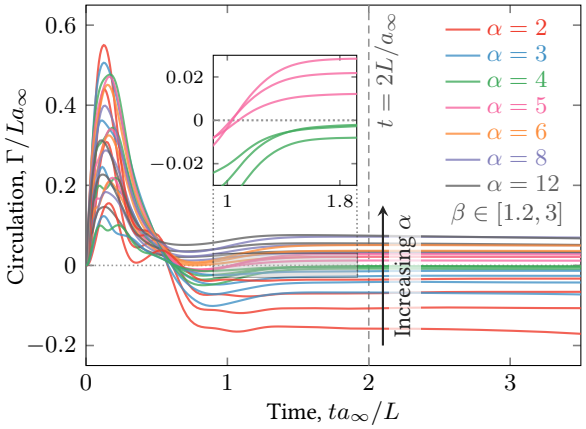

Figure 3.24: Time trace of net circulation for finite-L geometries $\alpha \in [2, 12]$, $\beta \in [1.2, 3]$.

A secondary effect also contributes to this transition. During the early-time expansion (figure 3.25a), a tangential pressure gradient develops along the conical region of the CB because gas at smaller r depressurizes faster than that at larger r. Dimensional considerations of the corresponding one-dimensional configuration suggest $p/p_\infty = g(ta_\infty/R_0)$, which is confirmed in figure 3.25(b) for $\alpha = 8$. The resulting ∇p and $\nabla \rho$ misalignment produces positive vorticity in all finite-L cases, becoming relatively more important for larger α, with its longer kernel and smaller ends. As will be shown in section 3.6, the $\alpha \approx 5$ transition to $\Gamma > 0$ (figure 3.23) is important for subsequent ejection characteristics.

3.6 Ejection and its reversal

As seen in section 3.3.2, for ejection to occur a vortex-ring-like structure must separate from the rest of the evolving hydrodynamics. We anticipate means by which this could occur in section 3.6.1. With this context, the mechanisms leading to the ejection characteristics seen in figure 3.7 are then described in sections 3.6.2 and 3.6.3.

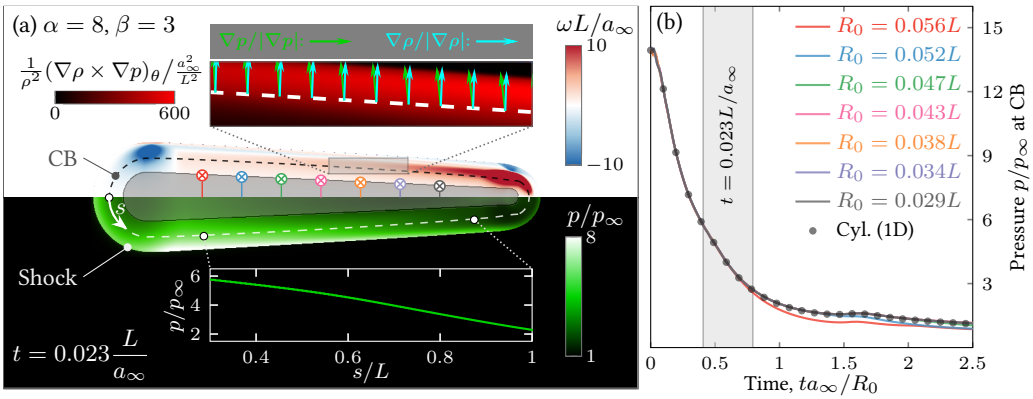

Figure 3.25: (a) Vorticity and pressure at $t = 0.023L/a_\infty$ for $\alpha = 8$, $\beta = 3$ showing positive baroclinic generation along the conical section of the contact boundary (CB) due to the tangential pressure variation $p(s)$. (b) Pressure traces at the CB, extracted at $x/L = \{-0.3, -0.2, \ldots, 0.3\}$, match the corresponding cylindrically symmetric case for the early times shown. The initial CB location $r = R_0$ at each x is marked by $\otimes$ in (a).

3.6.1 Candidate end-end vorticity interactions

It is clear from analysis of the semi-infinite configuration (section 3.4) that vorticity generated at either end of the kernel auto-advects towards its center. Several candidate scenarios for their subsequent interaction, shown schematically in figure 3.26, describe how an ejection can form or not. In figure 3.26(a), ejection occurs due to a vortex-ring-like structure simply being stronger at one end of the kernel than the other. Another route to ejection could result from a size mismatch. If the ring-like structure on one end is significantly smaller, as shown in figure 3.26(b), it could then auto-advect through the center of the larger structure, propagating at a higher velocity because of its smaller radius. In both of these cases, the opposing ring-like structure is pushed outward and slows as the ejecting structure is compressed inward and accelerates, leading to its prominent ejection. The experimental visualization in figure 1.2(a) seems to be such an example. While these first two scenarios presume that coherent vortical structures have formed prior to interaction, the third scenario in figure 3.26(c) concerns their time to form, which can depend on both the strength and radial location of distributed vorticity. The vorticity at one end may collect into a structure too slowly to collectively interact with the vorticity from the other end, which then ejects. Though the remaining vorticity may form into a ring subsequently, we anticipate that it would be significantly disrupted by and occur after the passing of the ejection and be pushed to larger r. Finally, in figure 3.26(d), we anticipate the primary means by which we expect ejection to fail: if the vorticity forms into similar structures at the ends of the kernel concurrently, vortex ring dynamics suggest that the structures will collide and progress outwards as a vortex pair that decelerates. Vorticity diffusion is neglected in this discussion: with $\rho = \rho_\infty/10$ and $\mu = \mu_\infty$, a characteristic time τ to diffuse over $l = L/2$,

$$\tau = \frac{1}{\pi^2}\frac{l^2}{\mu/\rho} = \frac{\mathrm{Re}}{40\pi^2}\frac{L}{a_\infty},$$

is much slower ($\tau \approx 110L/a_\infty$ for most cases) than the typical times observed ($\sim 10L/a_\infty$) to form an ejecting vortex ring (for example in figure 3.5c–d).

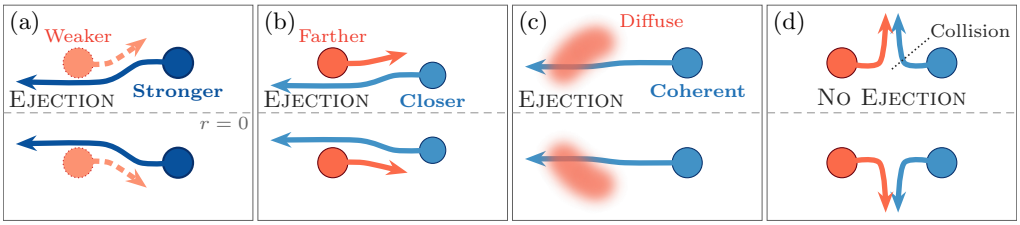

Figure 3.26: Four basic modes of vorticity interaction can lead either to ejection—by mismatched (a) strength, (b) radial location, or (c) formation time—or (d) to its failure. We note that though (d) could be considered as radially "ejecting" and resembles flow produced by electrode sparks [e.g. 21, 23], it is does not correspond to the axial ejection being analyzed.

Clearly these are idealizations of a complicated flow, and there is no expectation of a precise decomposition into such a clean a set of processes. However, as we analyze the evolution of the simulated flows in the following sections, we will see all these for different configurations. Moreover, these hydrodynamic scenarios are not limited by the specific breakdown model considered here, as a more complicated geometry or non-uniform kernel temperature, for example, will also lead to such asymmetries in the vorticity interaction.

3.6.2 Ejection failure with decreasing β

As the kernel changes from near symmetry ($1/1.2 \lesssim \beta \lesssim 1.2$) to greater asymmetry ($\beta \gtrsim 1.5$ or $\beta \lesssim 1/1.5$), we see in figure 3.27 the anticipated transition from the collision mechanism (figure 3.26d) to an ejection mechanism (figures 3.26b). We focus specifically on the vorticity at the ends of the kernel as marked. While the peak value does not necessarily occur there, we anticipate that the interaction of this end-vorticity, with its dense gas and inward-pointing momentum, will primarily determine the character of the ejection.

In figures 3.27(d) and (e), the positive and negative vorticity produced at the ends of the $\beta = 1.2$ kernel have almost mirrored trajectories as they collect into coherent vortex structures. Due to their similar strength and radii, they collide at the $x = 0$ symmetry plane, after which the most prominent structure radiates outward (figure 3.27f). Without the axisymmetric constraint, azimuthal instabilities would presumably cause this to break into the more irregular features seen in experiments (figure 1.1g), though agreement with experiment (e.g. figures 3.2a and b) is still achieved during the earlier phase of more organized flow. With modestly larger asymmetry ($\beta = 1.5$), the negative vorticity from the smaller end of the kernel collects sufficiently

close to $r = 0$ that it passes through the opposing positive vorticity, which subsequently collects into a larger ring (figures 3.27a–c).

The other two ejection mechanisms (figures 3.26a and c) also play a role. Early, at $t = 1.9L/a_\infty$, the vorticity is similarly distributed for both the $\beta = 1.2$ and $\beta = 1.5$ kernels, but the latter has more concentrated negative vorticity near the smaller end, which results from the shock–kernel offset as discussed in section 3.5. By $t = 13L/a_\infty$ (figure 3.27b), though not yet formed into a distinct ring, its relative coherency suggest the figure 3.26(c) scenario. Its greater strength also facilitates passage through the opposing structure, similar to figure 3.26(a), and later constitutes the ejection.

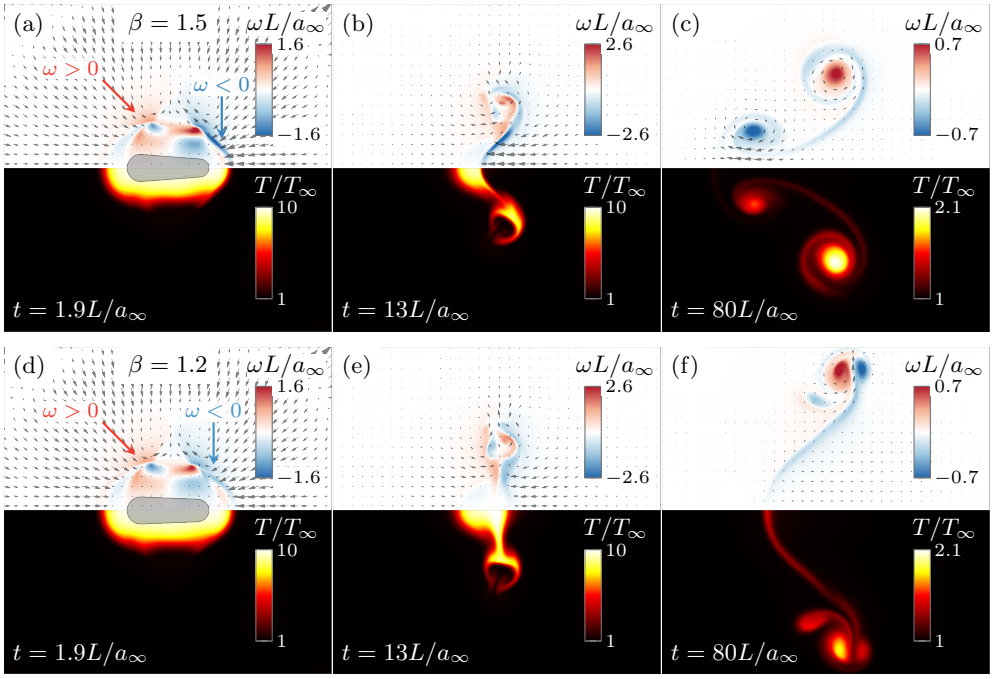

Figure 3.27: A $\beta = 1.5$, $R_2 = 0.11L$ kernel (a–c) forms a left-propagating vortex ring, whereas a $\beta = 1.2$, $R_2 = 0.14L$ kernel (d–f) does not. The initial kernels are shown in grey, both with $\alpha = 3$, and vectors correspond to $\rho\boldsymbol{u}$.

To further understand this transition between collision and ejection, we revisit the semi-infinite configuration and take t_p to be the time the vorticity penetrates the kernel:

$$\xi(x = -R_2, r = 0, t = t_p) = 0,$$

where ξ is the advected scalar (2.2) and $x = 0$ is labeled in figure 3.8. This marks the time at which the contact boundary (2.3) intersects the initial centerpoint of the hemispherical cap, occuring between figures 3.9(b) and (c) for example. Following the same arguments leading to (3.19), we anticipate the penetration time and the negative vorticity position,

$$r_- \equiv \frac{\int\int_{\omega<0} \omega r \,\mathrm{d}x \,\mathrm{d}r}{\int\int_{\omega<0} \omega \,\mathrm{d}x \,\mathrm{d}r}, \tag{3.20}$$

to be proportional to R_2 as well—$t_p \propto R_2$ and $r_- \propto R_2$—which is remarkably accurate (figure 3.28). The smaller end of the finite-L kernel, therefore, produces vorticity closer to $r = 0$ and thus penetrates earlier and passes through that of the opposite end.

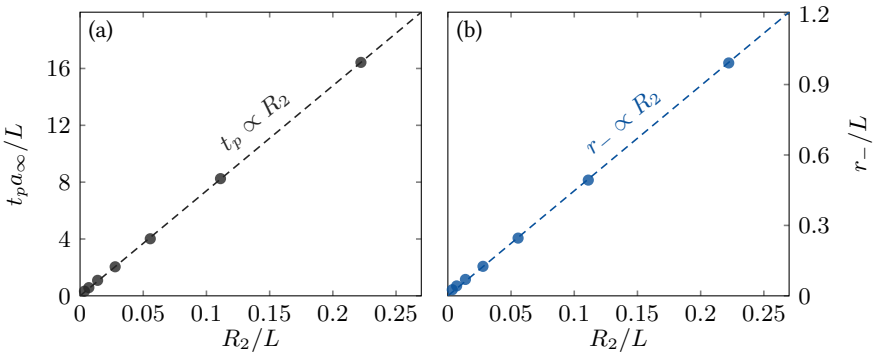

Figure 3.28: Essentially linear relationship of (a) penetration time t_p and (b) position of negative vorticity r_- (3.20) at t_p with respect to the cap radius R_2 in the semi-infinite configuration.

Of course, given the complexity of the flow, additional factors are expected to affect whether collision occurs. The collision model is predicated on vorticity forming into coherent structures before their critical interaction, but the figure 3.26(c) formation-time mechanism can interrupt this process at the larger end and partially account for the weak resistance encountered by the negative vorticity in figure 3.27(b). While it is difficult to determine the relative importance of strength, location, and timing—the three ejection mechanisms of figures 3.26(a–c)—from these observations alone, the outcome is clear: the vorticity from the smaller end is more intense and stays close to the axis in a fast-moving ring that ejects.

3.6.3 Reversal with increasing α

Ejection reversal for $\beta \lesseqgtr 1$ is obvious due to symmetry. However, kernel length (α) can also lead to reversal as seen in figure 3.7. Figure 3.29 compares $\alpha = 3$ to $\alpha = 9$. Figures 3.29(a–b) for $\alpha = 3$ seem to reflect the figure 3.26(c) mechanism: the concentrated negative vorticity penetrates the kernel and passes through the still diffuse positive vorticity. In contrast, the longer $\alpha = 9$ kernel allows structures to form and penetrate at both ends (figures 3.29d–e). The smaller-end vorticity appears more concentrated but is weaker, for reasons discussed in section 3.5, and is subsequently overwhelmed by strong positive vorticity in a reversal of the figure 3.26(a) strength-mismatch mechanism. The result is a change in the ejection direction (figures 3.29c and f). Thus, if the kernel is long enough, t_p for both ends is earlier than their time of interaction, and

ejection depends primarily on relative strengths. For this case, the relative position and coherency of vorticity (figures 3.26b and c) appear to be secondary to this strength asymmetry. As anticipated at $t = 2L/a_\infty$ in figure 3.23, this reversal with respect to α indeed corresponds to a change in the sign of Γ.

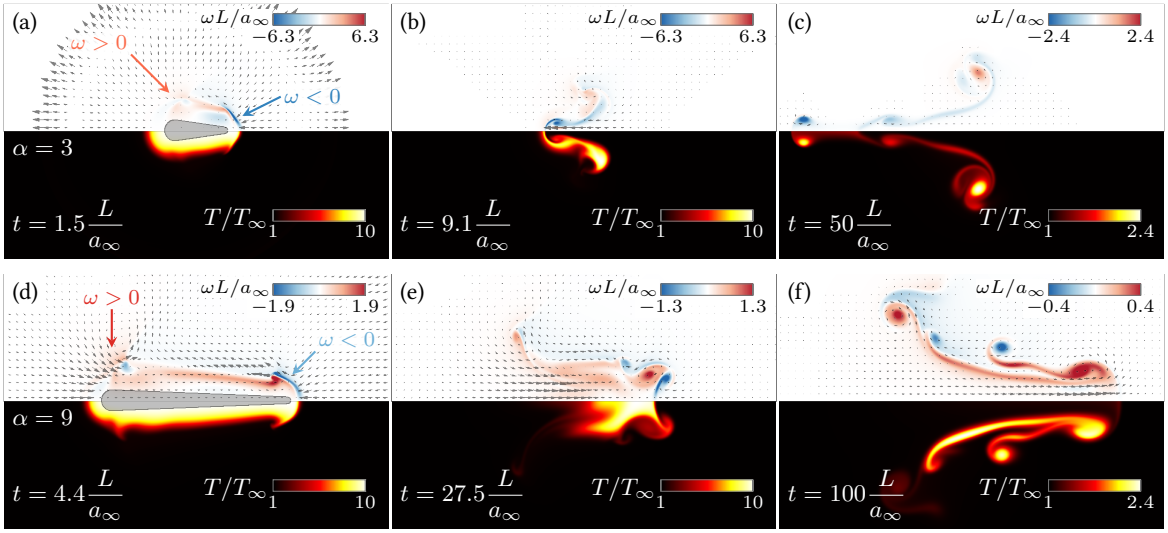

Figure 3.29: The $\alpha = 3$, length-L kernel (a–c) produces a leftward ejection, whereas the $\alpha = 9$, length-$3L$ kernel (d–f) produces a rightward ejection. Initial kernels are shown in grey, both with $\beta = 3$, and vectors correspond to $\rho\boldsymbol{u}$.

Chapter 4

Hydrodynamics of dual-pulse laser-induced breakdowns

4.1 Simultaneous depositions in close proximity

The perfect-gas model (section 3.1) is used to analyze flow characteristics following multiple breakdowns. We first analyze a configuration with two simultaneous, coaxial pulses with a small offset. It is based on the dual-pulse experiment of Limbach [59], for which it was found that ejection is suppressed by adding a 1 mJ femtosecond pulse only 60 ns before a 30 mJ nanosecond pulse, which would otherwise produce an ejection. For the ejection hydrodynamics, 60 ns is essentially negligible, so we use simultaneous model depositions. Though point-to-point comparison is not expected, the present model will be shown to reproduce key features seen in figure 4.1.

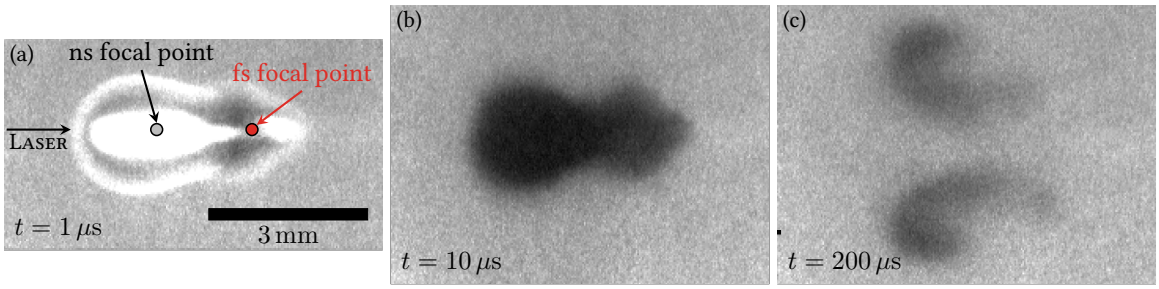

Figure 4.1: Planar Rayleigh scattering measurements of density by Limbach [59], reproduced with permission. Stretching of the original figures has been removed.

Values of α and β are based on available visualizations. An $\alpha = 5$, $\beta = 1$ kernel of length $l = 0.5L$ (half the primary kernel length) is used to model the energy distribution produced by a femtosecond pulse, reflecting

the elongated, approximately symmetric geometry observed [93]. An $\alpha = 4$, $\beta = 3$ kernel of length L is used for the nanosecond pulse based on the asymmetry observed in atmospheric air [6]. While a femtosecond pulse generates lower temperatures than a nanosecond pulse [93, 94], it is unclear whether the smaller kernel in this dual-pulse scenario should also have a correspondingly low temperature, as free electrons from the femtosecond pulse can absorb significant energy from a subsequent pulse, which occured in the figure 4.1 experiments [59]. While a more detailed mapping of laser properties to the ultimate flow pattern would include aspects of this complex laser-plasma coupling, for the present model we use $\Delta e_{\mathrm{LIB}} = 55 e_\infty$ for both kernels as an approximation. The deposited energies are $E = 2.93 \rho_\infty a_\infty^2 L^3$ for the larger kernel and $E = 0.44 \rho_\infty a_\infty^2 L^3$ for the smaller one, which correspond to 3.3 mJ and 0.50 mJ for $L = 2$ mm and atmospheric air.

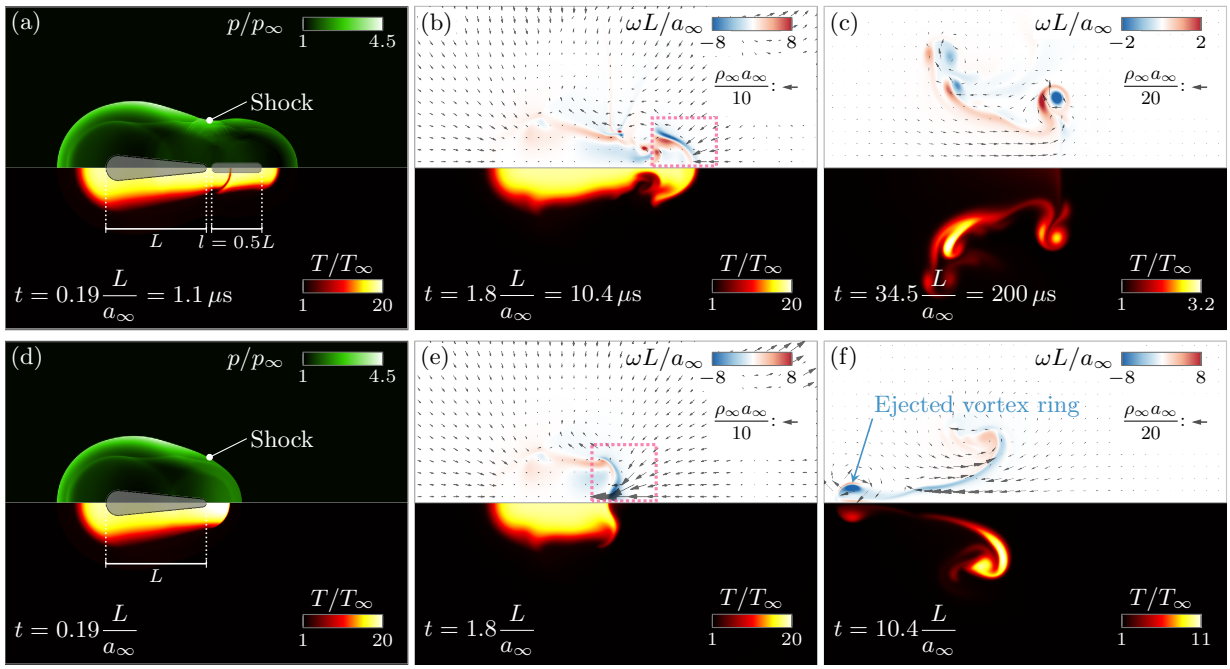

Figure 4.2: Evolution of (a–c) dual-pulse and (d–f) single-pulse cases. Dimensional values correspond to $L = 2$ mm and $p_\infty = 1$ atm, $T_\infty = 298$ K air. Momentum vectors are shown due to the density variation, and initial kernels are shown in grey.

Figure 4.2 compares the dual-pulse case (a–c) to a case with just the higher-energy nanosecond pulse (d–f). At early times (figures 4.2a and d), the kernel expands and cools rapidly from its initial peak of $56T_\infty$, producing a shock that decouples from the hot gas and propagates outward. The irregular shock shape in figure 4.2(a) resembles the motivating experiment (figure 4.1a). This leaves behind the vorticity

$$\omega \equiv \frac{\partial u_r}{\partial x} - \frac{\partial u_x}{\partial r}$$

shown in figures 4.2(b) and (e). In the single-pulse case, a region of inflowing momentum penetrates leftward into the hot kernel, consistent with the expected leftward auto-advection of the associated negative vorticity. An analogous structure can be seen in the dual-pulse case, though it is less pronounced and located outside the hot remnants of the secondary kernel, as indicated by the dotted box. At later times (figures 4.2c and f), the vorticity produced by the single pulse collects and ejects as a vortex ring, whereas no clear ejection can be seen in the dual-pulse case. Instead cold ambient gas pushes hot gas away from the $r = 0$ axis (figure 4.2c), as also observed experimentally (figure 4.1c). The single-pulse case (figures 4.2d–f) is shown here for comparison.

Perfect agreement with the experiment is not expected, of course, since our model is based on estimation of the early-time energy distribution. While direct sensitivity to short time delays (e.g. $\Delta t = 60\,\mathrm{ns}$) would not be reproduced in detail without modeling the complex plasma physics, the key flow patterns we target for varying focal-point offsets such as observed by Limbach [59], particularly in cases of non-overlapping kernels, are clearly reproducible with the present deposition model and the selected energy distribution.

The phenomenology of figure 4.2 is reflected in the development of the net circulation,

$$\Gamma(t) \equiv \int\int \omega(t)\,\mathrm{d}x\,\mathrm{d}r, \tag{4.1}$$

shown in figure 4.3. In both cases rapid vorticity generation occurs for $t \lesssim 2L/a_\infty$ before the circulation becomes constant; at later times, $\Gamma < 0$ for the single-pulse case corresponds to a leftward ejection whereas the weaker $\Gamma > 0$ for the dual-pulse case corresponds to the suppressed ejection.

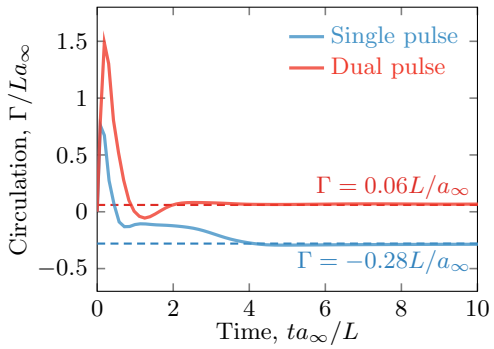

Figure 4.3: Net circulation (4.1) for the single- and dual-pulse cases in figure 4.2.

A transition from non-ejecting to ejecting behavior is realized by reducing the energy of the weaker pulse. This is done by decreasing its length l while maintaining its aspect ratio, consistent with observations that a weaker pulse typically results in a smaller volume of heated gas, with mild changes to its overall geometry

for either femtosecond [93] or nanosecond [54, 55, 57] pulses. Figure 4.4 shows that weakening the secondary pulse leads to the expected leftward ejection and associated increase in negative circulation, generated by the post-shock rarefaction mechanism of single pulses [25, 27].

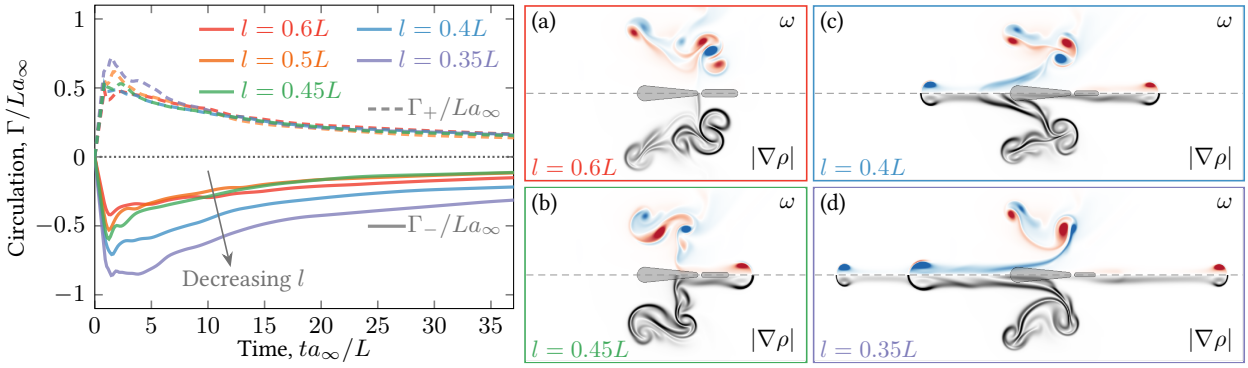

Figure 4.4: Circulation time traces and $t = 35L/a_\infty$ visualizations of ω and $|\nabla\rho|$ for several dual-pulse cases with $l \in [0.35L, 0.6L]$, where $\Gamma_\pm \equiv \int\int_{\omega \gtrless 0} \omega \, \mathrm{d}x \, \mathrm{d}r$.

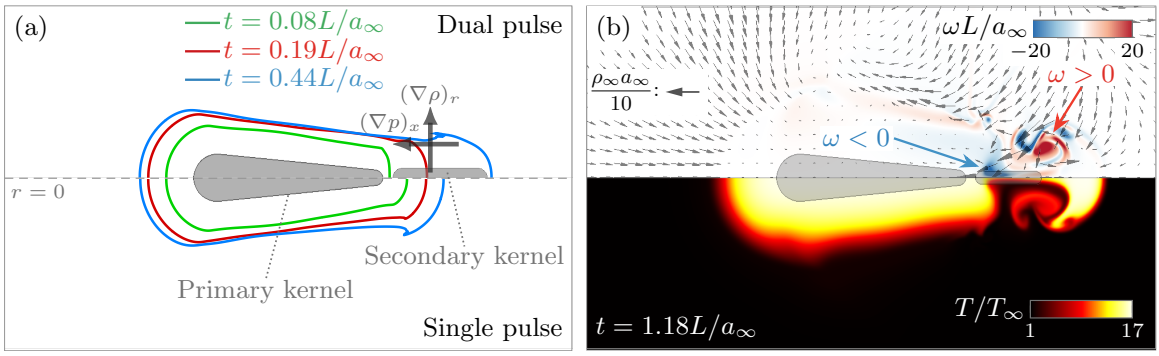

Figure 4.5: (a) Evolution of the primary kernel's boundary, defined by an advected scalar, for the figure 4.2 cases, with $(\nabla\rho \times \nabla p)_\theta > 0$ indicated schematically for the dual-pulse case, where θ is the cylindrical polar angle. (b) Flow at $t = 1.18L/a_\infty$ for the $l = 0.35L$ case. Vectors correspond to $\rho\boldsymbol{u}$.

For some cases the model curiously predicts an additional rightward ejection (figures 4.4b–d), resembling the "four-lobe" pattern observed in experiments [95]. Its source can be traced to the early expansion of the primary kernel, visualized in figure 4.5(a): for the dual-pulse case, the kernel expands farther because it is opposed by only the lower-density gas that has been expanded by the secondary kernel. The pressure gradient driving the primary kernel's expansion thus accelerates lower-density gas to a greater velocity, producing positive vorticity by baroclinic torque. This $\omega > 0$ can be seen in figure 4.5(b) in addition to leftward-advecting $\omega < 0$ fluid. The mechanism is anticipated to occur for all cases in figure 4.4; the maximum length of the kernel (figure 4.5a) differs by less than 5%, suggesting that even the smallest $l \in [0.35L, 0.6L]$ is sufficient to promote expansion of the primary kernel. This is also consistent with Γ_+ being insensitive to l (figure 4.4).

While this enhanced-expansion mechanism appears to produce the necessary positive vorticity, it is insuf-

ficient for a rightward ejection to form. For a large secondary kernel, this vorticity is opposed by negative vorticity produced at its right end (e.g., figure 4.2b), but a sufficiently small kernel is unable to generate enough counter-rotating flow, due to its small size (section 3.4.5), and the rightward ejection prevails (figures 4.5b and 4.4d). This mechanism is also expected to contribute to suppression of the leftward ejection (figures 4.2a–c).

4.2 Time-delayed and offset depositions

This configuration is motivated by the experiments of Jun et al. [69], in which a single laser beam focused in a fuel spray is used to produced multiple points of plasma initiation, occuring essentially simultaneously (figure 4.6a). We start with a three-breakdown case, modeled as initially non-overlapping kernels—two with $\alpha = 1.15$, $\beta = 1$, and length $0.62L$, and one with $\alpha = 2.11$, $\beta = 2.00$, and length $0.98L$—whose dimensions, relative position, and energies are approximated from shadowgraph images [69]. There is no expectation of precise agreement, given possible interference from fuel droplets and sensitivity of the ejection to the early-time plasma state and other uncertainties. For example, while each simulated kernel in figure 4.6 is approximately 20 times more massive than a single fuel droplet of diameter $50\,\mu$m [68], the collective effect of multiple high-density droplets could bias the kernel expansions and alter the ejection pattern due to their increased ability to resist breakdown-induced flow. The present model nonetheless reproduces several key features. By $t = 1\,\mu$s (figure 4.6a and d), the kernels' boundaries and blast waves interact, which results in the multiple intersecting shocks seen at $t = 5\,\mu$s (figure 4.6e). Many of these detailed structures match those observed (figure 4.6b). At $t = 25\,\mu$s, both also show a vortex-ring-like structure between the remnants of the two leftmost kernels. Though for this particular simulation the rightmost kernel does not evolve exactly as observed (figure 4.6c), which leads to an apparent reversed ejection away from the laser source, the present model will be shown to produce this general behavior for the dual-pulse configuration analyzed subsequently. Importantly, the experiment also indicates that the flow is largely axisymmetric for the time interval considered.

To understand interactions, we focus on a configuration with just two energy depositions. These are separated by time τ and offset by d (figure 4.7), where $d < 0$ corresponds to the second kernel being deposited to the left of the first. A mildly asymmetric geometry ($\alpha = 3$ and $\beta = 1.5$) is used for all cases, which produces a leftward ejection for a single pulse. Conclusions regarding mechanisms for the phenomenologies analyzed are not expected to be particularly sensitive to this choice.

Figure 4.8 compares two configurations, both with $\tau = 3L/a_\infty$ and energies $E_\mathrm{I} = 7.0\rho_\infty a_\infty^2 L^3$ and

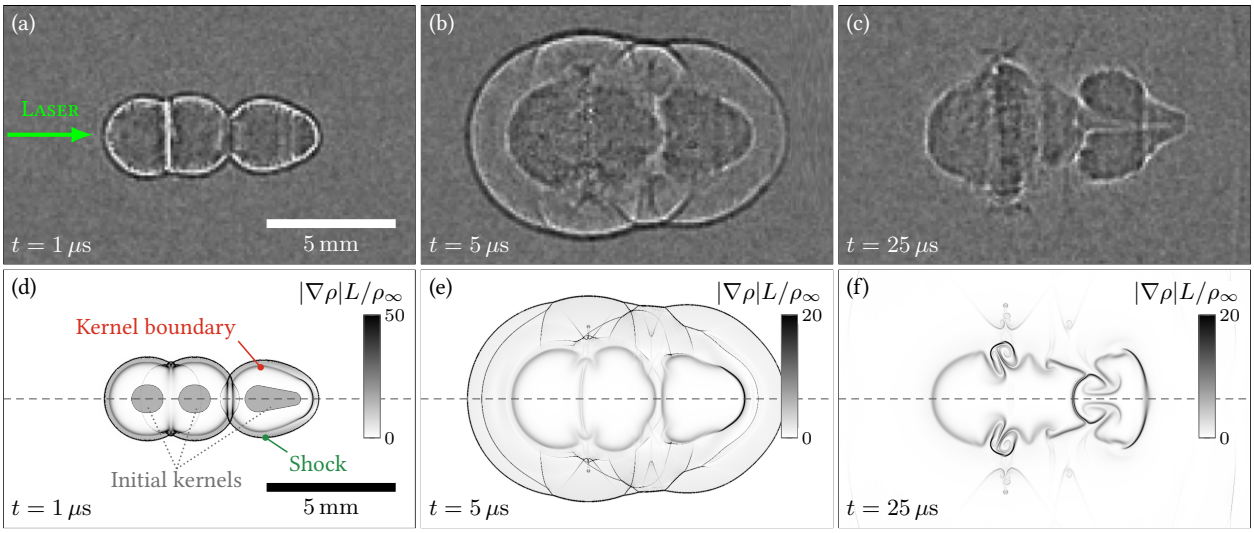

Figure 4.6: Comparison of $|\nabla\rho|$ with shadowgraph images by Jun et al. [69] in a configuration with three apparent plasma initiation points.

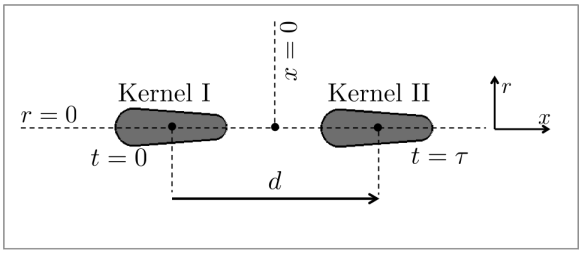

Figure 4.7: Dual-pulse configuration with temporal delay τ and relative kernel position d.

$E_{\mathrm{II}} = 6.8\rho_\infty a_\infty^2 L^3$ (7.9 mJ and 7.7 mJ for $L = 2$ mm in atmospheric air), which differ only slightly due to the reduced density in the rarefaction behind the shock of the first kernel. With $d = 3L$, both kernels eject leftward, though kernel II's ejection is weaker (figure 4.8a). In contrast a smaller $2L$ separation leads to kernel I ejecting more strongly and kernel II's ejection reversing and propagating rightward (figure 4.8b).

Closer inspection of the figure 4.8(b) case, shown in figure 4.9, suggests that the shock contributes to this phenomenology. Shortly after the second kernel is deposited, its shock passes through the first (figure 4.9a), producing negative vorticity at the boundary of the hot gas. Rarefactions are reflected and, in this case, rightward-propagating Mach-disk-like structures [96] form near $r = 0$ (figure 4.9b inset) and leave behind positive vorticity as they pass through the second kernel (figure 4.9c). This vorticity subsequently forms into the reversed ejection seen in figure 4.8(b).

The shock–kernel interactions can be seen in the time histories of the net circulation in $x > 0$ and $x < 0$ (figure 4.10), which correspond to vorticity generated in each kernel. For the $d = 2L$ case, sudden generation of negative vorticity in kernel I at $t \approx 3.5L/a_\infty$ is caused by the shock from the second deposition, followed by a corresponding sharp increase in the kernel II's circulation that coincides with the passage of the Mach-disk-

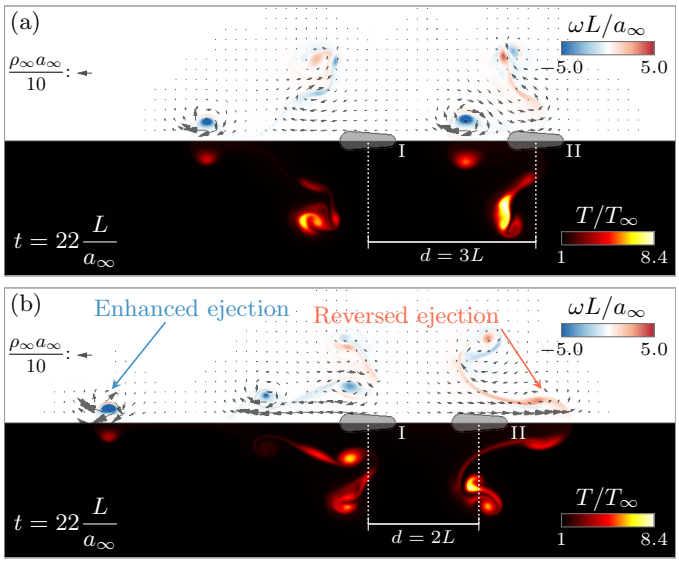

Figure 4.8: With $\tau = 3L/a_\infty$, (a) $d = 3L$ leads to two leftward ejections, whereas (b) $d = 2L$ leads to a reversed ejection. Vectors indicate $\rho\boldsymbol{u}$.

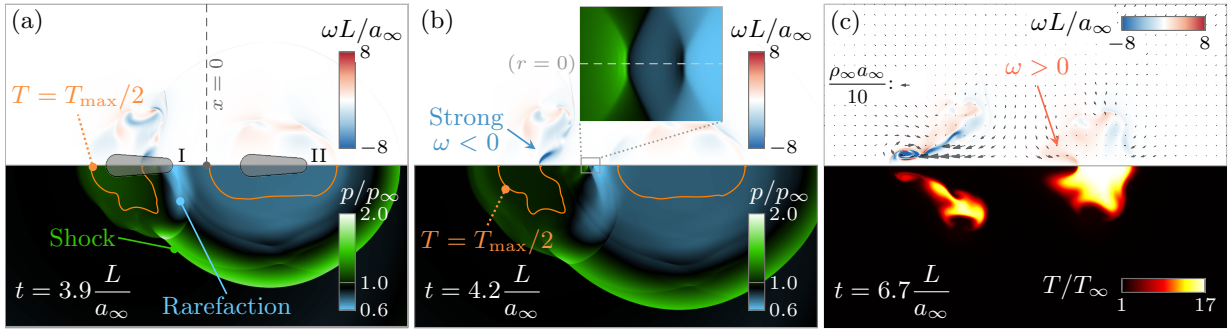

Figure 4.9: Case with $d = 2L$, $\tau = 3L/a_\infty$ for times $t =$ (a) $3.9L/a_\infty$, (b) $4.2L/a_\infty$, and (c) $6.7L/a_\infty$. Vectors correspond to $\rho\boldsymbol{u}$.

like shocks. The differing signs of $\Gamma_{\{x>0\}} > 0$ and $\Gamma_{\{x<0\}} < 0$ are consistent with the apparent auto-advection of vorticity and the respective ejection directions. For the $d = 3L$ case, vorticity generation by the shock passing through kernel I is weaker, due to the greater distance traveled, with a correspondingly weak effect of the subsequent reflection towards kernel II. Both kernels have net negative circulation after their interaction, with the weaker $\Gamma_{\{x>0\}}$ corresponding to the weaker ejection seen in figure 4.8(a).

Figure 4.11 shows the ejection phenomenology across a broader range of d and τ. In all cases, the second kernel is formed inside the first kernel's shock but at a sufficient distance so as not to overlap with its boundary. The shock-generation mechanism described above produces vorticity associated with the rightward reversal for $d = -2L$ and strong leftward ejection for $d = 2L$, both with $\tau = 1.5L/a_\infty$ (figures 4.11c and d). Though less pronounced, this mode of vorticity generation occurs for the more distal $d = \pm 3L$ cases as well, leading to the suppression of the $x > 0$ kernel's ejection for $d = -3L$ (figure 4.11a).

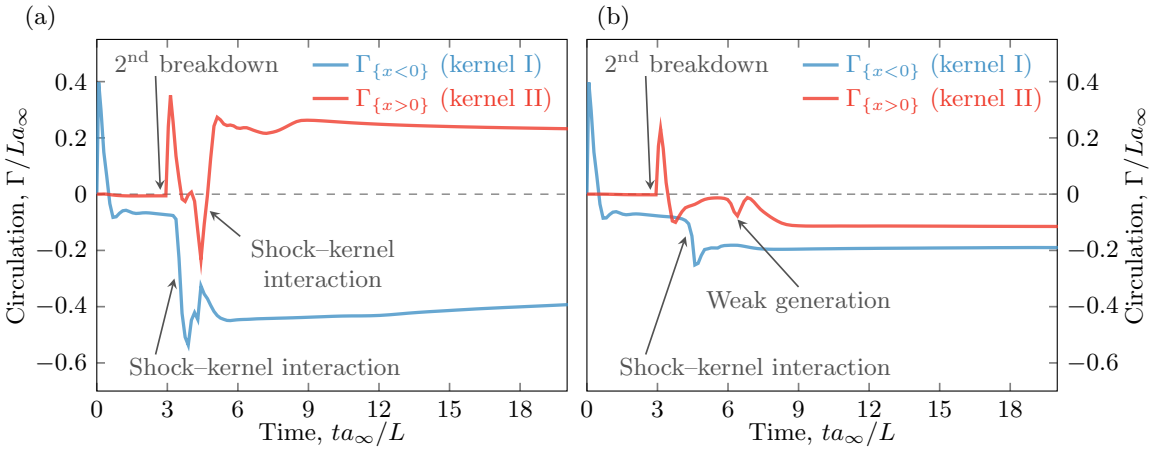

Figure 4.10: Circulation in $x > 0$ and $x < 0$ for (a) $d = 2L$ and (b) $d = 3L$, both with $\tau = 3L/a_\infty$.

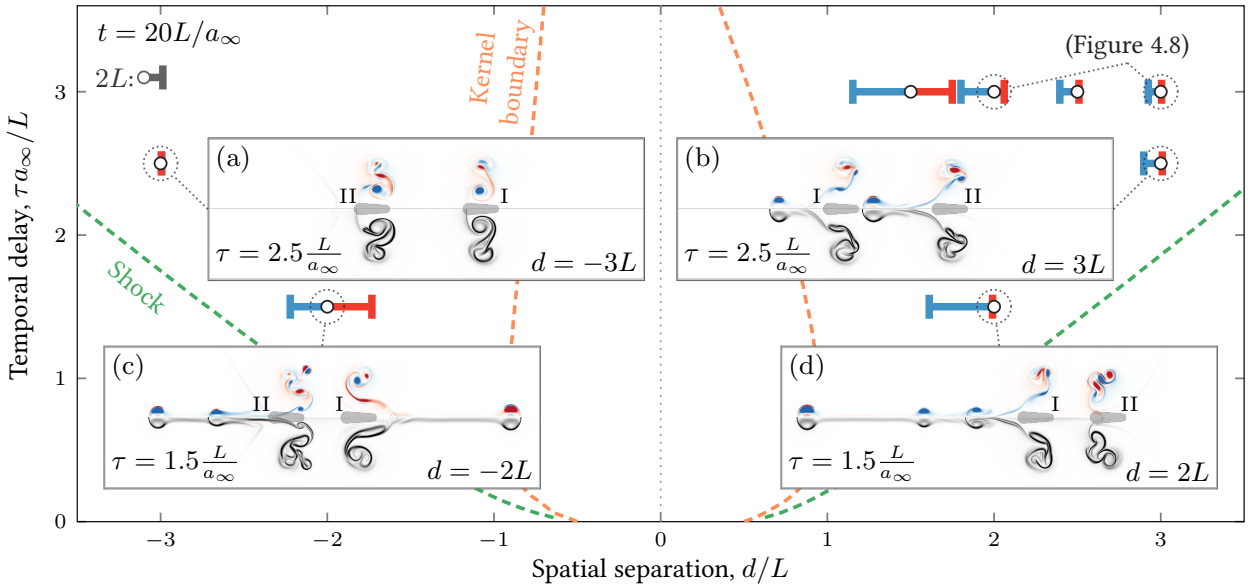

Figure 4.11: Ejection character, visualized by ω and $|\nabla\rho|$ at $t = 20L/a_\infty$. At each (d, τ), the blue (red) line corresponds to the farthest negative-x (positive-x) location of $T > 2T_\infty$ gas relative to the $x < 0$ ($x > 0$) kernel's initial position, shown in grey. The x–t trajectory of the $r = 0$ axial extents of the kernel boundary and shock for a single pulse are plotted for reference. Cases in figure 4.8 are also indicated.

More curious is the apparent $d \lessgtr 0$ asymmetry: whereas $d = -3L$ results in neither kernel ejecting, $d = 3L$ leads to two ejections, and reversal occurs for $d = -2L$ but not $d = 2L$. The kernel's own asymmetry is clearly important: for example, kernel I's leftward ejection is only enhanced by the shock if kernel II is deposited to its right ($d > 0$) and is suppressed or even reversed if kernel II is deposited to its left ($d < 0$). Closer inspection of the figure 4.11(a) case shortly before the second deposition, shown in figure 4.12, also suggests that the pressure distribution behind the shock from the first kernel biases the evolution of the second kernel. The trailing rarefaction, previously shown to be the principal mechanism of ejection for a single pulse [25, 27], also exerts a torque on the second kernel. As the shock and its rarefaction propagate outward, the associated

pressure gradient suppresses a leftward ejection, augmenting positive vorticity generation on the left end of the second kernel and weakening negative generation on its right. Though weak for $\tau = 2.5L/a_\infty$, the flow induced by the shock's rarefaction, also shown in figure 4.12, further biases the second kernel's evolution. This mechanism is also consistent with the slightly enhanced leftward ejection of kernel II compared to its partner for $d = 3L$ (figure 4.11b), for which the relative position of the shock and second kernel are the reverse of figure 4.12. Its effect is anticipated to be more pronounced for $d = \pm 2L$, as the earlier $\tau = 1.5L/a_\infty$ deposition occurs when the shock and its rarefaction are stronger than that shown in figure 4.12. While the post-shock density field introduces mild non-uniformity in the energy deposited, this is not expected to be a primary cause of the observed phenomenology; corresponding simulations of a single kernel in a quiescent flow with axially non-uniform background density do not produce flow consistent with that analyzed here.

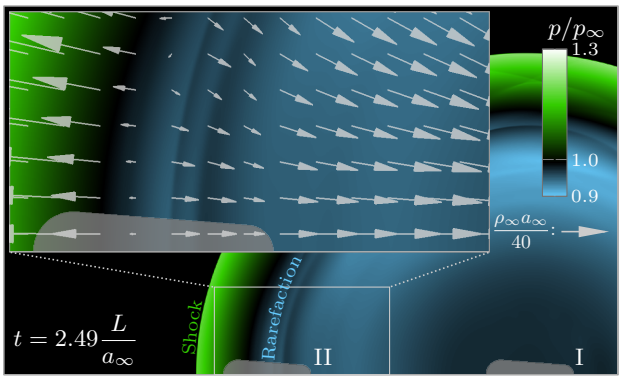

Figure 4.12: Pressure and momentum vectors shortly before the $d = -3L$ deposition at $\tau = 2.5L/a_\infty$; the shock is followed by a rarefaction zone with sub-ambient pressure.

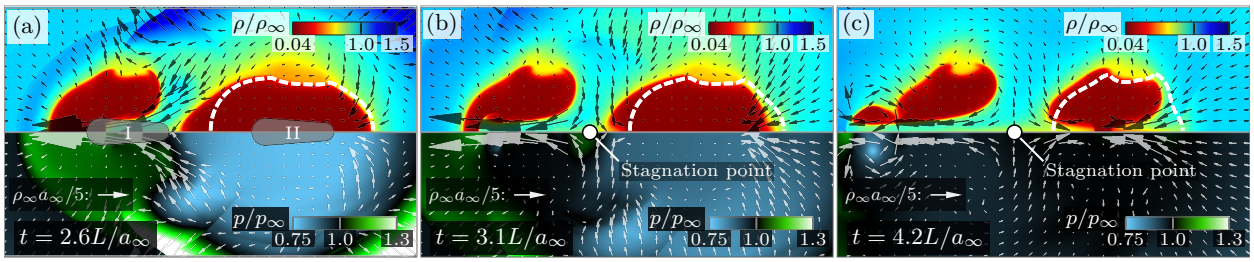

Figure 4.13: Case with $d = 2L$, $\tau = 1.5L/a_\infty$ at times (a) $2.6L/a_\infty$, (b) $3.1L/a_\infty$, and (c) $4.2L/a_\infty$. The $\rho = 0.3\rho_\infty$ contour for a corresponding single pulse is indicated by the dashed line. Vectors indicate $\rho\boldsymbol{u}$. The stagnation point is marked in (b) and (c).

This mechanism appears to be countered by another effect for the proximal $d = \pm 2L$ cases that leads to kernel II's ejection being enhanced for $d = -2L$ and suppressed for $d = 2L$ (figures 4.11c and d). For the $d = 2L$ case, prominent flow into the inter-kernel region is seen at $t = 2.6L/a_\infty$ (figure 4.13a), consistent with kernel I's eventual strong ejection due to shock-enhancement (figure 4.11d). Comparison with the corresponding single-pulse case indicates greater leftward protrusion of kernel II near $r = 0$, an artifact of its expansion towards the low-density remnants of the first kernel, and narrowing of the inter-kernel space. The

flow diverges at a stagnation point in this dense fluid, which coincides with elevated pressure (figure 4.13b). The ensuing pronounced rightward flow near $r = 0$ (figure 4.13c), absent in the single-pulse case, opposes the concurrent leftward flow in kernel II. Though the latter is enhanced by the rarefaction mechanism shown in figure 4.12 and would otherwise produce a leftward ejection (e.g., kernel II in figure 4.11b), it is ultimately suppressed for this $d = 2L$ case, as seen in figure 4.11(d). For the $d = -2L$ counterpart, this effect enhances kernel II's leftward ejection (figure 4.11c). It is also expected to contribute to the ejection reversal for $d = 2L$, $\tau = 3L/a_\infty$ (figure 4.9).

Though the axisymmetric constraint presumably leads to more organized flow and farther late-time vortex propagation, the core ejection phemenologies depend primarily on mechanisms that occur earlier in time, before $t \lesssim 7L/a_\infty$ ($t \lesssim 40\,\mu$s in atmospheric air), when the effect of three-dimensional instabilities are anticipated to be secondary, as evidenced by figure 4.6. We also note that while free electrons from the first breakdown can absorb laser radiation from the second pulse [57, 59], this would be a small effect for the present configuration with spatially non-overlapping depositions separated by a time delay $\tau \geq 1.5L/a_\infty = 8.7\,\mu$s, which is sufficient for significant electron-ion recombination to occur before the second pulse [7, 62, 97].

A broadly applicable criterion that predicts the flow response, while motivated by these results, has been difficult to obtain, even for a single pulse for which a single mechanism of vorticity generation is dominant. In the dual-pulse configurations considered, multiple mechanisms appear to contribute to the flow pattern, and some are prominent only when the kernels are in close proximity. It is also unclear what flow quantity would best support such a criterion: while vorticity is closely tied to the ejection behavior for a single pulse and some dual-pulse cases, certain dynamics (e.g. figure 4.13) may be best explained with momentum-based arguments. We note that there exist analytical estimates of circulation generated in a related cylindrical-channel configuration [24], though the analysis does not extend to the present case.

4.3 Burning enhancement with dual pulses

To quantify the effect of varying d and τ on flame kernel growth, dual energy kernels are deposited in a lean H_2–O_2 mixture at $p_\infty = 1\,$atm with fuel–oxidizer stoichiometric ratio $\phi = 0.15$. The combustion physics are modeled with a detailed 9-species, 21-reaction hydrogen-combustion mechanism [98], temperature-dependent mixture-averaged transport properties, and polynomial-fitted thermodynamic properties. This model is used extensively in chapter 6 and its full description is deferred to section 6.1.1.

The four cases shown in figure 4.14 correspond to the perfect-gas cases in figure 4.11 with $L = 2\,$mm and $E_I = E_{II} = 12\,$mJ. The flame surface is highlighted by the mass fraction Y_{HO_2}, which primarily resides in the

reaction zone. It is apparent that controlling d and τ can have a pronounced effect on the morphology and size of the flame. In particular, cases in which strong ejections are produced in a perfect gas (figures 4.11c–d) also correspond to larger flame kernels in a combustible mixture (figures 4.14c–d) due to the broader distribution of hot gas. This increases the flame's surface area and results in an accelerated burning rate, as evidenced in figure 4.15. By $t = 270\,\mu$s, the $d = \pm 4\,$mm cases have produced 47% more H_2O than the $d = -6\,$mm case. All dual-pulse cases burn faster than a single-pulse case of equal total energy $E = 24\,$mJ, which is less effective at spreading heated gas, and the figure 4.14(c) case burns 2.2 times faster. These results support the proposition, based on recent experimental observations [62, 63], that increasing the flame kernel surface area is a primary mechanism by which ignition can be enhanced with multiple depositions.

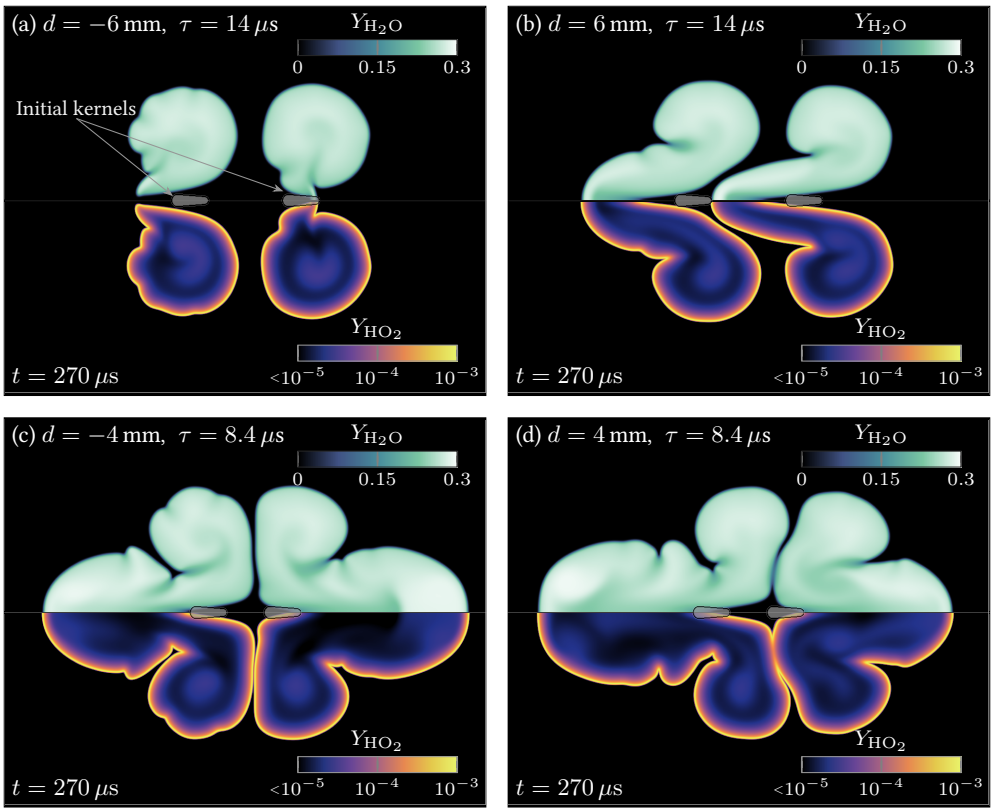

Figure 4.14: Flame kernels at $t = 270\,\mu$s, visualized by Y_{H_2O} and Y_{HO_2}, produced by dual-pulses in a $\phi = 0.15$ H_2–O_2 mixture for four cases (a–d) corresponding to figure 4.11(a–d), respectively, with $L = 2\,$mm and $p_\infty = 1\,$atm. Initial kernels are shown in grey; each frame is 26 mm × 20.8 mm.

This sensitivity to laser-pulse timing and placement offers opportunities to tailor the post-breakdown hydrodynamics for combustion applications, as configurations that lead to a broader distribution of hot gas are anticipated to enhance burning rate by forming larger flame kernels. Splitting the energy among more than two pulses could yield further improvements, with the trade-off that absorption tends to degrade for weaker pulses and diffusive losses occur more rapidly for smaller kernels.

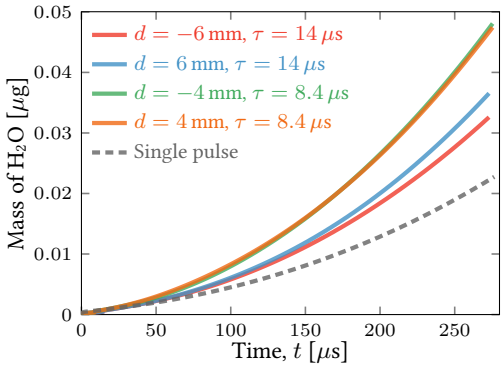

Figure 4.15: Mass of H_2O produced for the four dual-pulse cases in figure 4.14, compared with a single pulse of equal total energy $E = 24\,\text{mJ}$.

Chapter 5

Nonequilibrium-plasma effects on post-breakdown hydrodynamics

5.1 Model formulation

5.1.1 Nonequilibrium plasma model

The nonequilibrium plasma model consists of a two-temperature, three-species singly ionized gas with atom- and electron-impact ionization processes,

$$\mathrm{A} + \mathrm{e}^- \rightleftharpoons \mathrm{A}^+ + \mathrm{e}^- + \mathrm{e}^- \tag{5.1}$$

$$\mathrm{A} + \mathrm{A} \rightleftharpoons \mathrm{A}^+ + \mathrm{e}^- + \mathrm{A} \tag{5.2}$$

The monatomic species A and its ion A^+ have heavy-particle temperature T, and free electrons have temperature T_e. The governing equations are

$$\frac{\partial \rho}{\partial t} + \nabla \cdot (\rho \boldsymbol{u}) = 0 \tag{5.3}$$

$$\frac{\partial \rho \boldsymbol{u}}{\partial t} + \nabla \cdot (\rho \boldsymbol{u}\boldsymbol{u}) - \nabla \cdot (-p\boldsymbol{I} + \boldsymbol{\tau}) = \boldsymbol{0}, \tag{5.4}$$

$$\frac{\partial \rho(e+|\boldsymbol{u}|^2/2)}{\partial t} + \nabla \cdot [\rho(e+|\boldsymbol{u}|^2/2)\boldsymbol{u}] - \nabla \cdot [(-p\boldsymbol{I}+\boldsymbol{\tau})\boldsymbol{u}] + \nabla \cdot \boldsymbol{q} = 0 \tag{5.5}$$

$$\frac{\partial \rho e_{el}}{\partial t} + \nabla \cdot (\rho e_{el}\boldsymbol{u}) + \nabla \cdot (p_e \boldsymbol{u}) + \nabla \cdot \boldsymbol{q}_e = \boldsymbol{u} \cdot \nabla p_e + \frac{3}{2} n_e k_b (T_h - T_e) \left(\frac{1}{\tau_{e\mathrm{A}^+}} + \frac{1}{\tau_{e\mathrm{A}}} \right) - I_{\mathrm{A}} \dot{n}_{e,1} \tag{5.6}$$

$$\frac{\partial \rho Y_{\mathrm{A}^+}}{\partial t} + \nabla \cdot (\rho Y_{\mathrm{A}^+}\boldsymbol{u}) + \nabla \cdot (\rho Y_{\mathrm{A}^+}\boldsymbol{V}_{\mathrm{A}^+}) = W_{\mathrm{A}^+}\dot{\omega}_{\mathrm{A}^+} \tag{5.7}$$

$$p = \rho k_b \left(\frac{Y_e}{m_e} T_e + \frac{Y_{\mathrm{A}^+}}{m_{\mathrm{A}^+}} T_h + \frac{Y_{\mathrm{A}}}{m_{\mathrm{A}}} T_h \right) \tag{5.8}$$

where n_k, $\dot{\omega}_k = \dot{n}_k/\mathcal{N}$, m_k, $p_e = \rho Y_e \hat{k}_b T_e/m_e$, and I_{A} are the species number density, molar production rate, atomic mass, electron pressure, ionization potential of A [99, 100, 101]; $\dot{n}_{e,1}$ corresponds to the electrons produced by only electron-impact ionization (5.1) [102]. Argon properties are used throughout. The Boltzmann and Avogadro constants are denoted by k_b and $\mathcal{N}$, respectively. Neglected charge separation effects are not expected to be significant [101], particularly in the absence of an externally applied electric field during the post-breakdown dynamics, so charge neutrality is assumed and $n_e = n_{\mathrm{A}^+}$. The internal energy $e = e_f + e_h + e_{el}$ includes the formation, heavy-particle, and electronic energies:

$$e_f = Y_{\mathrm{A}^+} \frac{I_{\mathrm{A}}}{m_{\mathrm{A}^+}}, \qquad e_h = \frac{3}{2} \left(\frac{Y_{\mathrm{A}}}{m_{\mathrm{A}}} + \frac{Y_{\mathrm{A}^+}}{m_{\mathrm{A}^+}} \right) k_b T_h, \qquad e_{el} = \sum_k Y_k e_{e,k}$$

The electronic energy e_{el} accounts for both translation of free electrons and excitation of heavy species to a single energy level ε_k, and $e_{e,k}$ is the electronic energy of the k-th species [103]:

$$e_{e,e} = \frac{3}{2} \frac{k_b T_e}{m_e}, \qquad \text{and} \qquad e_{e,k} = \frac{g_k^1 \exp\left(-\frac{\varepsilon_k}{k_b T_e}\right)}{g_k^0 + g_k^1 \exp\left(-\frac{\varepsilon_k}{k_b T_e}\right)} \frac{\varepsilon_k}{m_k} \quad \text{for} \quad k \in \{\mathrm{A}, \mathrm{A}^+\},$$

where g_k^l is the degeneracy of the l-th energy level for the k-th species [104] (table 5.1).

	g_k^0	g_k^1	ε_k	I_k
A	1	12	11.5 eV	15.8 eV
A^+	6	2	13.5 eV	Not used

Table 5.1: Degeneracies and energy levels for argon, grouped approximately based on Kramida et al. [104].

The species internal energy e_k is

$$e_e = \frac{3}{2}\frac{k_b T_e}{m_e}, \qquad e_{\mathrm{A}} = \frac{3}{2}\frac{k_b T_h}{m_{\mathrm{A}}} + e_{e,\mathrm{A}}, \qquad e_{\mathrm{A}^+} = \frac{3}{2}\frac{k_b T_h}{m_{\mathrm{A}^+}} + \frac{I_{\mathrm{A}}}{m_{\mathrm{A}^+}} + e_{e,\mathrm{A}^+},$$

which satisfies $e = e_f + e_h + e_{el} = \sum_k Y_k e_k$. For A and A^+ the electronic enthalpy $h_{e,k}$ is equal to $e_{e,k}$, and for electrons $h_{e,e} = e_{e,e} + k_b T_e/m_e$ [101]. The translational and electronic specific heat are, respectively,

$$c_v^t = \sum_k Y_k \frac{3}{2}\frac{k_b}{m_k}, \qquad c_v^e = \sum_k Y_k \frac{\partial e_{e,k}}{\partial T_e} \tag{5.9}$$

The stress tensor and heat flux vectors are

$$\boldsymbol{\tau} = \mu(\nabla \boldsymbol{u} + \nabla \boldsymbol{u}^T) - \left(\mu_B - \frac{2}{3}\mu\right)(\nabla \cdot \boldsymbol{u})\boldsymbol{I},$$

$$\boldsymbol{q} = -\lambda_h \nabla T_h - \lambda_{el}\nabla T_e + \rho \sum_k Y_k h_k \boldsymbol{V}_k \qquad \text{and} \qquad \boldsymbol{q}_e = -\lambda_{el}\nabla T_e + \rho \sum_k Y_k h_{e,k} \boldsymbol{V}_k \,.$$

Physical bulk viscosity is zero for an ideal monatomic gas [103], though we use an artificial-viscosity model to stabilize shocks,

$$\mu_B = \overline{C\rho |D^4(\nabla \cdot \boldsymbol{u}) H(-\nabla \cdot \boldsymbol{u})|}\,, \tag{5.10}$$

where $C = 7.0$ is a parameter, H is the Heaviside step function, D^4 is a mesh-dependent biharmonic-like operator, and the overbar denotes Gaussian filtering; μ_B is strongly sensitive to gradients of dilatation and essentially negligible everywhere except the shock front [105, 106]. The Wilke mixture rule [107] is used for the shear viscosity:

$$\mu = \sum_{k=1}^{N} \frac{X_k \mu_k}{\sum_{j=1}^{N} X_j \frac{\left[1+(\mu_k/\mu_j)^{1/2}(W_j/W_k)^{1/4}\right]^2}{\sqrt{8(1+W_k/W_j)}}}$$

The heavy-particle thermal conductivity λ_h is computed without accounting for interactions between electron

and heavy particles, which have a negligible effect on the velocity distribution of heavy particles due to their large mass discrepancy, and further neglecting ion contributions results in $\lambda_h = X_\mathrm{A}\lambda_\mathrm{A}$ [108]. Similarly, only the free-electron contribution to the electronic thermal conductivity is included, so $\lambda_{el} = X_e\lambda_e$. The species viscosity, species thermal conductivity, and binary diffusion coefficients are modeled as

$$\mu_k = \frac{5}{16}\frac{\sqrt{\pi m_k k_b T}}{\overline{Q}^{(2,2)}_{kk}}, \qquad \lambda_k = \frac{15}{4}\frac{k_b}{m_k}\mu_k, \qquad \text{and} \qquad \mathcal{D}_{kl} = \frac{3}{8}\frac{k_b T}{p}\sqrt{\frac{\pi k_b T(m_k + m_l)}{2m_k m_l}}\frac{1}{\overline{Q}^{(1,1)}_{kl}},$$

where $T = T_e$ for electron properties and electron–heavy interactions, and $T = T_h$ otherwise [109]. The collision integrals are

$$\overline{Q}^{(l,s)}_{ij} = \frac{4(l+1)}{(s+1)!\,[2l+1-(-1)^l]}\int_0^\infty z^{2s+3}\exp(-z^2)Q^l_{ij}(z)\,\mathrm{d}z \tag{5.11}$$

where $Q^l_{ij}(g) = 2\pi\int_0^\infty(1-\cos^l\chi)\,\sigma(g,\chi)\sin\chi\,\mathrm{d}\chi$ is the momentum-transfer cross section for $l = 1$ and the viscosity cross section for $l = 2$; χ, g, and $\sigma(g,\chi)$ correspond respectively to the collision scattering angle, relative velocity magnitude, and differential cross section, and $z^2 = m_i m_j g^2/2k_b T(m_i + m_j)$ [8, 103, 109]. A constant, representative value is used for $\overline{Q}^{(1,1)}_{\mathrm{AA}^+} = 87.0\,\text{Å}^2$ based on calculations at $T = 10\,000\,\mathrm{K}$ by Devoto [110], and $\overline{Q}^{(1,1)}_{e\mathrm{A}}$ is approximated by an empirical fit [111]:

$$\overline{Q}^{(1,1)}_{e\mathrm{A}} = \begin{cases} \left(0.713 - 4.5\times10^{-4}T_e + 1.5\times10^{-7}T_e^2\right)\times\text{Å}^2, & T_e < 3000\,\mathrm{K} \\ \left(-0.488 + 3.96\times10^{-4}T_e\right)\times\text{Å}^2, & T_e \geq 3000\,\mathrm{K} \end{cases}$$

For interactions between electrons and ions, we use

$$\overline{Q}^{(1,1)}_{e\mathrm{A}^+} = \frac{2\pi\epsilon^4}{9(k_b T_e)^2}\log\left(\frac{9k_b^3 T_e^3}{4\pi\epsilon^6 n_e}\right),$$

where $\epsilon^2 \equiv k_e q_e^2$, $k_e = 8.987\times10^9\,\mathrm{Nm}^2/\mathrm{C}^2$ is the Coulomb constant, and $q_e = 1.602\times10^{-19}\,\mathrm{C}$ is the electron charge [112]. The neutral-particle viscosity cross section is

$$\overline{Q}_{\mathrm{AA}}^{(2,2)} = 170\, T_h^{-1/4} \times \mathrm{\AA}^2$$

based on Liu et al. [113]. For charged particles,

$$\overline{Q}_{\mathrm{A^+A^+}}^{(2,2)} = 1.36 Q_c, \qquad \text{and} \qquad \overline{Q}_{ee}^{(2,2)} = 1.29 Q_c\,,$$

are based on Gupta et al. [109], where

$$Q_c = \frac{\epsilon^4}{(k_b T_e)^2} \ln\left[\frac{9(k_b T_e)^3}{4\pi\epsilon^6 n_e} + \frac{16(k_b T_e)^2}{\epsilon^4 n_e^{2/3}}\right]^{1/2}.$$

Rapid diffusion of free electrons, which would otherwise produce charge separation, is counteracted by a locally induced electric field, resulting in electrons and ions effectively diffusing in tandem [114]. This effect, termed ambipolar diffusion, suppresses free-electron diffusion and enhances ion diffusion and is modeled with expressions simplified for a three-component mixture [115]:

$$\boldsymbol{V}_e = \boldsymbol{V}_{\mathrm{A^+}} = \left[-\frac{1}{X_e}\frac{W_{\mathrm{A}}}{W} D_{\mathrm{amb}} + \frac{W_{\mathrm{A}}^2}{W^2}(D_{\mathrm{amb}} - D_{\mathrm{neut}})\right] \nabla X_e$$

$$\boldsymbol{V}_{\mathrm{A}} = \left[\frac{1}{X_{\mathrm{A}}}\frac{W_{\mathrm{A}}}{W} D_{\mathrm{neut}} + \frac{W_{\mathrm{A}}^2}{W^2}(D_{\mathrm{amb}} - D_{\mathrm{neut}})\right] \nabla X_e,$$

where

$$D_{\mathrm{amb}} = 2\mathcal{D}_{\mathrm{AA^+}}, \qquad D_{\mathrm{neut}} = 2\mathcal{D}_{\mathrm{AA^+}}\left(1 - \frac{\mathcal{D}_{\mathrm{AA^+}}}{D_{e\mathrm{A^+}}}\right)$$

and

$$D_{ij} = \mathcal{D}_{ij}\left[1 + \frac{n_k(\mathcal{D}_{ik} m_k/m_j - \mathcal{D}_{ij})}{n_i \mathcal{D}_{jk} + n_j \mathcal{D}_{ik} + n_k \mathcal{D}_{ij}}\right], \qquad i \neq j \neq k.$$

The expressions for D_{amb} and D_{neut} are derived with the approximations $D_{e\text{A}^+} = D_{e\text{A}}$ and $\mathcal{D}_{\text{AA}^+} = D_{\text{AA}^+} = D_{\text{A}^+\text{A}}$. The diffusion velocities include a correction term to ensure mass conservation ($\sum_k \rho Y_k \boldsymbol{V}_k = \boldsymbol{0}$) and also maintain charge neutrality ($n_{\text{A}^+}\boldsymbol{V}_{\text{A}^+} = n_e \boldsymbol{V}_e$).

The two collisional processes (5.1) and (5.2) respectively have rates of progress

$$\mathcal{R}_1 = k_{f,1}(T_e)\left(n_e n_{\text{A}} - \frac{1}{K(T_e)} n_e^2 n_{\text{A}^+}\right)$$

$$\mathcal{R}_2 = k_{f,2}(T_h)\left(n_{\text{A}}^2 - \frac{1}{K(T_h)} n_{\text{A}} n_e n_{\text{A}^+}\right)$$

where $K(T)$ is the Saha equilibrium constant [103, 116] approximated with the first term of the electronic partition function, corresponding to ground states, for A and A^+:

$$K(T) = 2\frac{g^0_{\text{A}^+}}{g^0_{\text{A}}}\left(\frac{2\pi m_e k_b T}{h^2}\right)^{3/2} \exp\left(-\frac{I_{\text{A}}}{k_b T}\right) \tag{5.12}$$

The rate constants $k_{f,1}$ and $k_{f,2}$ are based on Hoffert and Lien [102]:

$$k_{f,1} = 3.75 \times 10^{-16} T_e^{1.5}\left(\frac{\varepsilon_{\text{A}}}{k_b T_e} + 2\right)\exp\left(-\frac{\varepsilon_{\text{A}}}{k_b T_e}\right) \times \text{cm}^3/\text{s} \tag{5.13}$$

$$k_{f,2} = 1.68 \times 10^{-20} T_h^{1.5}\left(\frac{\varepsilon_{\text{A}}}{k_b T_h} + 2\right)\exp\left(-\frac{\varepsilon_{\text{A}}}{k_b T_h}\right) \times \text{cm}^3/\text{s} \tag{5.14}$$

The production rates are $\dot{n}_{\text{A}^+} = \dot{n}_e = -\dot{n}_{\text{A}} = \mathcal{R}_1 + \mathcal{R}_2$. Because derivation of (5.13) and (5.14) assumes that excitation of the neutral particle A is rate controlling and is expected to be valid only for $T \geq 3000\,\text{K}$ [102], $T = \max(T, 3000\,\text{K})$ is used as an approximation when computing (5.13) and (5.14); this is not expected to affect conclusions, as recombination occurs primarily in the hot core of the kernel by (5.1). The thermal relaxation time τ_{ek} for elastic collisions between free electrons and heavy species k is

$$\frac{1}{\tau_{ek}} = \frac{8}{3}\frac{m_e}{m_k} n_k v_e \overline{Q}^{(1,1)}_{ek} \tag{5.15}$$

where $v_e = \sqrt{8k_b T_e/\pi m_e}$ is the mean particle velocity of free electrons [8].

Because local thermodynamic equilibrium is believed to be establish inside the plasma kernel shortly after the laser pulse, based on electron number density and temperature measurements [117], the kernel is initialized with $T_h = T_e$. The initial electron spatial distribution is in equilibrium and prescribed using

$$\frac{\phi^2}{1-\phi} = \frac{m_{\mathrm{A}}}{\rho}\frac{2g^0_{\mathrm{A}^+}}{g^0_{\mathrm{A}}}\left(\frac{2\pi m_e k_b T_e}{h^2}\right)^{3/2}\exp\left(-\frac{I_{\mathrm{A}}}{k_b T_e}\right) \tag{5.16}$$

where $\phi = n_e/(n_{\mathrm{A}} + n_{\mathrm{A}^+}) = X_e/(1 - X_e)$ is the ionization degree [103]. The initial electron temperature is such that the internal energy distribution matches that described in section 2.1.

Comparisons of cross sections, thermodynamics properties, and transport coefficients with detailed calculations are included in appendix C. The present model also reproduces key features of a Mach 15.9 shock in argon, including its relaxation length and oscillatory character.

5.1.2 Two-species model

To isolate nonequilibrium-plasma effects, the argon plasma model is compared with a simple two-species model, in which both species are perfect gases and do not react chemically, with the species representing the plasma having half the molecular weight of the ambient fluid. This is necessary in order to initialize the kernel with the same peak temperature and pressure as the nonequilibrium model, which would not be possible with the perfect-gas model (section 3.1) due to differing molecular weights in the equation of state.

In addition to (3.8)–(3.10), the nondimensional governing equations include transport for two non-reacting species

$$\frac{\partial \hat{\rho} Y_k}{\partial \hat{t}} + \nabla\cdot(\hat{\rho} Y_k \hat{\boldsymbol{u}}) + \nabla\cdot(\hat{\rho} Y_k \hat{\boldsymbol{V}}_k) = 0\,, \qquad k \in \{\mathrm{A},\mathrm{I}\}\,,$$

and equation of state

$$\hat{p} = \frac{\gamma - 1}{\gamma}\frac{\hat{\rho}\hat{T}}{\hat{W}}\,,$$

where $\hat{W} = (Y_{\mathrm{A}}/\hat{W}_{\mathrm{A}} + Y_{\mathrm{I}}/\hat{W}_{\mathrm{I}})^{-1}$ is the mean molecular weight, and Y_{A} and Y_{I} are the mass fractions of the

neutral and ionized gas, respectively. The nondimensionalization matches (3.7), where ambient properties ρ_∞ and a_∞ are those of the neutral fluid, and molecular weights are nondimensionalized by W_A. The specific heat $c_{p,k} = \gamma\overline{R}/W_k(\gamma-1)$ is assumed constant, and $\gamma = 5/3$ and $\hat{W}_\mathrm{A} = 2\hat{W}_\mathrm{I} = 1$ are used for comparison with singly-ionized argon.

Both fluids are assumed to have the same transport properties, with viscosity modeled by a power law [118]:

$$\hat{\mu} = \frac{\mu}{\mu_\infty} = \left(\frac{T}{T_\infty}\right)^{0.7} = [(\gamma-1)\hat{T}]^{0.7}$$

Assuming constant Prandtl number $\mathrm{Pr} = c_{p,\mathrm{A}}\mu/\lambda$ and Lewis number $\mathrm{Le} = \lambda/\rho_\infty c_{p,\mathrm{A}} D$, where D is the diffusion coefficient, the stress tensor, heat flux, and diffusion velocity are respectively

$$\hat{\boldsymbol{\tau}} = \frac{\hat{\mu}}{\mathrm{Re}}\left[(\hat{\nabla}\hat{\boldsymbol{u}} + \hat{\nabla}\hat{\boldsymbol{u}}^T) - \frac{2}{3}(\hat{\nabla}\cdot\hat{\boldsymbol{u}})\boldsymbol{I}\right] + \hat{\mu}_B(\hat{\nabla}\cdot\hat{\boldsymbol{u}})\boldsymbol{I}, \qquad \hat{\boldsymbol{q}} = \frac{\hat{\mu}}{\mathrm{Re}\,\mathrm{Pr}}\hat{\nabla}\hat{T}, \qquad \hat{\boldsymbol{V}}_k = -\frac{\hat{\mu}}{\mathrm{Re}\,\mathrm{Pr}\,\mathrm{Le}}\frac{1}{Y_k}\hat{\nabla}Y_k\,.$$

As with the nonequilibrium-plasma model (section 5.1.1), physical bulk viscosity is taken to be zero, and the shock-capturing artificial viscosity (5.10) is nondimensionalized as $\hat{\mu}_B = \mu_B/\rho_\infty a_\infty L$. In all two-species simulations, $\mathrm{Pr} = 0.7$ and $\mathrm{Le} = 1$.

The initial distribution of X_I is based on (5.16) in nondimensional form,

$$\frac{\phi^2}{1-\phi} = \hat{B}\frac{\hat{T}^{3/2}}{\hat{\rho}}\exp\left[-\frac{\hat{I}}{(\gamma-1)\hat{T}}\right]$$

where

$$\hat{B} = \frac{2g^0_{\mathrm{A}^+}}{g^0_\mathrm{A}}\left(\frac{2\pi m_e k_b}{h^2}\right)^{3/2}\frac{W_\mathrm{A}}{\mathcal{N}\rho_\infty}(\gamma-1)^{3/2}T_\infty^{3/2}, \qquad \hat{I} = \frac{I_\mathrm{A}}{k_b T_\infty}\,,$$

$\hat{B} = 1.53$ and $\hat{I} = 614$ are used to match properties of argon. The distribution of X_I is determined from $X_\mathrm{I} = 2\phi/(1+\phi) = X_e + X_{\mathrm{A}^+}$.

5.2 Discretization details for plasma simulations

Artificial bulk viscosity (5.10) is used to stabilize the shock during the earlier stage of the kernel evolution ($t \lesssim 2\,\mu$s), and third- and fourth-order derivatives are computed with sixth-order accurate stencils. Verification is provided in appendix B.2. The eighth-order implicit filter (2.7) is also used during this stage and later replaced, for computational efficiency, by its explicit counterpart (2.6) once the shock is sufficiently weak.

The mole fraction of electrons in the ambient gas is set to $X_{e,\infty} = 10^{-8}$. This avoids spurious errors resulting from calculating the electron temperature T_e where both the electronic energy and electron concentration are very small. It furthermore relaxes the spatial resolution required to resolve the rapid decrease of electrons at the perimeter of the kernel, where errors of a similar nature occur during the kernel expansion. Insensitivity to this parameter choice is confirmed with one-dimensional simulations (appendix C.3).

The kernel is simulated first on a uniform mesh until the shock reaches the boundary, occuring at approximately $t = 1\,\mu$s, and the solution is subsequently interpolated using bicubic polynomial splines onto the uniform region of a stretched, coarser mesh (table 5.2).

	Type	Mesh spacing	Extents	Uniform region	Size
1	Uniform	$1.4\,\mu$m	$6.05\,\text{mm} \times 2.38\,\text{mm}$	$6.05\,\text{mm} \times 2.38\,\text{mm}$	4320×1700
2	Stretched	$1.6\,\mu$m	$18\,\text{mm} \times 9\,\text{mm}$	$8.4\,\text{mm} \times 4.2\,\text{mm}$	5760×2880

Table 5.2: Meshes used for plasma simulations.

The time step [119] used for plasma simulations is

$$\Delta t < \mathcal{C} \min \left\{ \min_{(x,r)} \left\{ \frac{2.827/k'_{\max}}{\frac{|u_x|+a}{\Delta x} + \frac{|u_r|+a}{\Delta r}} \right\}, \min_{(x,r)} \left\{ \frac{2.785/k''_{\max}}{\frac{\kappa}{\Delta x^2} + \frac{\kappa}{\Delta r^2}} \right\} \right\} \tag{5.17}$$

where 2.827 and 2.785 correspond to the intersection of the fourth-order Runge-Kutta stability region with the imaginary and real axes, respectively; $k'_{\max} = 1.731$ and $k''_{\max} = 6.502$ are the maximum modified wave numbers [75] corresponding to the stencils (2.4) and (2.5), respectively. The criterion (5.17) is such that $\mathcal{C} < 1$ would be stable for a one-dimensional, linear model system with only advection or diffusion. The coefficient κ is taken to be

$$\kappa = \max \left\{ \frac{\mu}{\rho}, \frac{\lambda_h}{\rho c_v^t}, \frac{\lambda_{el}}{\rho c_v^e} \right\} \tag{5.18}$$

While inviscid and viscous terms couple to contribute to the stability limit, taking extrema as in (5.18) and (5.17) was sufficient as a working criterion for numerical stability.

Diffusion of electronic energy ($\lambda_{el}\nabla^2 T_e$) imposes the greatest stability restriction on the explicit time-stepping scheme, in some cases requiring $\Delta t < 10^{-12}\,\mathrm{s}$ with the mesh resolutions in table 5.2. Given the long time scale on which the hydrodynamic ejection forms ($t \sim 10^{-5}\,\mathrm{s}$), we apply an explicit, three-point second-order filter to $\lambda_{el}\nabla^2 T_e$,

$$\hat{f}_j = \frac{1}{2} f_j + \frac{1}{4}(f_{j+1} + f_{j-1})\,, \tag{5.19}$$

when computing the electronic heat flux $\boldsymbol{q}_e$ to reduce its represented wave-number spectrum and therefore its time-step restriction. This intentionally aggressive filter is consecutively applied four times for each evaluation of $\lambda_{el}\nabla^2 T_e$, and the corresponding transfer function [75] is shown in figure 5.1. Insensitivity is confirmed with one-dimensional simulations by comparison with the corresponding result with no filter on $\lambda_{el}\nabla^2 T_e$ (appendix C.3). Simulations are typically stable for $\mathcal{C} \approx 10$ (5.17), corresponding to $\Delta t \approx 2 \times 10^{-11}\,\mathrm{s}$ for the case presented in section 5.3.

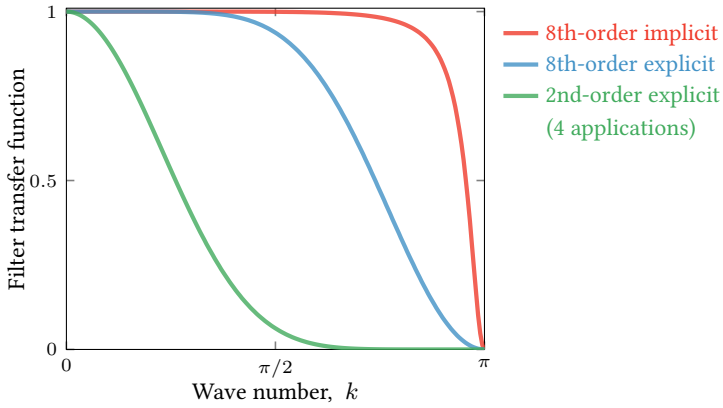

Figure 5.1: Filter transfer function for eighth-order explicit (2.6) and implicit (2.7) filters, and four applications of a second-order explicit filter (5.19).

5.3 Effect of recombination on the hydrodynamic expansion

The post-breakdown evolution for the nonequilibrium and two-species models is compare for an $L = 2\,\mathrm{mm}$, kernel with initial peak temperature $T_0 = 30\,000\,\mathrm{K}$ deposited in $p_\infty = 0.5\,\mathrm{atm}$, $T_\infty = 298\,\mathrm{K}$ argon, which correspond to $E = 48.5\,\mathrm{mJ}$ of deposited energy. The kernel geometry $\alpha = 2$, $\beta = 3$ has relatively pronounced asymmetry to accentuate the ejection. A Reynolds number $\mathrm{Re} = 2.36 \times 10^4$ corresponding to these conditions

is used for the two-species model, and results are dimensionalized accordingly for comparison. Both models are initialized with matching peak temperature and relative energy distribution; slight differences in T and X_I (figure 5.2a)—the latter corresponding to $X_e + X_{\mathrm{A}^+}$ for the nonequilibrium model—result from differing equations of state. Kernel properties are computed by integration over its volume: $\overline{T}_h$ and $\overline{T}_e$ are such that

$$\overline{\rho e}_h = \frac{3}{2}\left(\frac{\overline{\rho Y}_{\mathrm{A}}}{m_{\mathrm{A}}} + \frac{\overline{\rho Y}_{\mathrm{A}^+}}{m_{\mathrm{A}^+}}\right) k_b \overline{T}_h \qquad \text{and} \qquad \overline{\rho e}_{el} = \frac{3}{2}\frac{\overline{\rho Y}_e}{m_e} k_b \overline{T}_e + \sum_{k\in\{\mathrm{A},\mathrm{A}^+\}} \overline{\rho Y}_k \frac{g_k^1 \exp\left(-\frac{\varepsilon_k}{k_b \overline{T}_e}\right)}{g_k^0 + g_k^1 \exp\left(-\frac{\varepsilon_k}{k_b \overline{T}_e}\right)} \frac{\varepsilon_k}{m_k},$$

where

$$\overline{\rho Y}_k = \frac{1}{V}\int_{\mathcal{V}} \rho Y_k \,\mathrm{d}V', \qquad \overline{\rho e}_h = \frac{1}{V}\int_{\mathcal{V}} \rho e_h \,\mathrm{d}V', \qquad \overline{\rho e}_{el} = \frac{1}{V}\int_{\mathcal{V}} \rho e_{el} \,\mathrm{d}V',$$

and $\mathcal{V}$ is the region enclosed by the $\xi = 0$ surface (2.2) and V is its volume. The kernel density $\overline{\rho}$, pressure $\overline{p}$, and mole fraction $\overline{X}_k$ are similarly defined:

$$\overline{\rho} = \frac{1}{V}\int_{\mathcal{V}} \rho \,\mathrm{d}V', \qquad \overline{X}_k = \frac{1}{W_k}\frac{\overline{\rho Y}_k}{\overline{C}}, \qquad \text{and} \qquad \overline{p} = k_b\left(\frac{\overline{\rho Y}_e}{m_e}\overline{T}_e + \frac{\overline{\rho Y}_{\mathrm{A}^+}}{m_{\mathrm{A}^+}}\overline{T}_h + \frac{\overline{\rho Y}_{\mathrm{A}}}{m_{\mathrm{A}}}\overline{T}_h\right)$$

where $\overline{C} = (1/V)\int_{\mathcal{V}} C \,\mathrm{d}V'$ and C is the concentration.

The kernel temperature and density decrease (figures 5.3a–b) as it expands hydrodynamically. For $p_\infty = 0.5\,\mathrm{atm}$, elastic collisions between free electrons and ions are sufficiently frequent that $\overline{T}_e$ does not deviate significantly from $\overline{T}_h$. The kernel temperature for the nonequilibrium model decays more slowly than for the two-species model, apparent in figures 5.2(b) and (c), while the kernel expands to 2.8 times greater volume (figure 5.3b). This results primarily from heat released by electron recombination. The globally-integrated formation energy of ions $E_f = \int \rho e_f \,\mathrm{d}V'$ initially comprises 58% of total energy deposited (figure 5.3c); recombination converts a portion to the translational energy of free electrons, as well as that of heavy particles through elastic collisions, and elevates the kernel temperature and pressure (figure 5.3a and d). Thus recombination is a primary avenue by which formation energy of ions is converted to mechanical work on the gas. In the two-species model, $\overline{X}_{\mathrm{I}}$ decreases slowly due to diffusion through the kernel boundary (figure 5.3c). Corrugation of the kernel boundary (figure 5.2c) is due to vorticity generation at the smaller

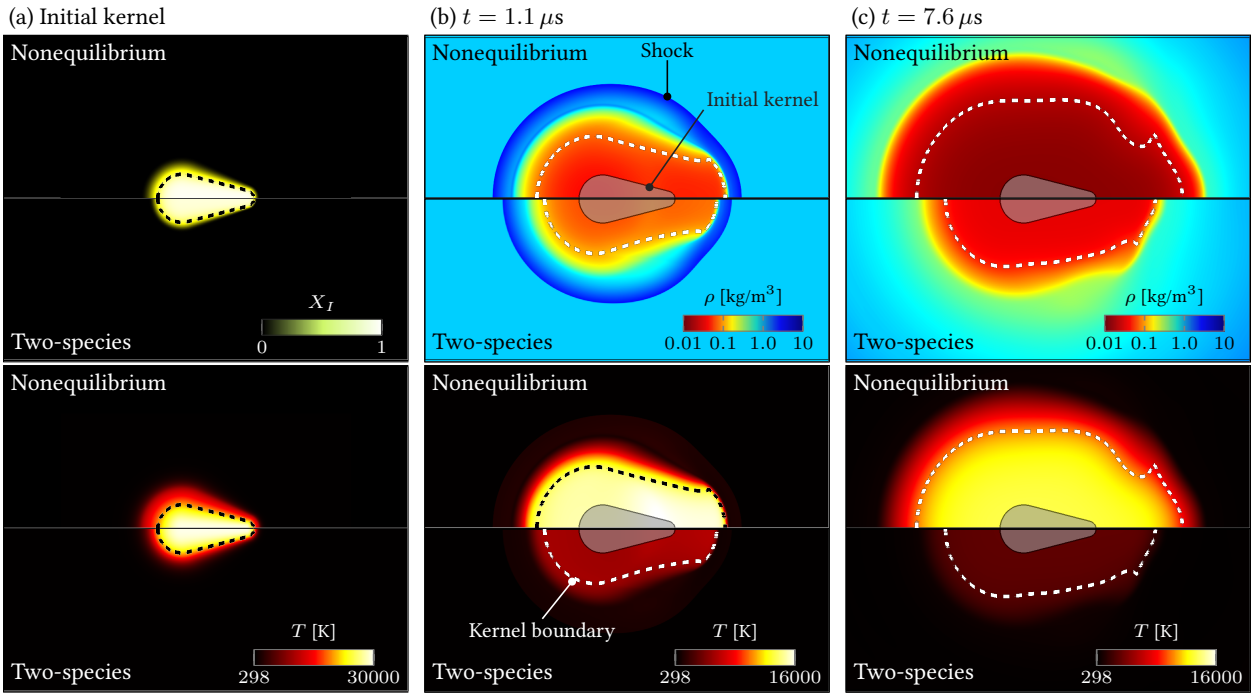

Figure 5.2: An $L = 2\,\text{mm}$, $E = 48.5\,\text{mJ}$ deposition in $p_\infty = 0.5\,\text{atm}$ argon at (a) its initial state, (b) $t = 1.1\,\mu\text{s}$, and (c) $t = 7.6\,\mu\text{s}$, computed using the nonequilibrium and two-species models. Dashed lines denote the kernel boundary, defined by $\xi = 0$ (2.2). Note the change in temperature scale.

R_2-end of the kernel.

The effect of recombination is quantified in figure 5.4 for a range of initial temperatures $T_0 \in [15\,000\,\text{K}, 61\,000\,\text{K}]$ for a spherically symmetric kernel with initial diameter $L = 1.16\,\text{mm}$ such that its volume matches that in figure 5.2(a). For each T_0, the kernel pressure at its maximum volume $V_{\max}$ is denoted by $\overline{p}_{V_{\max}}$, and $\overline{p}_0$ is its initial pressure. Dependence on the recombination rate is assessed by scaling the chemical source term $\dot{\omega}_k$ in (5.6) and (5.7) by a factor f_{rec}. For $f_{\text{rec}} = 1$, the kernel expands to a volume greater than that predicted by the two-species model. The effect is more pronounced for a larger pressure ratio $\overline{p}_0/\overline{p}_{V_{\max}}$, which corresponds to higher T_0 and thus higher initial level of ionization, but is suppressed at $p_\infty = 0.1\,\text{atm}$ due to the decreased collision rate at lower number densities. For $p_\infty = 1\,\text{atm}$, decreasing f_{rec} to zero results in an essentially adiabatic expansion from the initial kernel state to its maximum volume:

$$\frac{V_{\max}}{V_0} = \left(\frac{\overline{p}_0}{\overline{p}_{V_{\max}}}\right)^{1/\gamma}$$

where $\gamma = 5/3$, matching the behavior of the two-species model. At $p_\infty = 0.1\,\text{atm}$, however, both the two-species model and nonequilibrium model with $f_{\text{rec}} = 0$ depart slightly from adiabaticity (figure 5.4b) due to enhanced thermal diffusivity in lower-density gas.

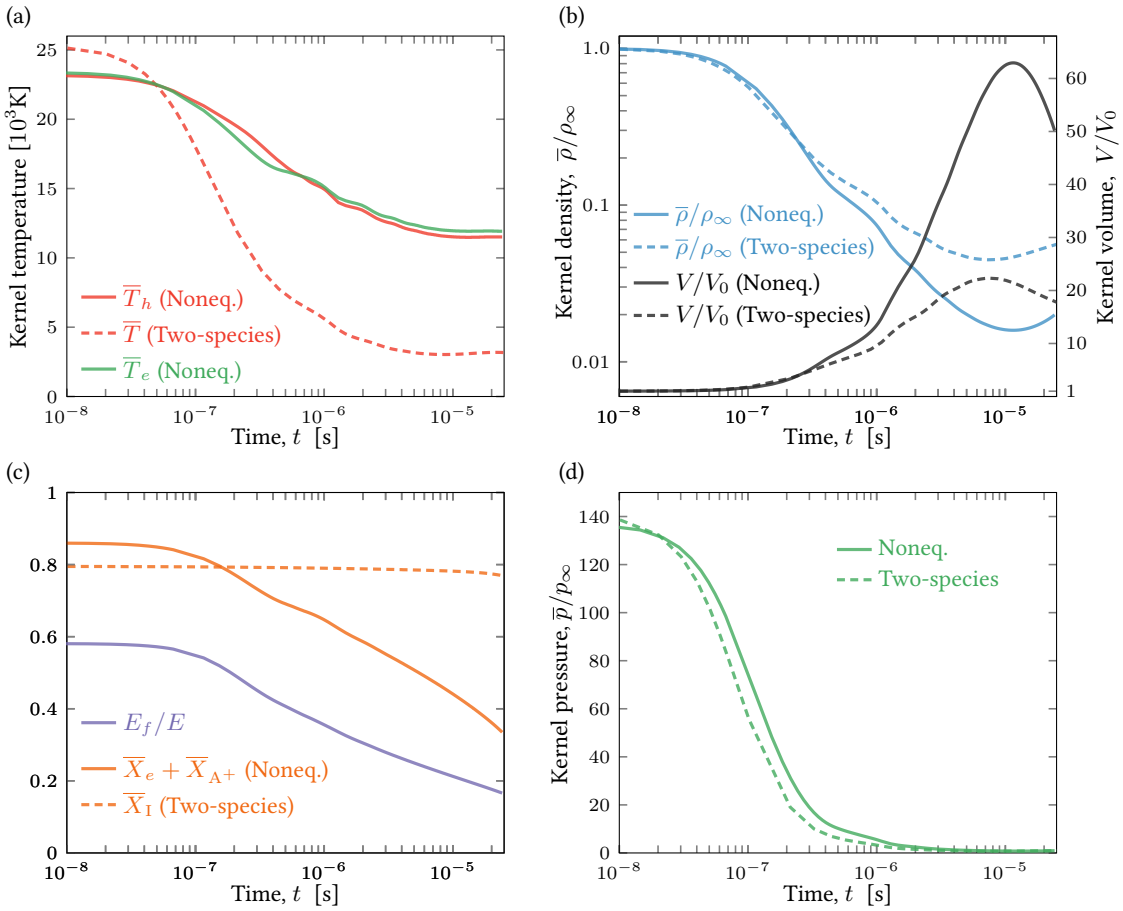

Figure 5.3: Time history of kernel properties for the evolution shown figure 5.2. V_0 is the initial volume of the kernel.

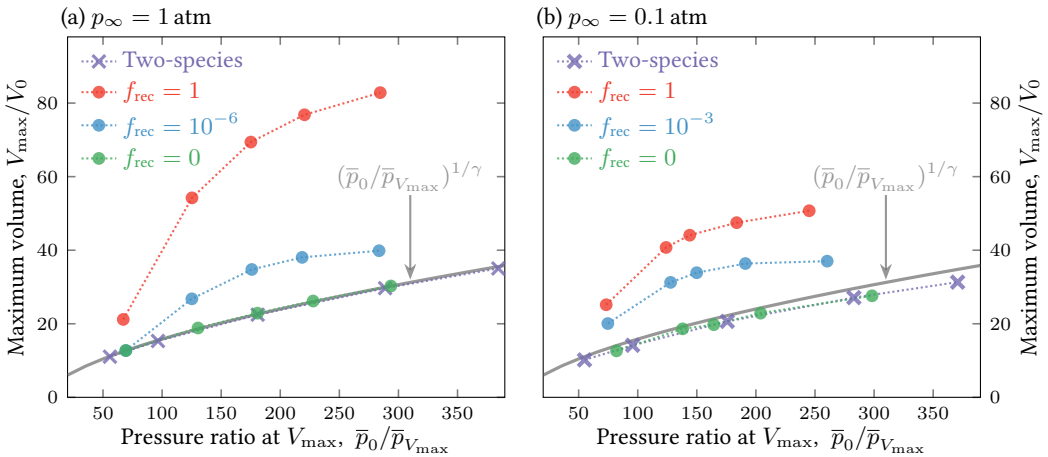

Figure 5.4: Maximum volume V_{max} attained by a spherically symmetric $L = 1.16$ mm kernel for (a) $p_\infty = 1$ atm and (b) $p_\infty = 0.1$ atm. The range of $\overline{p}_0/\overline{p}_{V_{max}}$ correspond to initial peak temperatures $T_0 \in [15\,000\,\text{K}, 61\,000\,\text{K}]$.

5.4 Effect on ejection

The plasma physics also appear to suppress the strength of the ejection. Figure 5.6(a–b) compares the flow at $t = 25.7\,\mu$s for the cases analyzed in section 5.3. Though the nonequilibrium model predicts more negative

circulation (figure 5.5), the vorticity is distributed over a larger volume compared to the two-species model, which remains closer to $r = 0$ (figure 5.6b). This is consistent with its faster flow and penetration into the hot core. Though the hottest region of the nonequilibrium-plasma kernel has low viscosity due to the presence of free electrons, the peak viscosity occurs near the region of high flow speed (figure 5.6a), which may further slow penetration.

The nonequilibrium result is compared to a second two-species case (figure 5.6c) in which the initial kernel temperature $T_0 = 155\,000\,\mathrm{K}$ is elevated so that the final kernel volume matches that predicted by the nonequilibrium model. The vorticity, as in the $T_0 = 30\,000\,\mathrm{K}$ case, is nonetheless concentrated near the centerline and penetrates more deeply into the kernel than the nonequilibrium case, suggesting that the enhanced expansion alone is insufficient to suppress the flow.

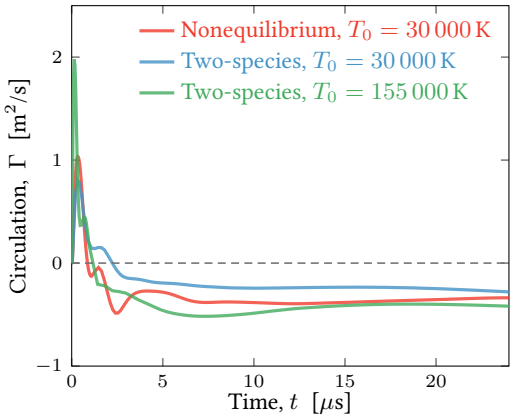

Figure 5.5: Circulation (3.14) evolution corresponding to the cases shown in figure 5.6.

(a) Nonequilibrium, $T_0 = 30\,000\,\mathrm{K}$

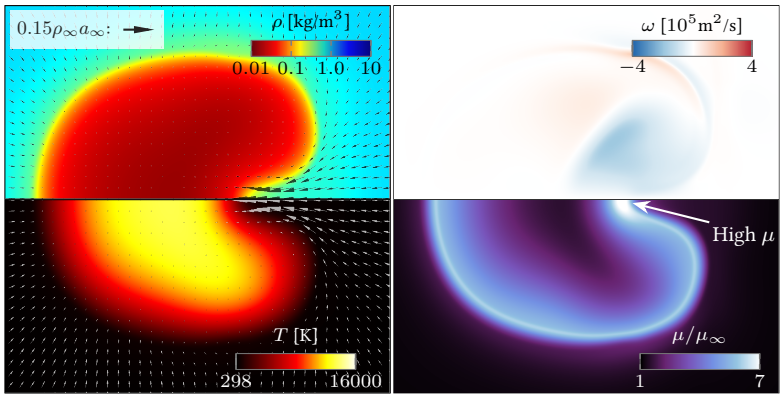

(b) Two-species, $T_0 = 30\,000\,\mathrm{K}$

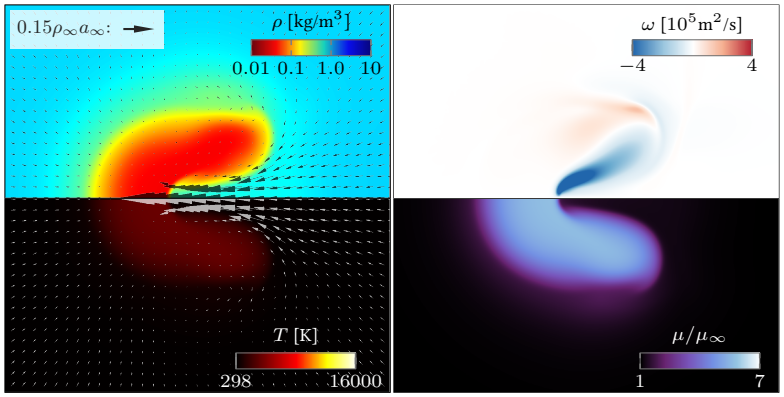

(c) Two-species, $T_0 = 155\,000\,\mathrm{K}$

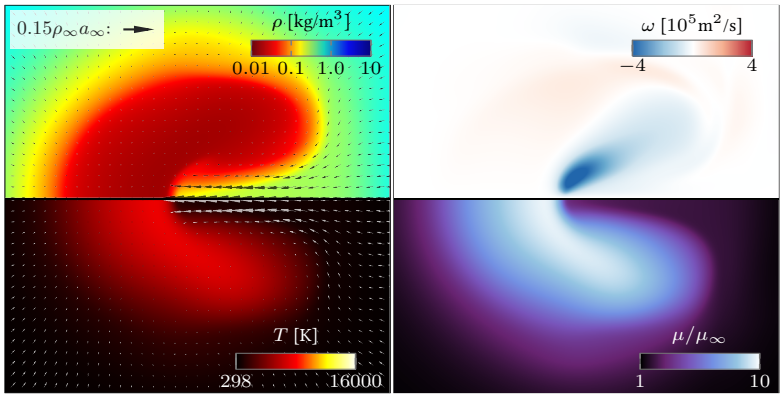

Figure 5.6: Flow at $t = 25.7\,\mu$s after $\beta = 3$, $\alpha = 2$ depositions in $p_\infty = 0.5\,$atm argon for the (a) nonequilibrium model with $T_0 = 30\,000\,$K, (b) two-species model with $T_0 = 30\,000\,$K, and (c) two-species model with $T_0 = 155\,000\,$K. Momentum vectors are shown due to the density variation and given in terms of its ambient value at sonic velocity. Note the differing scale for μ in (c).

Chapter 6

Ignition of a fuel–oxidizer interface

6.1 Configuration and combustion models

This configuration targets the intermediate complexity between existing studies of homogeneous mixtures [8, 20, 26] and combustor geometries [35, 37, 38, 120] and isolates the interaction of the expanding plasma kernel with a mixture gradient from other pre-pulse flow features. It consists of a length-L energy kernel is deposited in quiescent oxidizer with ambient pressure p_∞ and temperature T_∞ at a distance d from the $x = 0$ fuel interface (figure 6.1), defined by

$$\frac{\phi}{1+\phi} = \frac{1}{2} - \frac{1}{2}\tanh(\sigma x)\,, \tag{6.1}$$

where ϕ is the fuel-oxidizer equivalence ratio and σ is such that $\phi/(1+\phi) \in [0.1, 0.9]$ over a thickness h.

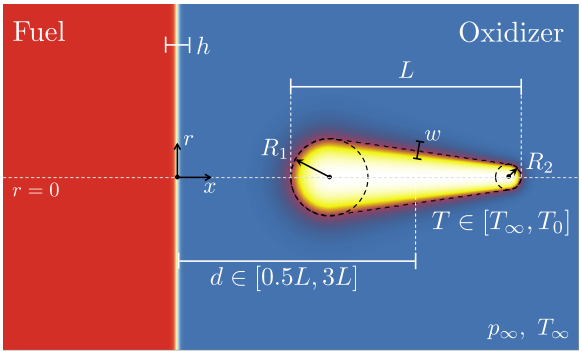

Figure 6.1: Schematic of the energy kernel deposited in oxidizer near a thin fuel interface.

The energy distribution of the kernel matches that described in section 2.1. Of the parameters shown in

figure 6.1, dependence on d and $\beta = R_1/R_2$ will be of primary concern. For all simulations in this chapter, the aspect ratio is fixed at $L/2R_1 = 3$.

6.1.1 Detailed combustion model

The detailed combustion model consists of the same equations for an ideal gas (3.1)–(3.4) in addition to the species mass equation

$$\frac{\partial \rho Y_k}{\partial t} + \nabla \cdot [\rho Y_k (\boldsymbol{u} + \boldsymbol{V}_k)] = W_k \omega_k \,, \tag{6.2}$$

where Y_k and W_k are the species mass fraction and molecular weights, respectively. The Wilke mixture rule (5.1.1) is used for the mixture viscosity, and the mixture thermal conductivity is approximated as [107]

$$\lambda = \frac{1}{2}\left(\sum_{k=1}^{N} X_k \lambda_k + \frac{1}{\sum\limits_{k=1}^{N} X_k/\lambda_k} \right) , \tag{6.3}$$

where X_k is the species mole fraction and temperature-dependent species properties μ_k and λ_k are computed according to the Lennard-Jones intermolecular energy potential [121]. Physical bulk viscosity in the stress tensor (3.5) is neglected for this model, and the shock-capturing artificial-viscosity model (5.10) is used here $C = 1.75$ [106]. The stress tensor matches (3.5), while the heat flux for multicomponent flow contains an additional contribution due to differences in energy carried by diffusing species,

$$\boldsymbol{q} = \lambda \nabla T - \rho \sum_{k=1}^{N} Y_k h_k \boldsymbol{V}_k \tag{6.4}$$

where $h_k(T) = h_k^o + \int_{T^o}^{T} c_{p,k}(T')\,\mathrm{d}T'$ is the species enthalpy, h_k^o is the species enthalpy of formation, and $c_{p,k}$ is the specific heat at constant pressure. The diffusion velocity includes a standard correction to ensure mass conservation [122],

$$\boldsymbol{V}_k = -\frac{D_k}{X_k}\nabla X_k + \sum_{k=1}^{N} D_k \frac{W_k}{W} \nabla X_k \,, \tag{6.5}$$

and D_k are the mixture-averaged diffusion coefficients according to the Hirschfelder-Curtiss approximation [121],

$$D_k = \frac{1 - Y_k}{\sum_{j \neq k} X_j / \mathcal{D}_{jk}} \tag{6.6}$$

where $\mathcal{D}_{jk}$ is the binary diffusion coefficient. To support simulation of the high-temperature kernel, thermodynamic properties are fitted to the model of Munafò et al. [8] over $T \in [250\,\mathrm{K}, 100\,000\,\mathrm{K}]$ using nine-coefficient NASA thermodynamics polynomials [123]. The chemical source term ω_k is modeled using a 9-species, 21-step kinetics mechanism for hydrogen combustion [98]. The Cantera software package [124] is used to compute thermodynamic and transport properties as well as the chemical source terms.

For this model an initial chemical transient occurs rapidly ($t \lesssim 1\,\mathrm{ns}$) as an artifact of this simplified breakdown, during which the high-temperature core dissociates almost entirely into atomic oxygen, cooling rapidly at approximately constant ρ and e and reaching effective chemical equilibrium before any meaningful flow develops. This transient is explicitly resolved as a modeling choice, rather than initiating a chemically equilibrated energy distribution, because cooler gas along the kernel's perimeter dissociates at a rate comparable to that of the subsequent hydrodynamic expansion. Conclusions are not anticipated to be sensitive to this choice. T_{LIB} will be used throughout to denote the peak temperature of the dissociated kernel.

6.1.2 Reduced combustion model

The simplified combustion model consists of a global irreversible reaction and a reversible recombination reaction:

$$\mathrm{F} + \nu_{\mathrm{O}}\,\mathrm{O} \longrightarrow \nu_{\mathrm{P}}\,\mathrm{P} \tag{6.7}$$

$$\mathrm{R} + \mathrm{R} + \mathrm{M} \longleftrightarrow \mathrm{O} + \mathrm{M} \tag{6.8}$$

where the fuel, oxidizer, radical, and product are denoted by F, O, R, and P respectively. While the radical does not participate directly in the combustion reaction, its thermodynamic effect on ignition is discussed in section 6.5.1. The governing equations take the same form as (3.1)–(6.2), in nondimensional terms, and includes the equation of state

$$\hat{p} = \frac{\gamma - 1}{\gamma} \frac{\hat{\rho}\hat{T}}{\hat{W}}$$

They are nondimensionalized by the kernel length L and ambient density $\rho_{O,\infty}$ and speed of sound $a_{O,\infty}$ of the oxidizer:

$$\hat{t} = \frac{t a_{O,\infty}}{L}, \qquad \hat{\boldsymbol{x}} = \frac{\boldsymbol{x}}{L}, \qquad \hat{\rho} = \frac{\rho}{\rho_{O,\infty}}, \qquad \hat{\boldsymbol{u}} = \frac{\boldsymbol{u}}{a_{O,\infty}}, \qquad \hat{p} = \frac{p}{\gamma p_\infty}, \qquad \hat{T} = \frac{T}{(\gamma - 1)T_\infty}, \qquad \hat{e} = \frac{e}{a_{O,\infty}^2}.$$

This yields Reynolds, Prandtl, and Lewis numbers

$$\mathrm{Re} = \frac{\rho_{O,\infty} a_{O,\infty} L}{\mu_\infty}, \qquad \mathrm{Pr} = \frac{c_{p,O}\mu}{\lambda}, \qquad \mathrm{Le} = \frac{\lambda}{\rho_{O,\infty} c_{p,O} D} = \frac{\lambda}{\rho_{F,\infty} c_{p,F} D},$$

and nondimensional stress tensor, heat flux, and diffusion velocity

$$\hat{\boldsymbol{\tau}} = \frac{\hat{\mu}}{\mathrm{Re}} \left[(\hat{\nabla}\hat{\boldsymbol{u}} + \hat{\nabla}\hat{\boldsymbol{u}}^T) - \frac{2}{3}(\hat{\nabla} \cdot \hat{\boldsymbol{u}})\boldsymbol{I} \right] + \hat{\mu}_B (\hat{\nabla} \cdot \hat{\boldsymbol{u}})\boldsymbol{I}, \qquad \hat{\boldsymbol{q}} = \frac{\hat{\mu}}{\mathrm{Re}\,\mathrm{Pr}} \hat{\nabla}\hat{T} - \hat{\rho} \sum_{k=1}^{N} Y_k \hat{h}_k \hat{\boldsymbol{V}}_k,$$

$$\hat{\boldsymbol{V}}_k = -\frac{\hat{\mu}}{\mathrm{Re}\,\mathrm{Pr}\,\mathrm{Le}} \left[\frac{1}{X_k} \hat{\nabla} X_k + \sum_{k=1}^{N} \frac{\hat{W}_k}{\hat{W}} \hat{\nabla} X_k \right].$$

A power-law model is used for viscosity [118],

$$\hat{\mu} = \frac{\mu}{\mu_\infty} = \left[(\gamma - 1)\hat{T} \right]^{0.7},$$

and the thermal conductivity λ and diffusion coefficient D are computed assuming constant Pr and Le, with $\mathrm{Pr} = 0.7$ throughout except in section 6.5.1. Though the power-law model overpredicts viscosity for the initial high temperatures in the kernel, most of the flow occurs after the kernel cools below $T < 4000\,\mathrm{K}$, where the model's accuracy is consistent with the present level of approximation. The artificial bulk viscosity is nondimensionalized as $\hat{\mu}_B = \mu_B / \rho_{O,\infty} a_{O,\infty} L$.

Assuming constant specific heat $c_{p,k} = \gamma_k \overline{R}/(\gamma_k - 1)W_k$, the internal energy is

$$\hat{e} = \frac{1}{\gamma}\sum_{k=1}^{N}\frac{\gamma-1}{\gamma_k-1}\frac{Y_k}{\hat{W}_k}\left(\hat{T}-\frac{1}{\gamma-1}\right)+\frac{1}{\gamma}\left(Y_P\frac{\hat{h}_P^o}{\hat{W}_P}+Y_R\frac{\hat{h}_R^o}{\hat{W}_R}-\frac{1}{\hat{W}}\right),$$

where we take $\gamma_k = \gamma = 1.4$ for all species except the radical, for which $\gamma_R = 5/3$. The enthalpy of formation $\hat{h}_k^o = h_k^o W_k/\overline{R}T_\infty$ at T_∞ is taken to be zero for the fuel and oxidizer. For the radical species, $\hat{h}_R^o = 101$ matches that of atomic oxygen [125]. For the product, $\hat{h}_P^o$ is based on an approximation of the adiabatic flame temperature T_f for a $\gamma = 1.4$ gas at isobaric, stoichiometric conditions,

$$\frac{h_P^o W_P}{\overline{R}T_\infty} = -\frac{\gamma}{\gamma-1}\left(\frac{T_f}{T_\infty}-1\right).$$

Molecular weights are nondimensionalized by W_O, so

$$\hat{W}_F = \frac{1-\mathrm{At}}{1+\mathrm{At}} = \frac{s}{s+1}\nu_P\hat{W}_P \qquad \text{and} \qquad \hat{W}_R = \frac{1}{2}, \tag{6.9}$$

where the stoichiometric ratio $s = W_F/\nu_O W_O$ is a model parameter, and the Atwood number is

$$\mathrm{At} = \frac{W_O - W_F}{W_O + W_F}$$

The density ratio for a stoichiometric mixture is

$$\frac{\rho_u}{\rho_b} = \frac{1}{\hat{W}_P}\frac{1+s}{1+s/\hat{W}_F}\frac{T_f}{T_\infty} \tag{6.10}$$

where ρ_u and ρ_b are the density of the unburnt and burnt mixtures, respectively. Both ν_P and $\hat{W}_P$ are treated as model parameters. The reaction rates are

$$\hat{\mathcal{R}}_1 = \mathrm{Da}_1 \exp\left[-\frac{\hat{T}_a}{(\gamma-1)\hat{T}}\right]\rho^2\frac{Y_F}{\hat{W}_F}\frac{Y_O}{\hat{W}_O} \tag{6.11}$$

$$\hat{\mathcal{R}}_2 = \mathrm{Da}_2 \hat{T}^{-1/2} \left(\hat{\rho}^2 \frac{Y_R^2}{\hat{W}_R^2} - \frac{1}{\hat{K}} \hat{\rho} \frac{Y_O}{\hat{W}_O} \right) \hat{\rho} \sum_{k=1}^{n} \frac{Y_k}{\hat{W}_k} \tag{6.12}$$

with Damköhler numbers

$$\mathrm{Da}_1 = \frac{A_1 C_\infty L}{a_{O,\infty}} \qquad \text{and} \qquad \mathrm{Da}_2 = \frac{A_2 C_\infty^2 L}{a_{O,\infty}} \left[(\gamma - 1) T_\infty \right]^{-1/2},$$

where A_j corresponds to the Arrhenius pre-exponential factor and $C_\infty = p_\infty / \overline{R} T_\infty$. Da_1 varies among cases, while $\mathrm{Da}_2 = 5.80$ is fixed based on $A_2 = 6.17 \times 10^{15}\,\mathrm{cm^6 mol^{-2} s^{-1} K^{1/2}}$ [98]. The activation temperature of the first reaction is $\hat{T}_a = E_a / \overline{R} T_\infty$ and E_a is its activation energy, while the recombination reaction (6.8) has zero activation energy. The equilibrium constant

$$\hat{K} = K_C C_\infty = \hat{B} \hat{T} \exp\left[-\frac{\hat{G}}{(\gamma - 1)\hat{T}} \right]$$

is derived from $K_C = \overline{R} T \exp(-\Delta G^o / \overline{R} T) / p^o$ with a linear approximation for the change in Gibbs free energy $\Delta G^o = -2 g_O^o + b(T - T_\infty)$, where $g_O^o = 2.32 \times 10^5\,\mathrm{J/mol}$ is the free energy of formation of atomic oxygen at 298 K [126], and $b = 142\,\mathrm{J/(mol \cdot K)}$ is approximated from the detailed model. The nondimensional parameters

$$\hat{B} = (\gamma - 1) \frac{C_\infty \overline{R} T_\infty}{p^o} \exp\left[-\frac{b}{\overline{R}} \right] \qquad \text{and} \qquad \hat{G} = -\frac{2 g_O^o + b T_\infty}{\overline{R} T_\infty}$$

are fixed at $\hat{B} = 1.95 \times 10^{-8}$ and $\hat{G} = -204$, which produce agreement with the detailed-model equilibrium O_2–O composition to within 4% over $T \in [298\,\mathrm{K},\ 15\,000\,\mathrm{K}]$.

6.2 Discretization details for combustion simulations

The shock is stabilized with artificial viscosity and an implicit eighth-order filter as described in section 5.2. Characteristic boundary conditions are modified for reacting flow [127]. The mesh spacing is at most $\Delta x_{\min} = \Delta r_{\min} = 8\delta_f$, where δ_f is the premixed laminar flame thickness

$$\delta_f = \frac{T_f - T_\infty}{\max\{|\partial T/\partial x|\}}$$

computed from one-dimensional simulations at corresponding conditions; δ_f depends on At and Da_1. For deposition cases with $d \leq 0.7L$, a finer uniform mesh with $\Delta x = 10^{-3}L$ is used to resolve the shock–interface interaction, most pronounced for $t \leq 0.5L/a_{O,\infty}$, after which the solution is interpolated using bicubic splines onto a coarser, stretched mesh with $\Delta x_{\min} = 3 \times 10^{-3}L$ for the subsequent ignition and flame development. For depositions at $d > L$, $\Delta x_{\min} = 3 \times 10^{-3}L$ is used. Table 6.1 summarizes the meshes used.

Use	Type	Mesh spacing	Extents	Uniform region	Size
$d \leq 0.7L$, $t < 0.5L/a_{O,\infty}$	Uniform	$10^{-3}L$	$4.32L \times 2.0L$	$4.32L \times 2.0L$	4320×2000
$d \leq L$	Stretched	$3 \times 10^{-3}L$	$36L \times 12L$	$14.6L \times 4.4L$	5400×1700
$d > L$	Stretched	$3 \times 10^{-3}L$	$24L \times 12L$	$11.4L \times 3.0L$	4320×1200
Detailed model	Stretched	$6\,\mu$m	$40\,\mathrm{mm} \times 12\,\mathrm{mm}$	$18.3\,\mathrm{mm} \times 6.1\,\mathrm{mm}$	3600×1240

Table 6.1: Meshes used for combustion simulations.

For the detailed H_2–O_2 combustion model, the time step during the early stage is limited by the high-temperature chemistry and is increased incrementally from 2 ps to 200 ps; $\Delta t = 0.8$ ns is used during the subsequent combustion. For the reduced model, the time step is set by (5.17) with $\mathcal{C} = 0.9$ and

$$\kappa = \max\left\{\frac{\hat{\mu}}{\hat{\rho}\,\mathrm{Re}}, \frac{\hat{\mu}\gamma\hat{W}}{\hat{\rho}\,\mathrm{Re}\,\mathrm{Pr}}\right\}.$$

6.3 Comparison with experiment

The geometric breakdown model is used in conjunction with the detailed H_2–O_2 combustion model for comparison with flame growth measurements (figure 6.2) at two homogeneous-mixture conditions: (1) $p_\infty = 100\,\mathrm{kPa}$, $\phi = 0.5$, and (2) $p_\infty = 70\,\mathrm{kPa}$, $\phi = 1.0$ where ϕ is the fuel–oxidizer equivalence ratio. The energy kernel is initialized with $L = 2.1\,\mathrm{mm}$, $\alpha = 5.6$, $\beta = 1.0$, corresponding to the 32 ns post-breakdown state for the 70 kPa case, and $L = 2.0\,\mathrm{mm}$, $\alpha = 5.0$ and $\beta = 1.1$, corresponding to the 80 ns state for the 100 kPa case, both from auxiliary simulations of a detailed nonequilibrium-plasma model [8]. The total deposited energy $E = 6.8\,\mathrm{mJ}$ at 70 kPa and $E = 12\,\mathrm{mJ}$ at 100kPa is controlled by adjusting the initial kernel temperature T_0. In figure 6.2(a), discrepancy in the flame radius due to the confining effect of the experimental chamber can be expected after $t \gtrsim 96\,\mu$s and $t \gtrsim 113\,\mu$s at 70 kPa and 100 kPa respectively, which correspond to the time for an acoustic wave to travel from the breakdown to the nearest wall and back. While this axisymmetric

model is clearly not expected to predict three-dimensional flame-surface instabilities and their effect on flame growth [128, 129], it nonetheless reproduces corrugations, more pronounced at 100 kPa, seen in figures 6.2(b) and (c). Importantly, there is agreement at 5 μs, shown in the inset, when the kernel dimensions are expected to be most sensitive to details of the deposition.

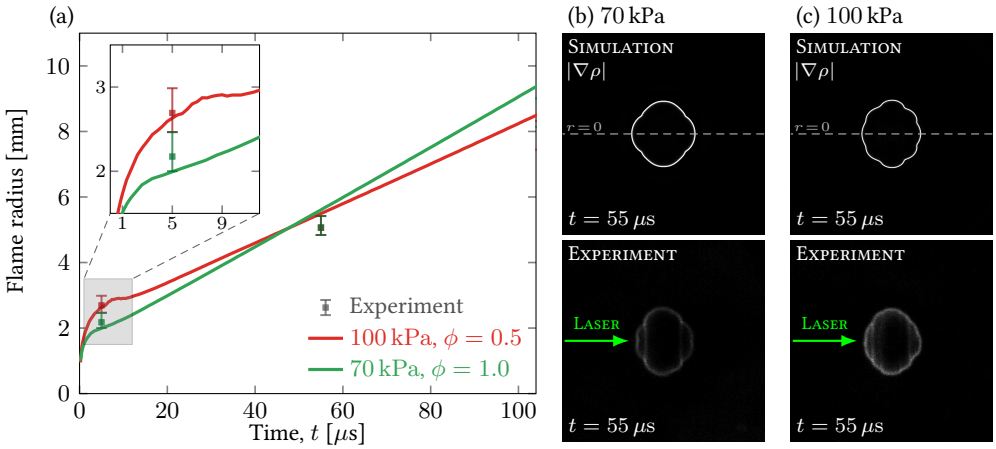

Figure 6.2: (a) Simulated and experimentally measured flame radius in hydrogen (M. Nishihara and G. S. Elliott, personal communication), taken to be the average of the axial and radial extents; error bars denote extrema among 3 trials at 70 kPa and 6 trials at 100 kPa. Computed $|\nabla\rho| \in [0, 5000]\,\mathrm{kg/m^4}$ and Schlieren imaging are shown for (b) 70 kPa and (c) 100 kPa. Each image is 35 mm $\times$ 35 mm, and the $r = 0$ symmetry axis is marked for simulations.

6.4 Ignition Phenomenology

The detailed H_2–O_2 combustion model (section 6.1.1) is used to demonstrate the effect of breakdown-induced hydrodynamics on the ignition character. The kernel has initial length $L = 2\,\mathrm{mm}$ and temperature $T_0 = 15\,500\,\mathrm{K}$, and its geometry $\beta \in [1, 3]$ is varied by changing R_2 at fixed $R_1 = L/6$. Because the initial kernel volume depends on β, this corresponds to total energy deposited $E = \int \rho_\infty (e - e_\infty)\,\mathrm{d}V \in [17.6\,\mathrm{mJ}, 31.2\,\mathrm{mJ}]$. The ambient conditions are $p_\infty = 1\,\mathrm{atm}$ and $T = 298\,\mathrm{K}$, and the initial interface thickness is $h = L/20$.

Ignition depends on kernel asymmetry β and its distance d from the fuel interface. For asymmetric kernels ($\beta > 1$) that are sufficiently far ($d \geq 1.5L$) from the interface, hot gas is ejected towards the fuel. The ejection ignites if it makes contact with the fuel at a sufficiently high temperature (figure 6.3b), but for a more distal deposition, this fails to occur due to the increased time to cool before reaching the fuel (figure 6.3a). More symmetric kernels, such as $\beta = 1.5$ in figure 6.3(c), produce ejections that are slightly larger radially (figure 6.3c), due to the larger initial R_2 (section 3.4.5), but have correspondingly slower vortex-ring auto-advection speeds and reach the fuel after cooling significantly. Ignition is therefore favored for smaller d and larger β.

At $d = L$, however, the expanding kernel interacts with the fuel interface, resulting in a peculiar reversal

of the ejection, which instead propagates *away* from the fuel. As seen in figure 6.3(d), ignition occurs by slowly-advecting remnants of the hot kernel rather than the ejection. This reversal is observed for $\beta \in [1, 2]$ and notably results in a prolonged delay of ignition and even no ignition, despite the proximity of the energy deposition. Cases from figure 6.3 are discussed in detail in sections 6.5 and 6.6.

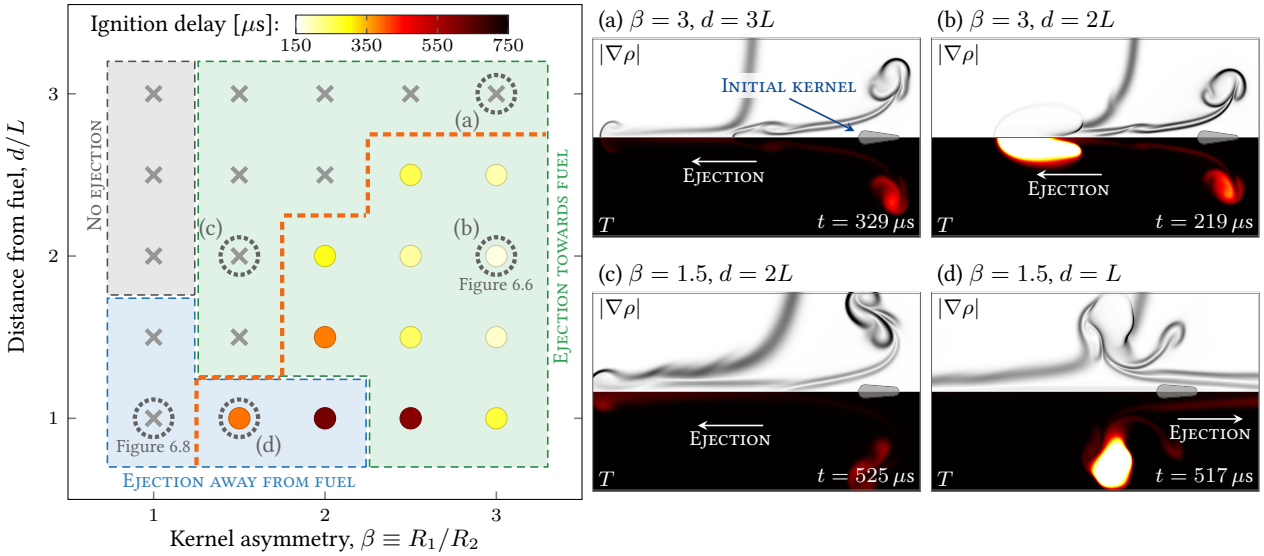

Figure 6.3: Dependence of ignition delay time on β and d for the H_2–O_2 detailed combustion model; non-igniting cases are marked by an "×". Ignition is defined by the inflection point of the otherwise monotonically decreasing global maximum T. Temperature and $|\nabla\rho|$ are shown for four cases in (a–d). Cases corresponding to figures 6.6 and 6.8 are also indicated for reference.

6.4.1 Reduced-model validation

To validate the reduced model, we compare its ignition phenomenology with that of the detailed model (figure 6.3). The kernel is initialized at $T_0 = 18\,774\,\mathrm{K} = 63T_\infty$ so that the total energy deposited matches that of the detailed simulation, though it results in a higher temperature than $T_0 = 15\,500\,\mathrm{K}$ used for the detailed model due to differing thermodynamic models. The dissociation reaction (6.8) is initialized in equilibrium, so $Y_R \approx 1.0$ in the hottest regions of the kernel. A global Lewis number $\mathrm{Le} = 0.3$ is used to model diffusion with hydrogen [130], and $\mathrm{Re} = 4.3 \times 10^4$ and $\mathrm{Pr} = 0.7$ correspond to oxygen at the ambient conditions with $L = 2\,\mathrm{mm}$. It was found that calibrating Da_1 by matching the isobaric autoignition time of the detailed model in a $\phi = 0.1$ mixture at 900 K with atomic oxygen $Y_O = 10^{-2}$, corresponding to conditions inside the ejection, did not reproduce the expected ejection-ignition behavior. Instead $\mathrm{Da}_1 = 1.35 \times 10^5$, 1.5 times larger than the calibrated value, is used. The activation temperature $\hat{T}_a = 35$ is higher than values typically reported for hydrogen based on premixed flame speed (e.g. $\hat{T}_a \in [11, 26]$ [131]) and, for this nonpremixed configuration, was found to be necessary to reproduce ignition sensitivity to the ejection temperature. The parameters $\mathrm{At} = 0.882$, $s = 0.125$, $\nu_P = 1$ are used for this comparison, and the molecular

weight $\hat{W}_P = 0.5625$ matches that of water.

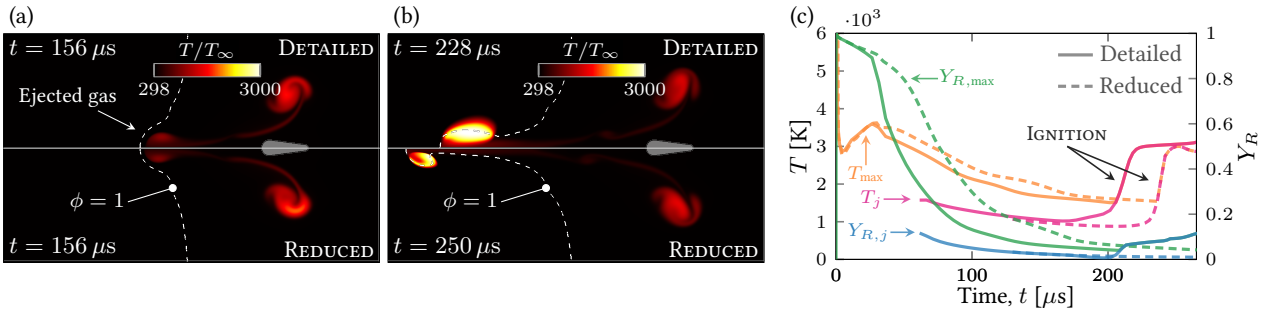

Figure 6.4: (a–b) Ignition with $\beta = 2.5$, $d = 2L$, and (c) time histories of T and radical mass fraction Y_R (corresponding to Y_O for the detailed model). Subscripts "max" and "j" indicate global maxima and properties of the ejected gas, respectively. The stoichiometric surface is marked in (a) and (b).

Figure 6.4 compares ignition by the ejected gas for detailed and reduced models with $\beta = 3$, $d = 2L$. Both produce an ejection at $t \approx 61\,\mu$s, which reaches the fuel at $t = 156\,\mu$s with essentially matching temperature distributions (figure 6.4a). Though ignition occurs later in the reduced model, which leads to deeper penetration into the fuel (figure 6.4b), there is agreement in the temperature T_j and radical mass fraction $Y_{R,j}$ of the ejected gas, the latter corresponding to atomic oxygen Y_O for the detailed model.

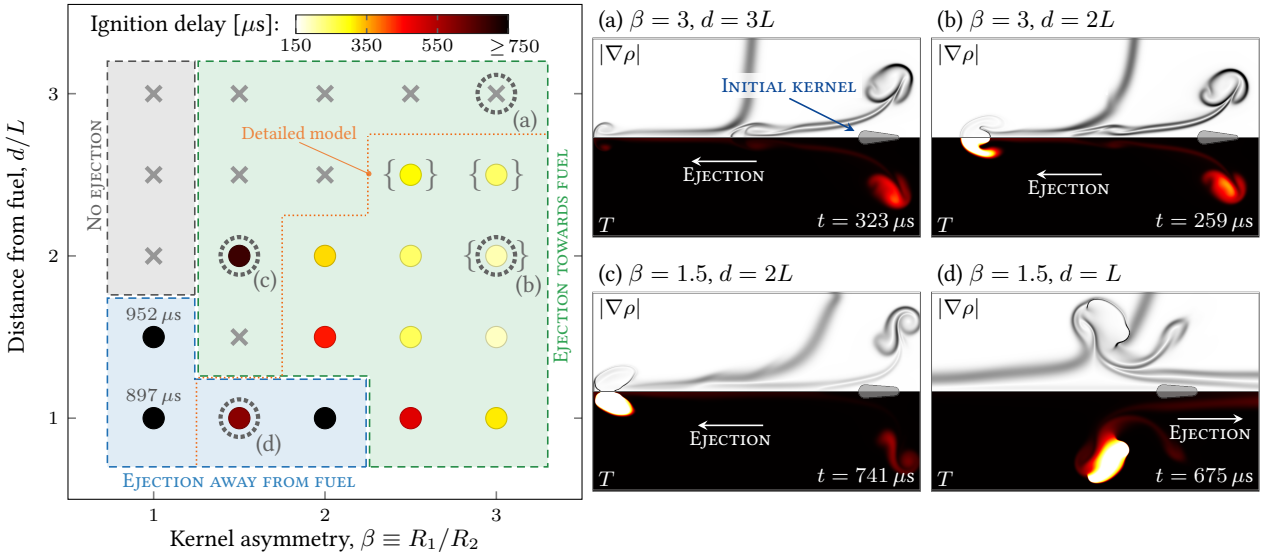

Figure 6.5: Dependence of ignition delay time on β and d for the reduced model, annotated as in figure 6.3 and with matching color scale to facilitate comparison; longer ignition times are marked. Braces indicate extinction after ignition. The ignition boundary for the detailed model is shown for reference. Temperature and $|\nabla\rho|$ are shown for representative cases in (a–d).

The ignition phenomenology over $\beta \in [1, 3]$, $d \in [L, 3L]$ is shown in figure 6.5. Point-to-point agreement is obviously not expected given the intended simplicity of this reduced model. Still, it reproduces key features of the detailed-model phenomenology. For both models, the earliest ignition occurs at $\beta = 3$, $d = 2L$, with ignition delay increasing as d approaches L. With the exception of one case (figure 6.5c), the ignition

boundary is reproduced by the reduced model when the ejection propagates towards the fuel. Even in reverse-ejection $d = L$ cases where the flow is disrupted by interaction with the interface (e.g. figure 6.5d), the reduced model predicts the resulting delayed ignition. In the three igniting cases that fall outside the detailed-model ignition boundary, the reduced model produces ignition at low temperatures $T < 900\text{K}$ where discrepancy can be anticipated, and near the upper boundary the three cases in which the diffusion flame extinguishes after ignition are likely a result of the richer mixture encountered by the ejection due to its deeper penetration at ignition (e.g. figure 6.4b). Such discrepancies are expected given the sensitivity of ignition to temperature and radical content as well as the qualitative differences across this parameter space in how the flow distributes heated gas. A more detailed calibration of Da_1 and $\hat{T}_a$, and potentially other model parameters, would likely produce closer agreement for this particular comparison with hydrogen but is unnecessary given our present objective. This model is exercised in sections 6.5 and 6.6 to analyze mechanisms by which ignition is qualitatively altered by breakdown-induced flow for a range of fuel properties.

6.5 Ignition by ejected hot gas

A representative igniting case with $\beta = 3$, $d = 2L$, and $E = 17.6\,\text{mJ}$ is shown in figure 6.6 using the detailed H_2–O_2 model. The kernel expands and cools rapidly after deposition, producing a shock (figure 6.6a) that generates a reflected rarefaction wave upon interacting with the interface due to the lower density of hydrogen. For this asymmetric $\beta = 3$ kernel, pronounced negative vorticity $\omega = \partial u_r/\partial x - \partial u_x/\partial r$ is generated by baroclinic torque at the smaller R_2-end of the kernel, which penetrates into the hot, low-density core (figure 6.6b) as it auto-advects towards the fuel. This ejects from the kernel at $t = 52\,\mu\text{s}$ as a radical-rich vortex ring (figure 6.6c), with peak local $|\boldsymbol{u}| = 65\,\text{m/s}$, and triggers OH production and ignition upon contact with H_2 (figure 6.6d). An edge flame forms and travels outward from the fuel cavity, outpacing the leftward ejection-induced motion of the interface.

6.5.1 Effect of radical recombination

At $T_0 = 15\,500\,\text{K}$, approximately 57% of the total energy deposited consists of formation energy of dissociated oxygen in all detailed-model simulations. This is consistent with the plasma model of MacArt et al. [129], based on Munafò et al. [8], which includes 10 charged species (H_2^+, O_2^+, H^+, O^+, O^{2+}, O^{3+}, O^{4+}, O^{5+}, O^{6+}, e^-) in addition to the 9 represented here. For our model energy distribution (figure 6.1), the formation energy proportion is essentially constant over $T_0 \in [10\,000\,\text{K}, 40\,000\,\text{K}]$ and constitutes between 58.3% and 59.4% of the total energy, even with varying peak ionization levels $Y_{O^+} \in [0.03, 0.85]$ and $Y_{O^{2+}} \in [1.9 \times 10^{-11}, 6.7 \times 10^{-2}]$.

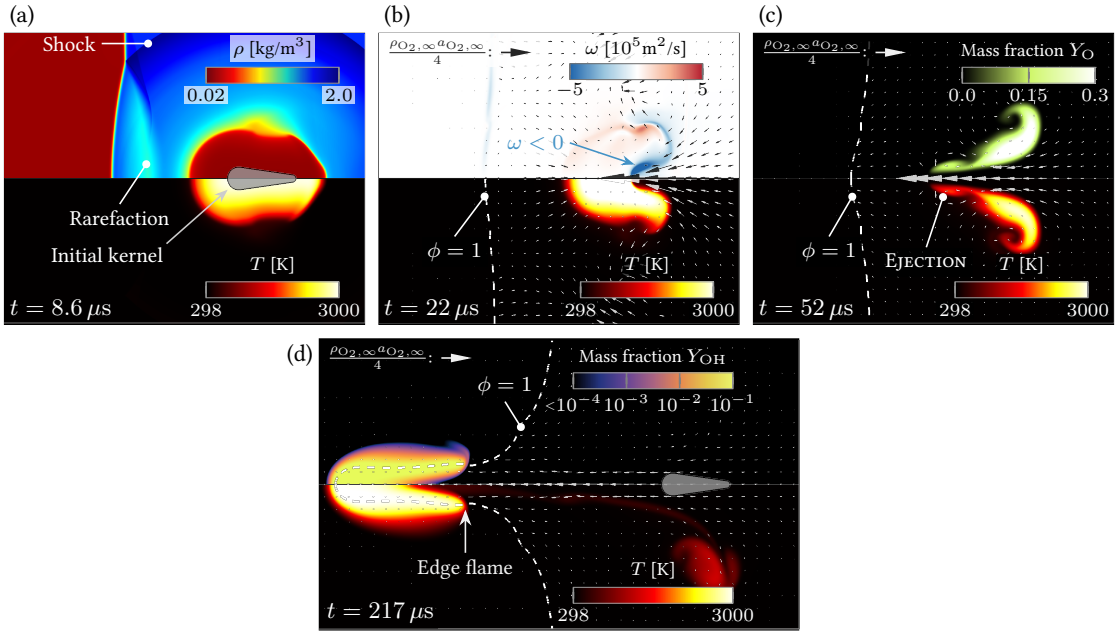

Figure 6.6: Evolution of the H_2–O_2 system (a) 8.6 μs, (b) 22 μs, (c) 52 μs, and (d) 217 μs after deposition with $\beta = 3$ and $d = 2L$, predicted by the detailed model. The momentum is shown in (b–d) instead of velocity due to the density variation, with its scale given in terms of its ambient value in O_2 at sonic velocity.

The reduced model similarly yields 59% formation energy with $T_0 = 63T_\infty$. Recombination is anticipated to be an important source of heat, as a portion of this energy is ultimately converted to sensible energy as the gas recombines. Thermal conduction competes with this as the gas cools while being convected toward the fuel. For the ejection, a Peclet number representing the ratio of a diffusion time scale $R_1^2/\pi^2\alpha_\infty$ to the ejection-arrival time d/u_j is

$$\mathrm{Pe}_j = \frac{u_j R_1^2}{\pi^2 d\alpha_\infty} = \mathrm{Re}\,\mathrm{Pr}\,\frac{\hat{u}_j \hat{R}_1^2}{\pi^2 \hat{d}}\,, \tag{6.13}$$

where u_j is the ejection velocity and $\alpha_\infty = \lambda_\infty/\rho_{O,\infty}c_{p,O}$ is the thermal diffusivity of the ambient oxidizer. The nondimensionalizations $\hat{u}_j = u_j/a_{O,\infty}$, $\hat{R}_1 = R_1/L$, and $\hat{d} = d/L$ match the reduced-model formulation (section 6.1.2), and R_1 is chosen as a characteristic radial dimension of the ejection.

To demonstrate the thermodynamic effect of radical recombination on ignition, figure 6.7(a) shows the dependence on Pe_j of the ejection temperature T_j/T_∞ at its time of contact with the fuel, for variable Da_2. The range of Pe_j correspond to $\beta \in [1.5, 3]$, which produced ejection velocities $u_j/a_{O,\infty} \in [0.05, 0.13]$, and $d/L \in [2, 3]$. The Prandtl number $\mathrm{Pr} \in [0.5, 1.0]$ is also varied to broaden the range of accessible Pe_j. For each Da_2, T_j increases with Pe_j, consistent with more rapid convective transport of hot gas compared to its diffusive loss. The largest Pe_j correspond to the most asymmetric kernels (large β and u_j) that are

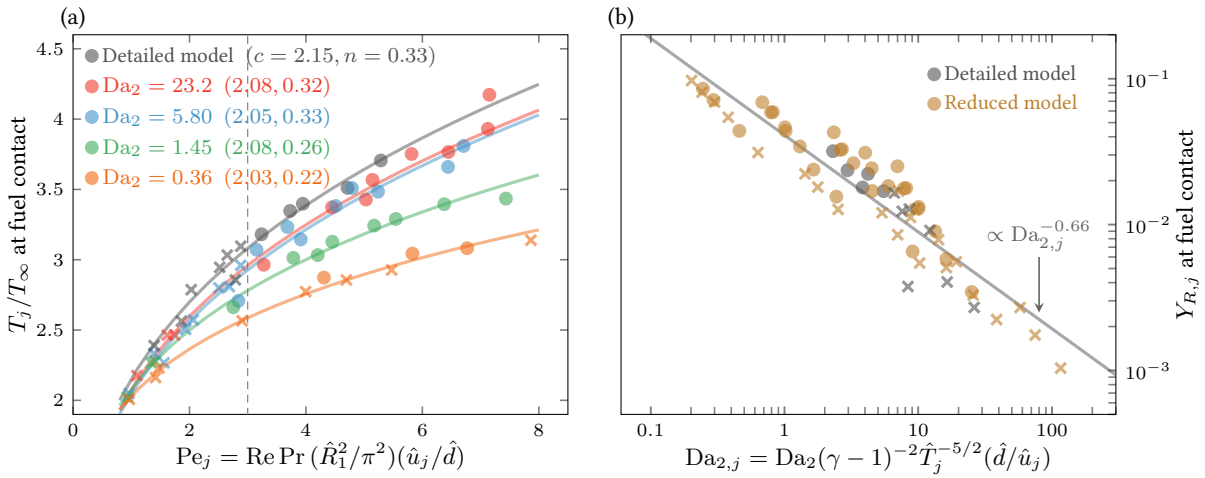

Figure 6.7: (a) Dependence on Pe_j (6.13) of ejection temperature T_j at its contact with the fuel for $\mathrm{Da}_2 \in [0.36, 23.2]$, computed with the reduced model; non-igniting cases are marked by an "×". Constants (c, n) for least-squares power-law fits $T_j/T_\infty = c\,\mathrm{Pe}_j^n$ are indicated in the legend. (b) Dependence of the radical mass fraction $Y_{R,j}$ of the ejection on $\mathrm{Da}_{2,j}$ (6.14).

deposited closer to the fuel (small d). T_j also increases with Da_2, as faster radical recombination produces more heat as the ejection propagates towards the fuel. For the parameter range shown, T_j can vary by up to T_∞ with respect to Da_2, with non-igniting cases being more prevalent for slow recombination ($\mathrm{Da}_2 = 0.36$) that results in lower T_j. As indicated by the dashed line in figure 6.7(a), ignition is likely to occur for $\mathrm{Pe}_j \gtrsim 3$; this threshold is expected to depend on fuel properties and the initial temperature T_0 of the kernel. The Reynolds number $\mathrm{Re} = 4.3 \times 10^4$ is fixed in figure 6.7, but preliminary calculations suggest that T_j has an explicit dependence on Re, in addition to Pe_j, due to subtle changes in the flow field that alter the temperature of the ejection at the time of its formation.

To quantify the relative rates of recombination and transport, a chemical time scale τ_r is formulated based on the recombination rate at p_∞ and T_j:

$$\frac{1}{\tau_r} = A_2 C_j^2 T_j^{-1/2} = A_2 C_\infty^2 T_\infty^{-1/2} \left(\frac{T_\infty}{T_j}\right)^{5/2},$$

where $C_j = p_\infty/\overline{R}T_j$. A corresponding Damköhler number $\mathrm{Da}_{2,j}$ representing the ratio of the ejection-arrival time d/u_j to τ_r is

$$\mathrm{Da}_{2,j} = A_2 C_\infty^2 T_\infty^{-1/2} \left(\frac{T_\infty}{T_j}\right)^{5/2} \frac{d}{u_j} = \mathrm{Da}_2 \frac{\hat{T}_j^{-5/2}}{(\gamma-1)^2} \frac{\hat{d}}{\hat{u}_j}. \tag{6.14}$$

As seen in figure 6.7(b), the radical content in the ejection decreases with $\mathrm{Da}_{2,j}$, as larger $\mathrm{Da}_{2,j}$ correspond to faster recombination relative to the time to reach the fuel. Though ignition does not appear to be sensitive to the radicals for the reduced model, likely due to their absence from directly participating in the combustion kinetics, the model does agree with the detailed one in $Y_{R,j}$ and furthermore suggests approximate proportionality to $\mathrm{Da}_{2,j}^{-0.66}$, based on a least-squares fit.

6.6 Ignition-suppressing breakdown-induced flow

When the kernel is deposited in close proximity to the fuel ($d \leq L$), the post-breakdown flow changes qualitatively from more distal depositions and, as seen in figure 6.3, can result in a reversal of the ejection and failure of ignition. The flow dynamics causing this is described for a $\beta = 1$, $d = L$ case using the detailed H_2–O_2 combustion model and with all other parameters matching those in section 6.5.

After deposition, the kernel temperature decays rapidly to $T < 3000\,\mathrm{K}$ due to its hydrodynamic expansion (figure 6.8a). This expansion occurs asymmetrically, apparent by comparison with a corresponding case without the interface, and is biased toward the fuel due to the lower density of hydrogen. A low-pressure region develops in the cavity generated by this expansion and draws flow towards the centerline (figure 6.8b), where it diverges in the axial direction. Though the kernel is composed predominantly of atomic oxygen, these radicals remains separated from the fuel by a layer of cold oxidizer. Roll-up of the interface due to shock-generated vorticity can be seen in the mixture fraction

$$Z = \frac{Z_\mathrm{H}/2W_\mathrm{H} + (Z_{\mathrm{O},0} - Z_\mathrm{O})/W_\mathrm{O}}{Z_{\mathrm{H},0}/2W_\mathrm{H} + Z_{\mathrm{O},0}/W_\mathrm{O}}\,,$$

where Z_H and Z_O are the mass fractions of elements H and O, respectively, and $Z_{\mathrm{O},0} = Z_{\mathrm{H},0} = 1$ [132, 133]. A stagnation point develops in this dense gas at (figure 6.8c), corresponding to flow that disperses the fuel and hot gas in opposite directions (figure 6.8d), ultimately leading to no ignition.

6.6.1 Atwood number dependence

The reduced model is used to analyze the effect of breakdown-induced flow on ignition for $\mathrm{At} \in [-0.3, 0.9]$, which includes heavy and light fuels, e.g. $\mathrm{At} = 0.88$ for hydrogen, $\mathrm{At} = 0.33$ for methane, and $\mathrm{At} = -0.29$ for butane. The flame temperature $T_f/T_\infty = 6$ and activation temperature $T_a/T_\infty = 43.2$ correspond to a Zel'dovich number of $T_a(T_f - T_\infty)/T_f^2 = 6$. The product molecular weight $\hat{W}_P$ is calculated from (6.10) with $\rho_u/\rho_b = 5$, and $s = 0.3$ is used as a representative value for hydrocarbons, e.g. $s = 0.25$ for methane,

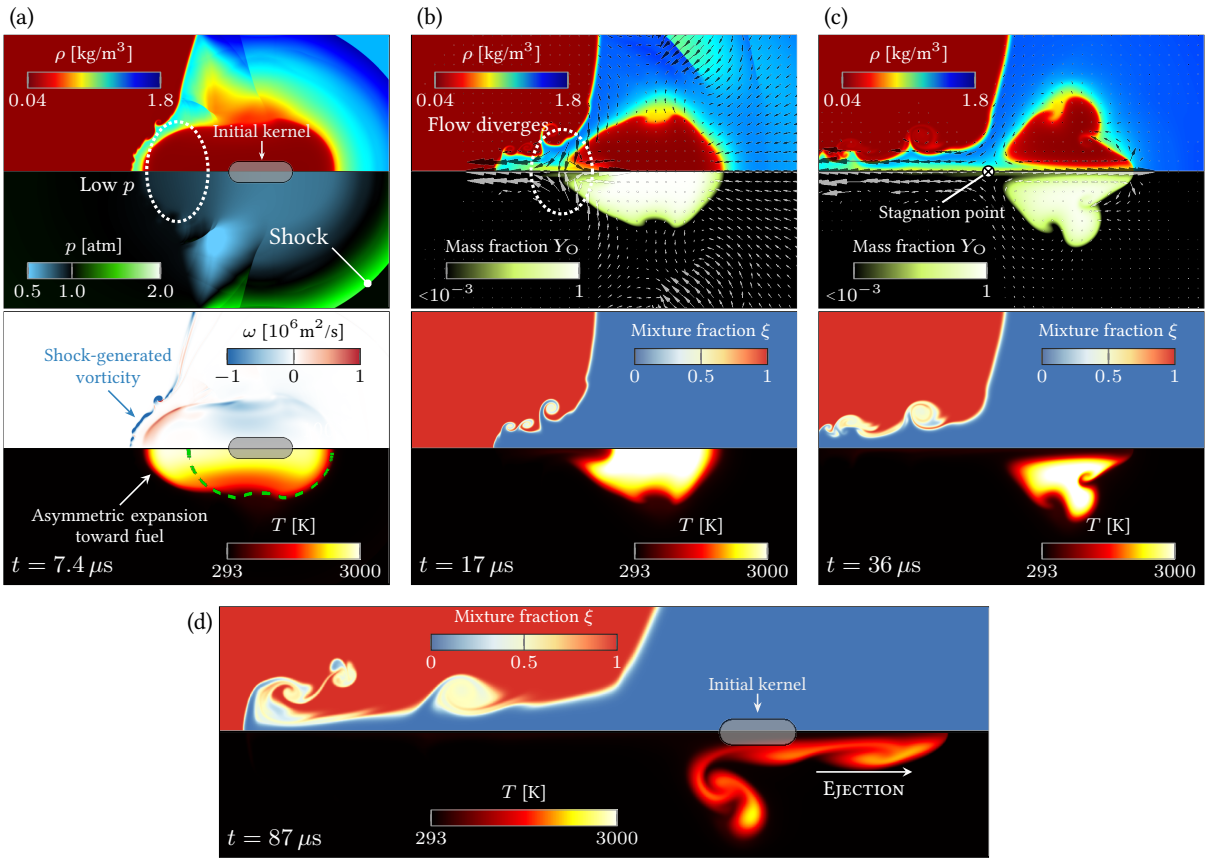

Figure 6.8: Evolution of a H_2–O_2 system (a) 7.4 μs, (b) 17 μs, (c) 36 μs, and (d) 87 μs after deposition at $d = L$ and with $\beta = 1$, predicted by the detailed model. The $T = 1500$ K contour for the corresponding case without the fuel interface is indicated by the dashed line in (a). Momentum vectors $\rho\boldsymbol{u}$ are shown instead of velocity in (b) and (c) due to the density variation.

$s = 0.325$ for acetylene, and $s = 0.279$ for butane. The coefficient ν_P is calculated from (6.9) and increases with decreasing At, consistent with combustion of heavy fuels. The initial peak temperature is $T_0 = 63T_\infty$, with (6.8) in equilibrium, and the total energy deposited is $E_0 = 27.6\gamma p_\infty L^3$, corresponding $E_0 = 31.3$ mJ with $p_\infty = 1$ atm and $\gamma = 1.4$. $\mathrm{Re} = 4.3 \times 10^4$, $\mathrm{Le} = 1$, and $\beta = 1$ are used throughout this section.

For $\mathrm{At} = 0.9$ (figure 6.9a), the kernel expands asymmetrically and protrudes into the low-density fuel, as seen at $t = 1.0L/a_{O,\infty}$. Hot gas pinches off at $t = 25L/a_{O,\infty}$ due to converging flow at the $r = 0$ centerline (e.g. figure 6.8a–c) and mixes with the fuel as it advects leftward. This strained vortical flow, visualized in the mixture-fraction inset, rapidly dissipates the pinched gas, which does not lead to sustained combustion. An ejection forms by $t = 42L/a_{O,\infty}$ and transports most of the heated gas away from the fuel. Though remnants of the kernel advect into the fuel ($t = 108L/a_{O,\infty}$), the temperature is too low for ignition.

For $\mathrm{At} = 0.3$ (figure 6.9b) the kernel expansion is approximately symmetric, resembling the corresponding case with no fuel interface, as seen at $t = 1.0L/a_{O,\infty}$. Perturbation of an otherwise spherical shock results from the differing speed of sound $a_{F,\infty}/a_{O,\infty} = \sqrt{W_O/W_F}$. The limited protrusion into the fuel does not lead

to pinch-off, and the ejection again propagates away from the fuel ($t = 25L/a_{O,\infty}$), which is characteristic of all At > 0 cases. At $t = 84L/a_{O,\infty}$, the kernel remnants make contact with the fuel after cooling significantly and are ultimately unable to ignite ($t = 372L/a_{O,\infty}$).

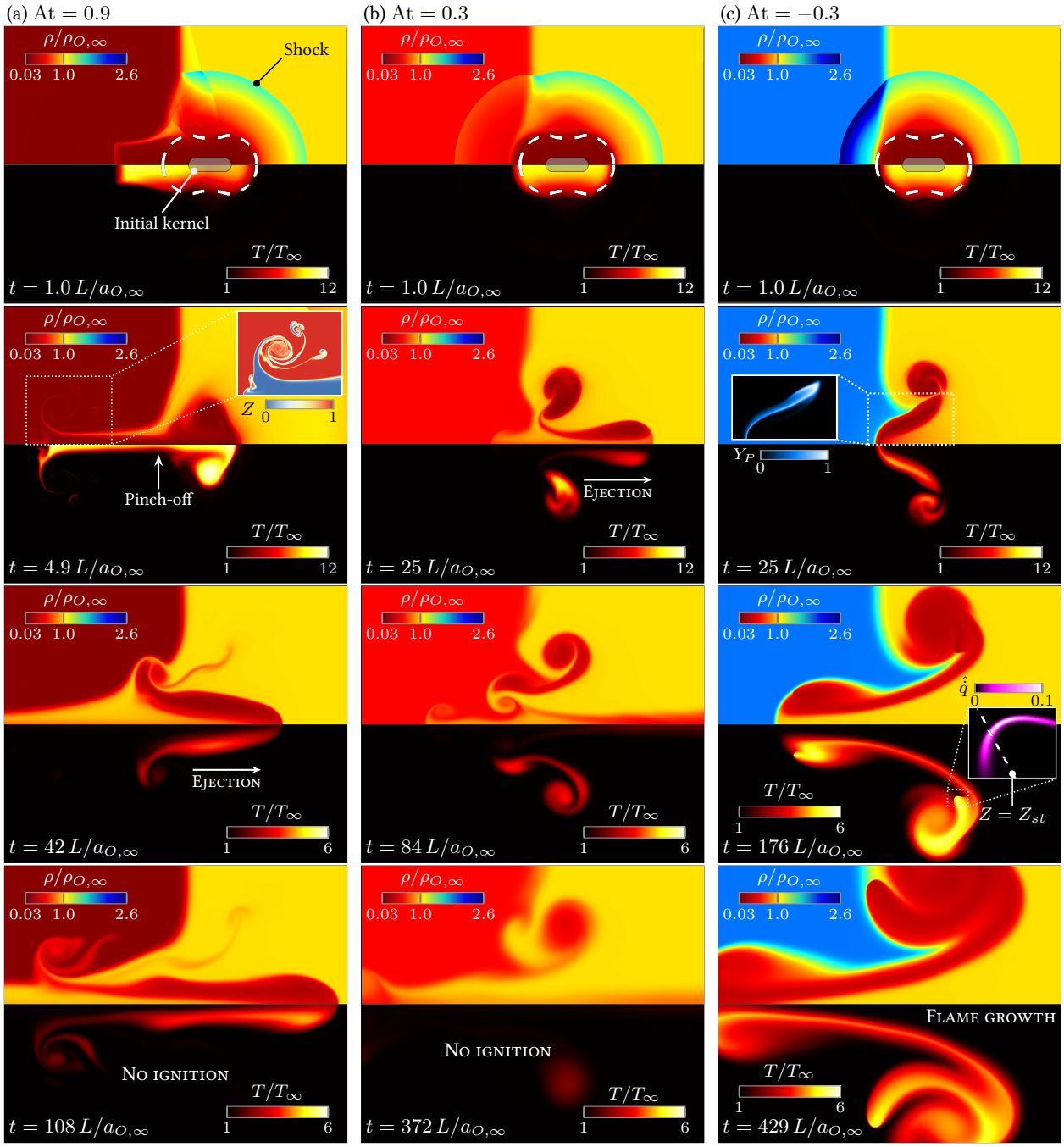

Figure 6.9: Evolution of $d = 0.8L$, $\beta = 1$ depositions for (a) At $= 0.9$, (b) At $= 0.3$, and (c) At $= -0.3$, with $\mathrm{Da}_1 = 3 \times 10^5$. The $T = 5T_\infty$ contour of a corresponding case without the fuel interface is indicated by the dashed line at $t = 1.0L/a_{O,\infty}$. Note the change in temperature scale.

In contrast to the At > 0 cases, the kernel makes sustained contact with the heavy At $= -0.3$ fuel (fig-

ure 6.9c), which is less perturbed by the kernel expansion due to its high density, and burns a thin layer of gas, as evidenced by Y_P in the $t = 25L/a_{O,\infty}$ inset. An edge flame forms by $t = 176L/a_{O,\infty}$, visualized by its heat release

$$\hat{\dot{q}} = \frac{L}{a_{O,\infty}} \frac{1}{C_\infty h_P^o W_P} \sum_k \dot{\omega}_k Y_k h_k W_k \,,$$

and competes with the flow induced by the vortex. The breakdown-induced flow is qualitatively different for this heavy-fuel case: instead of ejecting away from the fuel, hot gas penetrates *into* it. This results from vorticity generated at the R_2 end of the kernel; in a homogeneous gas this would be opposed by equal-magnitude vorticity (for $\beta = 1$) at the R_1 end (section 3.6.1), but its generation is disrupted here by the heavy fuel, resulting in the flow pattern seen at $t = 176L/a_{O,\infty}$. The combustion is sustained as the edge flame propagates radially outward along the interface, as seen at $t = 429L/a_{O,\infty}$.

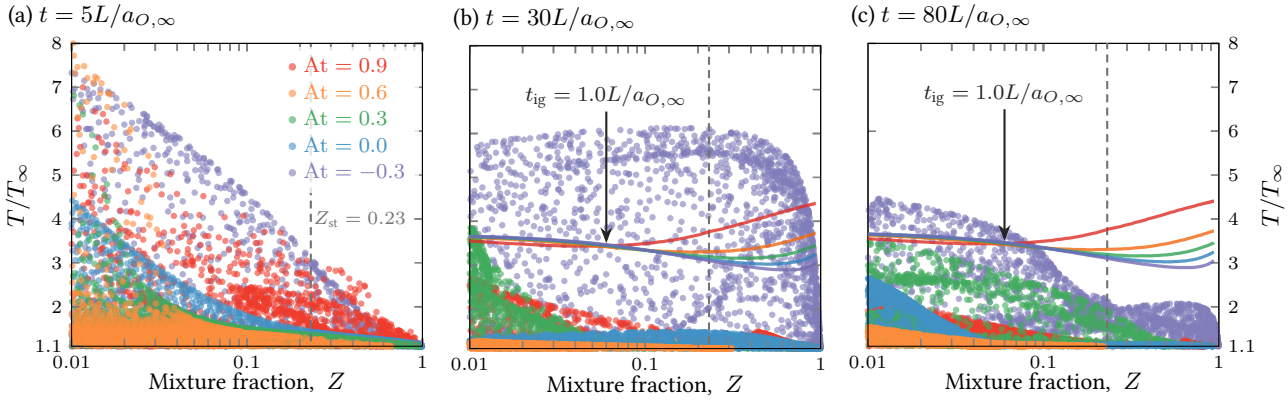

Figure 6.10: T versus Z at mesh points for $d = 0.8L$ and At $\in [-0.3, 0.9]$ at (a) $t = 5L/a_{O,\infty}$, (b) $t = 30L/a_{O,\infty}$, and (c) $t = 80/a_{O,\infty}$, computed with $\mathrm{Da}_1 = 0$. Every tenth mesh point is plotted. The stoichiometric mixture fraction $Z_{st} = s/(s+1) = 0.23$ is indicated. Isocontours of isobaric autoignition time $t_{ig} = 1.0L/a_{O,\infty}$, based on corresponding zero-dimensional calculations at each At, are shown for reference in (b) and (c).

The adverse effect of the breakdown-induced flow on ignition of light fuels (At > 0) is further evidenced by scatter plots of T and Z (figure 6.10), calculated with combustion-inert ($\mathrm{Da}_1 = 0$) simulations to isolate mixing induced by the flow dynamics. For the reduced model we use the mixture fraction

$$Z = \frac{Y_F/s - (Y_O + Y_R) + 1}{1 + 1/s} \,,$$

which is a conserved scalar that takes the values $Z = 0$ and $Z = 1$ in the ambient oxidizer and fuel, respectively. Though hot gas (e.g. $T \gtrsim 3T_\infty$) makes contact with the fuel at $t = 5L/a_{O,\infty}$ (figure 6.10a),

this is sustained only for At $= -0.3$ (figure 6.10b). For At $= 0.9$ the hot mixture is dissipated after pinch-off (figure 6.9a), and for At $= 0.6$ and At $= 0.3$ most of the heated gas is repelled from the fuel (e.g. figure 6.9b). Limited contact for At > 0 fuel is achieved later in time (figure 6.10c) due to slowly advecting remnants of the kernel (e.g. figure 6.9a and b), though its temperature is lower than that of the At $= -0.3$ mixture.

6.7 Breakdown in H_2 versus O_2

Given the sensitivity to the fuel density gradient and its impact on ignition, we anticipate that the flow dynamics will differ qualitatively depending on the location of the deposition, if the fuel and oxidizer have disparate molecular weights. Figure 6.11 shows the contrasting evolution following $\beta = 1$ depositions at $d = 2\,\text{mm}$ in H_2 and O_2, with comparable energies $E = 28.4\,\text{mJ}$ and $E = 31.2\,\text{mJ}$, respectively. Interaction between the expanding kernel and low-density H_2 (figure 6.11a), described in section 6.6, leads to ejection of gas away from the fuel and no ignition. However, when the energy is deposited in H_2, the interface is minimally perturbed and ignites shortly after deposition, leading to sustained combustion and propagation of an edge flame along the interface.

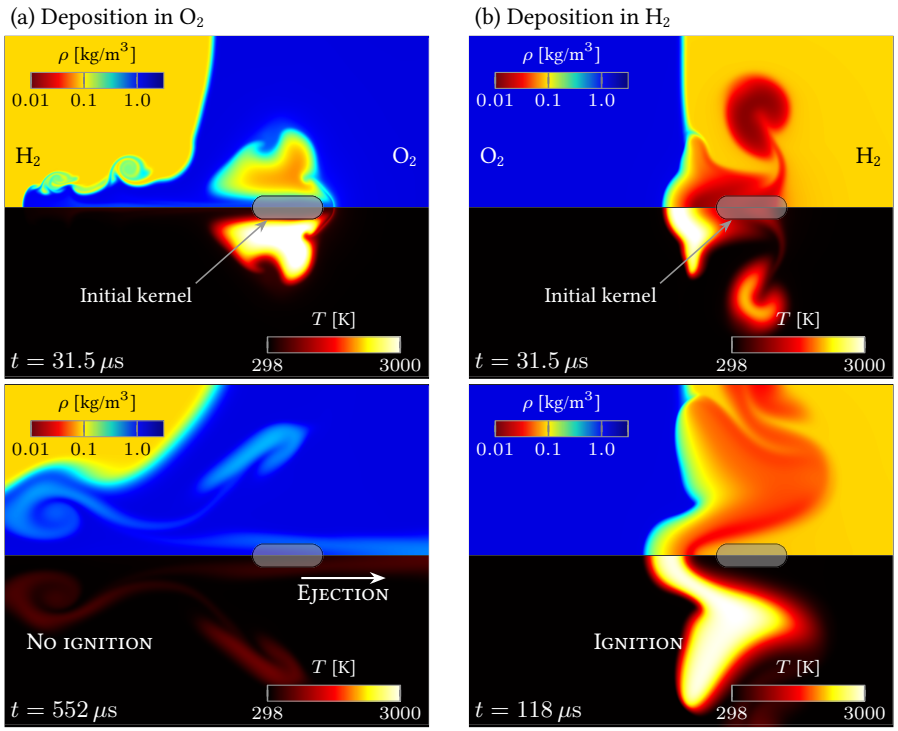

Figure 6.11: Deposition of a $\beta = 1$, $L = 2\,\text{mm}$ kernel at $d = 2\,\text{mm}$ in (a) oxygen and (b) hydrogen.

The phenomenology differs for a distal deposition ($d = 4\,\text{mm}$) that ignites by the ejection. For deposition in O_2 (figure 6.12a), the ejection penetrates into the fuel and ignites, whereas penetration is less pronounced for the corresponding H_2 deposition due to the high density of O_2. The H_2-ejection also reaches the interface

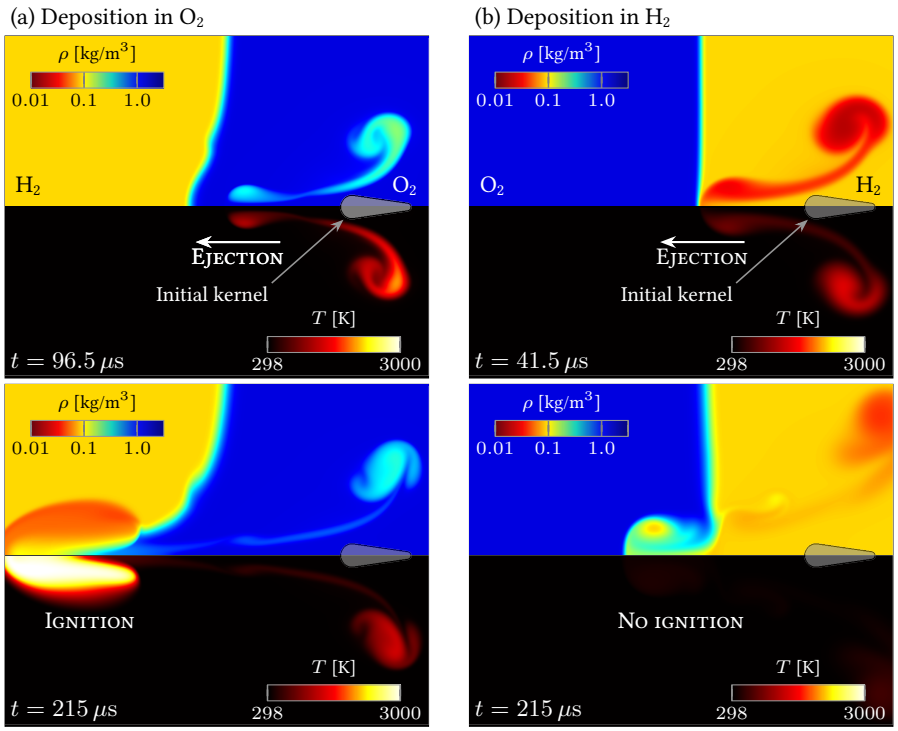

Figure 6.12: Deposition of a $\beta = 3$, $L = 2\,$mm kernel at $d = 4\,$mm in (a) oxygen and (b) hydrogen.

before its O_2 counterpart, consistent with its higher speed of sound $a_{H_2,\infty}/a_{O_2,\infty} = 4.01$ [125] and the fact that the vorticity-generating compressible-flow dynamics evolve on the acoustic time scale L/a_∞ (e.g. figure 3.24). The hot gas from the kernel also cools faster in H_2 as a result of its higher thermal conductivity ($\lambda_{H_2,\infty}/\lambda_{O_2,\infty} = 6.98$) [125], leading to ignition failure. The results of figures 6.11 and 6.12 suggest that in sufficiently nonpremixed H_2–O_2 flows, the location of the breakdown relative to local mixture gradients can significantly impact successful ignition.

Chapter 7

Concluding remarks

7.1 Research summary

The post-breakdown flow and ignition dynamics are analyzed with direct numerical simulation using five different gas models, selected to isolate various aspects of these dynamics. The breakdown-induced flow occurs primarily by hydrodynamic processes: many features observed in both single- and dual-pulse experiments are reproduced with a perfect-gas flow model. Of the two mechanisms previously thought to produce the distinct ejection of hot gas from the laser focal region, we show that baroclinic torque along the kernel boundary dominates over generation by the shock. These mechanisms are analyzed in detail using a semi-infinite analog that isolates vorticity generation at the ends of the kernel, and results are generalized to show that even subtle fore-aft asymmetry can lead to pronounced differences in the ensuing vorticity dynamics and ultimate ejection pattern, in some cases leading to its reversal.

This sensitivity can be leveraged to access a broader range of flow phenomenology using a secondary pulse. We show that relatively small changes in its strength, position, and timing can precipitate significant differences in the flow pattern. The proposed mechanisms by which this occurs can explain experimental observations of ejection suppression [71] and irregular flame-kernel morphologies [95] produced by dual pulses. It is further shown that the timing and position of two depositions can be controlled to produce double ejections that increase size of the resultant flame kernel, leading to a twofold enhancement in burning rate for depositions in a lean H_2–O_2 mixture, relative to a single pulse of equal total energy.

Given the sensitivity of the flow pattern to relatively mild alterations in these details of the deposition, aspects of coupling between nonequilibrium-plasma physics and the hydrodynamics are assessed using a

two-temperature argon-plasma model. By comparison with a two-species model, it is found that electron recombination, as a source of sensible energy, can significantly enhance the hydrodynamic expansion of the plasma, increasing its volume by a factor of 2.8 for the case analyzed. It is further shown that the nonequilibrium plasma kernel produces weaker vorticity than its perfect-gas counterpart, which delays the formation of the ejection.

Finally, the impact of these flow dynamics on ignition of a fuel–oxidizer interface is analyzed using a detailed H_2–O_2 combustion model and generalized to heavy fuels using a reduced model. Radical recombination is a crucial source of heat that maintains the temperature of the hot kernel remnants above ignition levels as they advect towards the fuel. It is found that for depositions near the interface ($d \lesssim L$), heavy fuels more readily ignite in the absence of an otherwise intense hydrodynamic interaction with the interface that disperses the hot gas and delays contact with a light fuel. This is shown to critically lead to ignition failure in certain cases, with the effect being particularly pronounced for a hydrogen–oxygen system.

7.2 Outlook

One theme of this work is the rich phenomenology that can be recovered with relatively simple modeling of the breakdown and gas properties. A missing but complex piece of this reduced-modeling framework is dependence on laser-device parameters, such as wavelength, focal length, or pulse width. While recent efforts [8, 70] have advanced knowledge of the early breakdown, a detailed description of how the post-breakdown kernel geometry, taken simply as a model input in this work, depends on laser parameters remains incomplete. Given the sensitivity of the flow characteristics to asymmetries in the kernel, understanding the relationship between its geometry and details of the breakdown would be important to developing an end-to-end model to map laser parameters onto the ultimate flow and ignition dynamics. Such a model would enable flexible deployment of laser-based energy depositions and control parameters, for example, to increase ignition probability in combustion devices.

While experiments suggest that the energy deposition and subsequent evolution is predominantly axisymmetric in a homogeneous gas, this is clearly untrue in general, particularly in nonuniform flows typically encountered in application environments. Mechanisms by which such pre-pulse inhomogeneities alter the breakdown-induced dynamics are largely unexplored. In particular, understanding the growth of three-dimensional irregularities, often unavoidable in realistic laser operation, into ostensibly turbulent flow and how this is influenced by plasma physics not only is of fundamental interest but also has practical impact: for example, instabilities can accelerate flame growth in laser-initiated combustion [129] and alter the dynamics

of a cavitating bubble in liquid, which drives certain modes of laser-induced droplet fragmentation [13]. Though currently limited due to their expense [129, 134, 135], simulations of such three-dimensional dynamics would greatly enhance understanding of the post-breakdown evolution. Two-dimensional axisymmetric simulations such as those presented here can also elucidate phenomenology, for example, by prescribing perturbations to the kernel geometry and introducing other forms of anticipated nonuniformity.

The simpler models employed can also be exercised in various configurations that are not pursued in this work. For example, the quasi-steady flow and mixing produced by a series of many coaxial pulses, observed to improve certain ignition characteristics [67], could be examined with an inert-gas model such as that used for our study of dual-pulse hydrodynamics; the relatively low simulation cost of such a model would facilitate analysis of the long-time flow behavior. The results of section 4.2 suggest that tuning the spatial offset and temporal separation of these pulses could lead to qualitatively different phenomenologies. The mean temperature and radical concentration produced by such a configuration would also be useful for assessing its efficacy for ignition.

While this work examines aspects of how plasma physics can affect the hydrodynamics, future efforts will include a more exhaustive analysis. Controlling the background pressure, kernel size, and kernel temperature in a way to alter the rates of relaxation, recombination, and electronic diffusion relative to the hydrodynamic expansion rate would elucidate possible coupling mechanisms. Analysis of these effects on the flow pattern can also be extended to diatomic molecules, which would introduce additional time scales associated with, for example, vibrational relaxation and heavy-particle recombination.

Appendix A

Treatment of the $r = 0$ coordinate singularity

A.1 Navier–Stokes equations at $r = 0$

The treatment at the $r = 0$ coordinate singularity is described here for the Navier–Stokes equations for reacting flow as an example, though the procedure is identical for all physical models. The governing equations are, in expanded form,

$$
\begin{aligned}
\frac{\partial \rho}{\partial t} &= -\frac{\partial(\rho u_x)}{\partial x} - \frac{1}{r}\frac{\partial(r\rho u_r)}{\partial r} \\
\frac{\partial \rho u_x}{\partial t} &= -\frac{\partial p}{\partial x} - \frac{\partial(\rho u_x^2)}{\partial x} - \frac{1}{r}\frac{\partial(r\rho u_x u_r)}{\partial r} + t_x \\
\frac{\partial \rho u_r}{\partial t} &= -\frac{\partial p}{\partial r} - \frac{\partial(\rho u_x u_r)}{\partial x} - \frac{1}{r}\frac{\partial(r\rho u_r^2)}{\partial r} + t_r \\
\frac{\partial \rho(e+|\boldsymbol{u}|^2/2)}{\partial t} &= -\frac{\partial[\rho(e+|\boldsymbol{u}|^2)+p]u_x}{\partial x} - \frac{1}{r}\frac{\partial r[\rho(e+|\boldsymbol{u}|^2)+p]u_r}{\partial r} + u_x t_x + u_r t_r + \eta\left[\frac{\partial u_x}{\partial x} + \frac{1}{r}\frac{\partial(r u_r)}{\partial r}\right]^2 \\
&\quad + \mu\left[2\left(\frac{\partial u_x}{\partial x}\right)^2 + 2\left(\frac{\partial u_r}{\partial r}\right)^2 + \left(\frac{\partial u_x}{\partial r} + \frac{\partial u_r}{\partial x}\right)^2 + 2\left(\frac{u_r}{r}\right)^2\right] + \lambda\left(\frac{\partial^2 T}{\partial x^2} + \frac{\partial^2 T}{\partial r^2} + \frac{1}{r}\frac{\partial T}{\partial r}\right) \\
&\quad + \frac{\partial \lambda}{\partial x}\frac{\partial T}{\partial x} + \frac{\partial \lambda}{\partial r}\frac{\partial T}{\partial r} + \sum_{k=1}^{N}\left[\nabla\left(\rho h_k D_k \frac{W_k}{W}\right)\cdot\nabla X_k + \rho h_k D_k \frac{W_k}{W}\nabla^2 X_k\right]
\end{aligned}
$$

$$
\begin{aligned}
&- \sum_{k=1}^{N}\sum_{l=1}^{N}\left[\nabla\left(\rho h_k Y_k D_l \frac{W_l}{W}\right)\cdot\nabla X_l + \rho h_k Y_k D_l \frac{W_l}{W}\nabla^2 X_l\right] \\
\frac{\partial \rho Y_k}{\partial t} =& -\frac{\partial(\rho Y_k u_x)}{\partial x} - \frac{1}{r}\frac{\partial(r\rho Y_k u_r)}{\partial r} + \nabla\left(\rho D_k \frac{W_k}{W}\right)\cdot\nabla X_k + \rho D_k \frac{W_k}{W}\nabla^2 X_k \\
&- \sum_{l=1}^{N}\left[\nabla\left(\rho Y_k D_l \frac{W_l}{W}\right)\cdot\nabla X_l + \rho Y_k D_l \frac{W_l}{W}\nabla^2 X_l\right] + W_k\dot{\omega}_k,
\end{aligned}
$$

where

$$
\begin{aligned}
t_x =& \mu\left(\frac{\partial^2 u_x}{\partial r^2} + \frac{\partial^2 u_r}{\partial x \partial r} + \frac{1}{r}\frac{\partial u_x}{\partial r} + \frac{1}{r}\frac{\partial u_r}{\partial x} + 2\frac{\partial^2 u_x}{\partial x^2}\right) + \eta\left(\frac{\partial^2 u_r}{\partial r \partial x} + \frac{1}{r}\frac{\partial u_r}{\partial x} + \frac{\partial^2 u_x}{\partial x^2}\right) \\
&+ 2\frac{\partial u_x}{\partial x}\frac{\partial \mu}{\partial x} + \left(\frac{\partial u_x}{\partial r} + \frac{\partial u_r}{\partial x}\right)\frac{\partial \mu}{\partial r} + \left(\frac{\partial u_x}{\partial x} + \frac{1}{r}\frac{\partial (r u_r)}{\partial r}\right)\frac{\partial \eta}{\partial x} \\
t_r =& \mu\left(\frac{\partial^2 u_x}{\partial r \partial x} + \frac{\partial^2 u_r}{\partial x^2} + \frac{2}{r}\frac{\partial u_r}{\partial r} - \frac{2u_r}{r^2} + 2\frac{\partial^2 u_r}{\partial r^2}\right) + \eta\left(\frac{\partial^2 u_r}{\partial r^2} + \frac{1}{r}\frac{\partial u_r}{\partial r} - \frac{u_r}{r^2} + \frac{\partial^2 u_x}{\partial x \partial r}\right) \\
&+ \left(\frac{\partial u_x}{\partial r} + \frac{\partial u_r}{\partial x}\right)\frac{\partial \mu}{\partial x} + 2\frac{\partial u_r}{\partial r}\frac{\partial \mu}{\partial r} + \left(\frac{\partial u_x}{\partial x} + \frac{1}{r}\frac{\partial (r u_r)}{\partial r}\right)\frac{\partial \eta}{\partial r},
\end{aligned}
$$

and $\eta = \mu_B - 2\mu/3$. The equations at $r = 0$ are evaluated in their $r \to 0$ limit, and terms multiplying $1/r$ converge; for example,

$$
\begin{aligned}
&\lim_{r\to 0}\frac{1}{r}\frac{\partial(r\rho u_r)}{\partial r} = 2\rho\frac{\partial u_r}{\partial r}\bigg|_{r=0} \\
&\lim_{r\to 0}\frac{1}{r}\frac{\partial(r\rho u_r^2)}{\partial r} = 0 \\
&\lim_{r\to 0}\frac{1}{r}\frac{\partial u_x}{\partial r} = \frac{\partial^2 u_x}{\partial r^2}\bigg|_{r=0} \\
&\lim_{r\to 0}\frac{1}{r}\frac{\partial u_r}{\partial x} = \frac{\partial^2 u_r}{\partial x \partial r}\bigg|_{r=0} \\
&\lim_{r\to 0}\left(\frac{1}{r}\frac{\partial u_r}{\partial r} - \frac{u_r}{r^2}\right) = 0
\end{aligned}
$$

For axisymmetric flow, all flow variables are even functions of r for except u_r, which is an odd function of r [77]. The governing equations at $r = 0$ are

$$
\begin{aligned}
\frac{\partial \rho}{\partial t} &= -\frac{\partial(\rho u_x)}{\partial x} - 2\rho\frac{\partial u_r}{\partial r} \\
\frac{\partial(\rho u_x)}{\partial t} &= -\frac{\partial p}{\partial x} - \frac{\partial(\rho u_x^2)}{\partial x} - 2\rho u_x\frac{\partial u_r}{\partial r} + t_x \\
\frac{\partial(\rho u_r)}{\partial t} &= 0 \\
\frac{\partial(\rho(e+|\boldsymbol{u}|^2/2)}{\partial t} &= -\frac{\partial[(\rho(e+|\boldsymbol{u}|^2/2)+p)u_x]}{\partial x} - 2[\rho(e+|\boldsymbol{u}|^2/2+p)]\frac{\partial u_r}{\partial r} + u_x t_x + \eta\left(\frac{\partial u_x}{\partial x} + 2\frac{\partial u_r}{\partial r}\right)^2 \\
&\quad + \mu\left[2\left(\frac{\partial u_x}{\partial x}\right)^2 + 4\left(\frac{\partial u_r}{\partial r}\right)^2\right] + \lambda\left(\frac{\partial^2 T}{\partial x^2} + 2\frac{\partial^2 T}{\partial r^2}\right) + \frac{\partial \lambda}{\partial x}\frac{\partial T}{\partial x} \\
&\quad + \sum_{k=1}^{N}\left[\frac{\partial(\rho h_k D_k W_k/W)}{\partial x}\frac{\partial X_k}{\partial x} + \rho h_k D_k\frac{W_k}{W}\left(\frac{\partial^2 X_k}{\partial x^2} + 2\frac{\partial^2 X_k}{\partial r^2}\right)\right] \\
&\quad - \sum_{k=1}^{N}\sum_{l=1}^{N}\left[\frac{\partial(\rho Y_k h_k D_l W_l/W)}{\partial x}\frac{\partial X_l}{\partial x} + \rho Y_k h_k D_l\frac{W_l}{W}\left(\frac{\partial^2 X_l}{\partial x^2} + 2\frac{\partial^2 X_l}{\partial r^2}\right)\right] \\
\frac{\partial \rho Y_k}{\partial t} &= -\frac{\partial(\rho Y_k u_x)}{\partial x} - 2\rho Y_k\frac{\partial u_r}{\partial r} + \frac{\partial(\rho D_k W_k/W)}{\partial x}\frac{\partial X_k}{\partial x} + \rho D_k\frac{W_k}{W}\left(\frac{\partial^2 X_k}{\partial x^2} + 2\frac{\partial^2 X_k}{\partial r^2}\right) \\
&\quad - \sum_{l=1}^{N}\left[\frac{\partial(\rho Y_k D_l W_l/W)}{\partial x}\frac{\partial X_l}{\partial x} + \rho Y_k\frac{D_l}{X_l}\left(\frac{\partial^2 X_l}{\partial x^2} + 2\frac{\partial^2 X_l}{\partial r^2}\right)\right] + W_k\dot{\omega}_k,
\end{aligned}
$$

where

$$
t_x = \mu\left(2\frac{\partial^2 u_x}{\partial r^2} + 2\frac{\partial^2 u_r}{\partial x\partial r} + 2\frac{\partial^2 u_x}{\partial x^2}\right) + \eta\left(2\frac{\partial^2 u_r}{\partial x\partial r} + \frac{\partial^2 u_x}{\partial x^2}\right) + 2\frac{\partial u_x}{\partial x}\frac{\partial \mu}{\partial x} + \left(\frac{\partial u_x}{\partial x} + 2\frac{\partial u_r}{\partial r}\right)\frac{\partial \eta}{\partial x}
$$

A.2 Shock-capturing

The artificial bulk viscosity model used in chapters 5 and 6 is

$$
\mu_B = \overline{C\rho|D^4(\nabla\cdot\boldsymbol{u})H(-\nabla\cdot\boldsymbol{u})|}\,,
$$

where C is a parameter, H is the Heaviside step function, D^4 is a mesh-dependent biharmonic-like operator

with cross-derivatives removed, and the overbar denotes Gaussian filtering [105]. D^4 in cylindrical polar coordinates is

$$D^4(\nabla\cdot\boldsymbol{u}) = \frac{\partial^4(\nabla\cdot\boldsymbol{u})}{\partial x^4}\delta_x^6 + \left[\frac{\partial^4(\nabla\cdot\boldsymbol{u})}{\partial r^4} + \frac{2}{r}\frac{\partial^3(\nabla\cdot\boldsymbol{u})}{\partial r^3} - \frac{1}{r^2}\frac{\partial^2(\nabla\cdot\boldsymbol{u})}{\partial r^2} + \frac{1}{r^3}\frac{\partial(\nabla\cdot\boldsymbol{u})}{\partial r}\right]\delta_r^6 \tag{A.1}$$

where $\delta_i \equiv (\Delta x_i \boldsymbol{e}_i)\cdot\frac{\nabla\rho}{|\nabla\rho|}$ and Δx_i is the grid spacing [106]. Because r-derivatives and the $r\to 0$ limit do not commute, we expand terms in (A.1):

$$\begin{aligned}
\nabla\cdot\boldsymbol{u} &= \frac{\partial u_x}{\partial x} + \frac{\partial u_r}{\partial r} + \frac{u_r}{r}\\
\frac{1}{r^3}\frac{\partial(\nabla\cdot\boldsymbol{u})}{\partial r} &= \frac{1}{r^3}\left[\frac{\partial^2 u_x}{\partial x\partial r} + \frac{\partial^2 u_r}{\partial r^2} + \frac{1}{r^2}\left(r\frac{\partial u_r}{\partial r} - u_r\right)\right]\\
-\frac{1}{r^2}\frac{\partial^2(\nabla\cdot\boldsymbol{u})}{\partial r^2} &= -\frac{1}{r^2}\left[\frac{\partial^3 u_x}{\partial x\partial r^2} + \frac{\partial^3 u_r}{\partial r^3} + \frac{1}{r^3}\left(r^2\frac{\partial^2 u_r}{\partial r^2} - 2r\frac{\partial u_r}{\partial r} + 2u_r\right)\right]\\
\frac{2}{r}\frac{\partial^3(\nabla\cdot\boldsymbol{u})}{\partial r^3} &= \frac{2}{r}\left[\frac{\partial^4 u_x}{\partial x\partial r^3} + \frac{\partial^4 u_r}{\partial r^4} + \frac{1}{r^4}\left(r^3\frac{d^3 u_r}{\partial r^3} - 3r^2\frac{\partial^2 u_r}{\partial r^2} + 6r\frac{\partial u_r}{\partial r} - 6u_r\right)\right]\\
\frac{\partial^4(\nabla\cdot\boldsymbol{u})}{\partial r^4} &= \frac{\partial^5 u_x}{\partial x\partial r^4} + \frac{\partial^5 u_r}{\partial r^5} + \frac{1}{r^5}\left(r^4\frac{\partial^4 u_r}{\partial r^4} - 4r^3\frac{\partial^3 u_r}{\partial r^3} + 12r^2\frac{\partial^2 u_r}{\partial r^2} - 24r\frac{\partial u_r}{\partial r} + 24u_r\right)
\end{aligned}$$

It can be shown that

$$\lim_{r\to 0}\frac{1}{r^3}\left(\frac{\partial u_x}{\partial r} - r\frac{\partial^2 u_x}{\partial r^2} + 2r^2\frac{\partial^3 u_x}{\partial r^3} + r^3\frac{\partial^4 u_x}{\partial r^4}\right) = \frac{8}{3}\frac{\partial^4 u_x}{\partial r^4}\bigg|_{r=0}$$

where u_x is an even function of r for axisymmetric flow, and

$$\begin{aligned}
\lim_{r\to 0}\frac{1}{r^5}\left(r^2\frac{\partial^2 u_r}{\partial r^2} + r\frac{\partial u_r}{\partial r} - u_r\right) &= \frac{1}{5}\frac{\partial^5 u_r}{\partial r^5}\bigg|_{r=0}\\
\lim_{r\to 0}\frac{1}{r^5}\left(r^4\frac{\partial^4 u_r}{\partial r^4} + r^3\frac{\partial^3 u_r}{\partial r^3} - 3r^2\frac{\partial^2 u_r}{\partial r^2} + 6r\frac{\partial u_r}{\partial r} - 6u_r\right) &= \frac{12}{5}\frac{\partial^5 u_r}{\partial r^5}\bigg|_{r=0}
\end{aligned}$$

$$\lim_{r\to 0}\frac{1}{r^5}\left(r^3\frac{\partial^3 u_r}{\partial r^3}+r^2\frac{\partial^2 u_r}{\partial r^2}-2r\frac{\partial u_r}{\partial r}+2u_r\right)=\frac{3}{5}\frac{\partial^5 u_r}{\partial r^5}\bigg|_{r=0}$$

$$\lim_{r\to 0}\frac{1}{r^5}\left(r^5\frac{\partial^5 u_r}{\partial r^5}+r^4\frac{\partial^4 u_r}{\partial r^4}-4r^3\frac{\partial^3 u_r}{\partial r^3}+12r^2\frac{\partial^2 u_r}{\partial r^2}-24r\frac{\partial u_r}{\partial r}+24u_r\right)=\frac{6}{5}\frac{\partial^5 u_r}{\partial r^5}\bigg|_{r=0}$$

where u_r is an odd function of r. The following expression is obtained at $r=0$:

$$D^4(\nabla\cdot\boldsymbol{u})\big|_{r=0}=\frac{\partial(\nabla\cdot\boldsymbol{u})^4}{\partial x^4}\bigg|_{r=0}\delta_x^6+\left[\frac{8}{3}\frac{\partial^5 u_x}{\partial x\partial r^4}\bigg|_{r=0}+\frac{16}{5}\frac{\partial^5 u_r}{\partial r^5}\bigg|_{r=0}\right]\delta_r^6$$

where the r-derivatives at $r=0$ are evaluated with appropriate modifications to the finite-difference stencils to reflect the r-parity of u_x and u_r. For spherically symmetric flow such as that analyzed in section 5.3, the D^4 operator is

$$D^4(\nabla\cdot\boldsymbol{u})=\left[\frac{\partial^4(\nabla\cdot\boldsymbol{u})}{\partial r^4}+\frac{4}{r}\frac{\partial^3(\nabla\cdot\boldsymbol{u})}{\partial r^3}\right]\delta_r^6$$

Following a similar procedure leads to

$$D^4(\nabla\cdot\boldsymbol{u})\big|_{r=0}=7\frac{\partial^5 u_r}{\partial r^5}\bigg|_{r=0}\delta_r^6$$

Fifth-order derivatives are computed by consecutive applications of the fourth-order and first-order derivatives.

Appendix B

Code verification

B.1 Method of manufactured solutions

The governing equations for each of the five gas models are independently verified to converge at the expected order of spatial accuracy using the method of manufactured solutions. For example, for the reduced combustion model (section 6.1.2), primitive variables are prescribed as

$$\begin{aligned}
\rho &= 1.5 + \sin(c_1 x)\cos(c_2 r), & \xi &= \sin(c_1 x)\sin(c_2 r) \\
u_x &= \sin(c_2 x)\cos(c_1 r), & Y_F &= 0.2 + 0.1[2 + \sin(c_2 x) + \cos(c_1 r)] \\
u_r &= \cos(c_2 x)\sin(c_1 r), & Y_O &= 0.2 + 0.1[2 + \sin(c_1 x) + \cos(c_2 r)] \\
e &= 1.5 + \cos(c_1 x)\sin(c_2 r), & Y_R &= 0.2 + 0.1[2 + \sin(c_2 x) + \cos(c_2 r)]\,,
\end{aligned}$$

where $c_1 = 37$ and $c_2 = 41$. The right-hand-side of the governing equations are evaluated numerically and compared with the corresponding result using a symbolic engine such as Mathematica [136], used to calculate all derivatives and limits analytically. Figure B.1 shows eighth-order convergence for the reduced-combustion model as an example.

An analogous approach is used to verify fourth-order accuracy of the explicit Runge-Kutta time-integration scheme. Additional tests are used for various submodels, as outlined in the following sections.

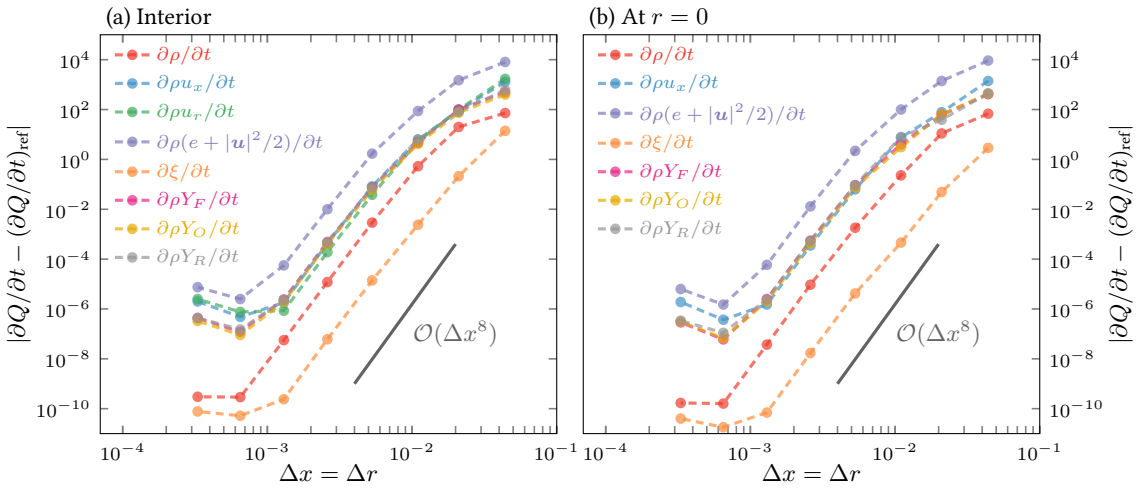

Figure B.1: Verification of eighth-order spatial convergence (a) on the interior of the simulation domain and (b) at $r = 0$, excluding boundary points in x; Q denotes the solved flow quantities.

B.2 Shock capturing

The Shu-Osher problem [137] is used to verify implementation of the shock capturing scheme [106]. Third and fourth derivatives, used exclusively for shock-capturing terms, are computed with a sixth-order, nine-point explicit differencing. An eighth-order implicit filter [75] with $\alpha = 0.495$ [76] is applied to conserved variables at the end of each time step; this was necessary reproduced published results, as its explicit counterpart destroys the fine-scale structures of the Shu-Osher problem. Figure B.2 shows the verification test case, which closely resembles results of Kawai et al. [106].

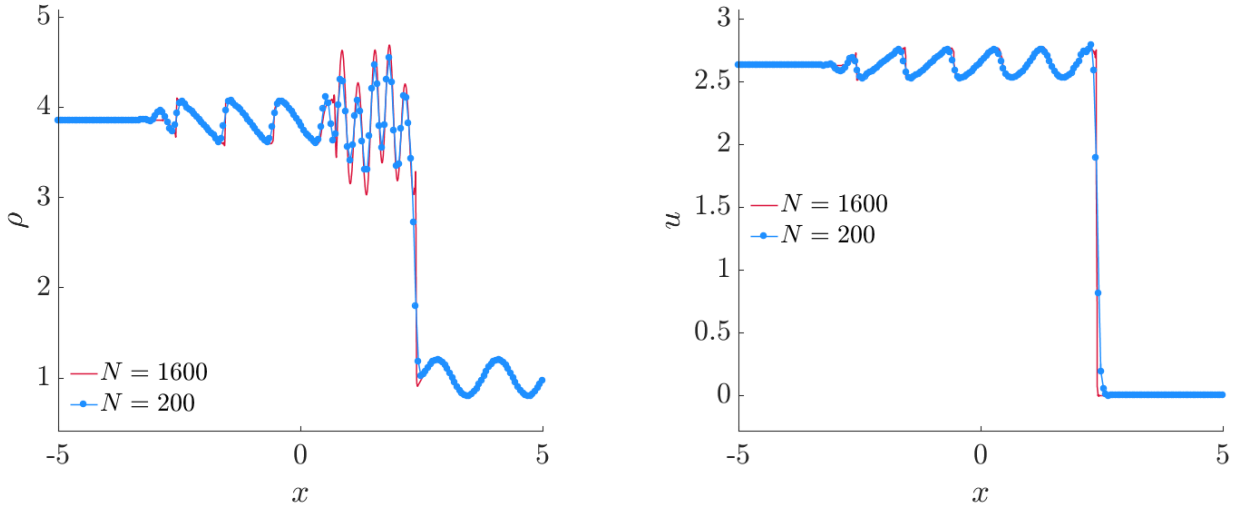

Figure B.2: Density and velocity fields of the Shu-Osher problem [137] at $t = 1.8$.

B.3 Navier–Stokes post-shock conditions

In addition to mesh independence of circulation Γ, we also verify that the post-shock conditions for the perfect-gas model, which does not employ shock-capturing, are insensitive by comparison with the inviscid result computed with a Riemann solver [138]. The discontinuity is initialized with $\rho = \rho_\infty$ and T_0/T_∞ corresponding to cases shown in section 3.4.4; finer mesh spacing is used for more intense cases (table B.1). Figure B.3 shows close agreement between the perfect-gas model and Riemann solver. For the most intense case $T_0/T_\infty = 72$, there is only a 0.4% discrepancy in the post-shock velocity and pressure.

T_0/T_∞	8.9	17.9	26.9	35.8	72.0
Mesh spacing $\Delta x/L$	5×10^{-4}	5×10^{-4}	5×10^{-4}	2.5×10^{-4}	1.25×10^{-4}

Table B.1: Mesh spacing used for comparing shock-jump conditions between the perfect-gas model and Riemann solver.

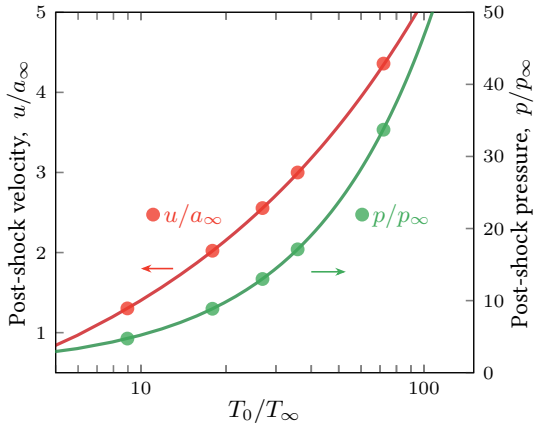

Figure B.3: Comparison of the post-shock velocity and pressure computed using a Riemann solver (lines) and the perfect-gas model (circles).

B.4 Combustion submodels

B.4.1 Autoignition

Implementation of the chemical source terms is verified using zero-dimensional adiabatic simulations. The composition for the constant-h, constant-p system is governed by

$$\dot{Y}_k = \frac{W_k \dot{\omega}_k}{\rho}, \qquad h \equiv \sum_{k=1}^{N_s} h_k(T) Y_k = \text{const.},$$

where $h_k(T) \equiv h^o + \int_{T^o}^{T} c_{p,k}(\tilde{T})\, \mathrm{d}\tilde{T}$ is the specific enthalpy of the k-th species. NASA-7 polynomials are used

to compute thermodynamic quantities [139]. Figure B.4 shows close agreement with published autoignition times [e.g. 140] of the 8-species 21-step San Diego mechanism [98].

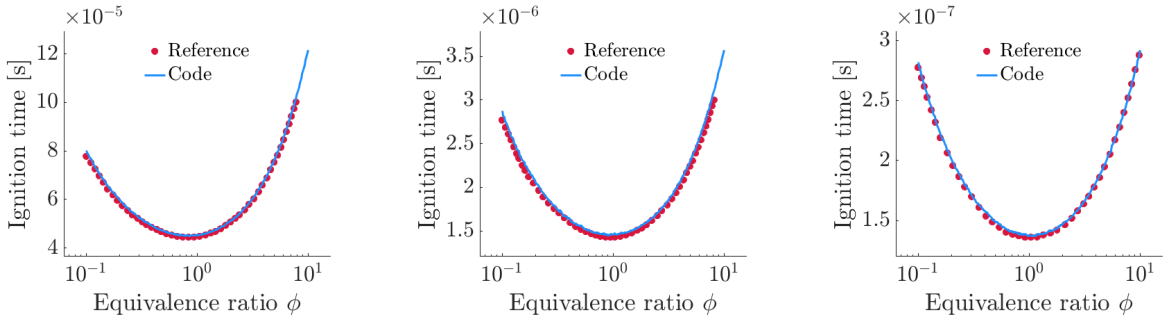

Figure B.4: Ignition delay time for (a) $T_0 = 1200\,\mathrm{K}$, $p = 1\,\mathrm{atm}$ (b) $T_0 = 1500\,\mathrm{K}$, $p = 10\,\mathrm{atm}$, and (c) $T_0 = 1800\,\mathrm{K}$, $p = 50\,\mathrm{atm}$.

B.4.2 Premixed laminar flame

Implementation of transport properties is verified with premixed flame simulations. Premixed flame speeds over a range of equivalence ratios ϕ are computed with one-dimensional direct numerical simulations and compared with computation by Cantera library [124]. Flame speeds are averaged over a time interval of 1 ms and computed by subtracting the upstream velocity from that of the flame front:

$$S_L = U_{\mathrm{flame}} - u(x = x_{\mathrm{flame}} + 4\delta_F), \quad \text{where} \quad \delta_F \equiv \frac{T_{\max} - T_{\min}}{\max\{\mathrm{d}T/\,\mathrm{d}x\}}\,.$$

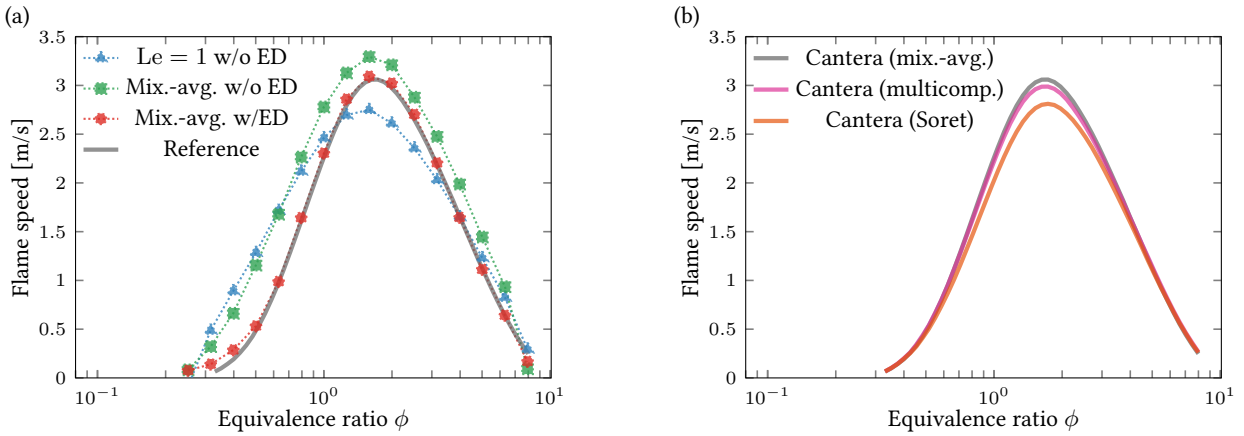

Figure B.5: (a) Verification of the current model—mixture-averaged diffusion with enthalpy diffusion (ED)—and effect of reduced modeling choices. (b) Effect of multicomponent diffusion and Soret effect.

Figure B.5 shows close agreement between the current implementation and Cantera as well as the effect of several modeling choices for mass and enthalpy diffusion, though all simulations include the enthalpy

diffusion term. Detailed analysis of its effect in reactive flows has been conducted by Cook [141]. The small discrepancy in the flame speed near the lean flammability limit is likely due to numerical errors in computing the speed of the slow-moving flame front during post-processing.

Appendix C

Nonequilibrium-plasma model verification

C.1 Plasma properties

Collision integrals (5.11) computed for argon with the present model (section 5.1.1) are in good agreement with detailed calculations by Devoto [110] (figure C.1). Transport properties, shown for $p = 1\,\text{atm}$ in figure C.2, show approximate agreement, with some discrepancy in the viscosity and electronic thermal conductivity. The enthalpy and electron number density are also seen to agree with detailed calculations by Murphy and Arundelli [142] and Murphy and Tam [143] for $T \lesssim 20\,000\,\text{K}$, beyond which multiply ionized species lead to discrepancy. The decrease in n_e for $T \gtrsim 17\,000\,\text{K}$ is due to decreasing total number density $\sum_k n_k$ with respect to T at constant pressure.

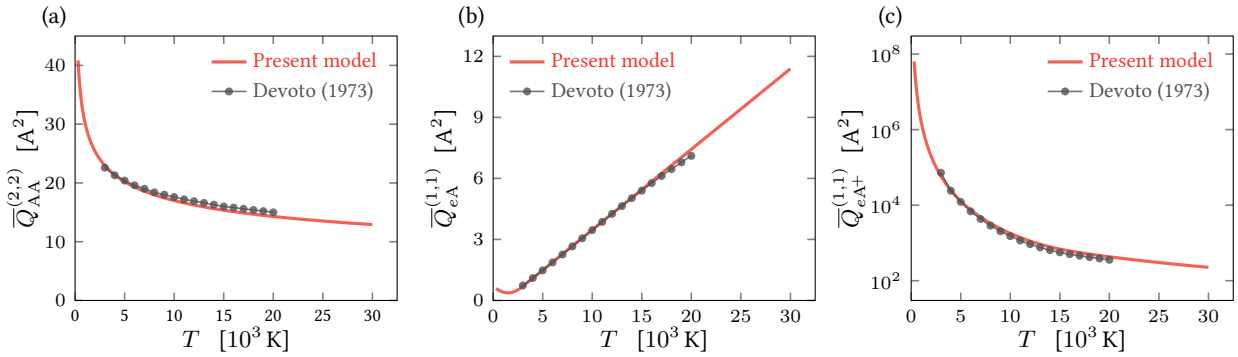

Figure C.1: Comparison of collision integrals with detailed calculations by Devoto [110].

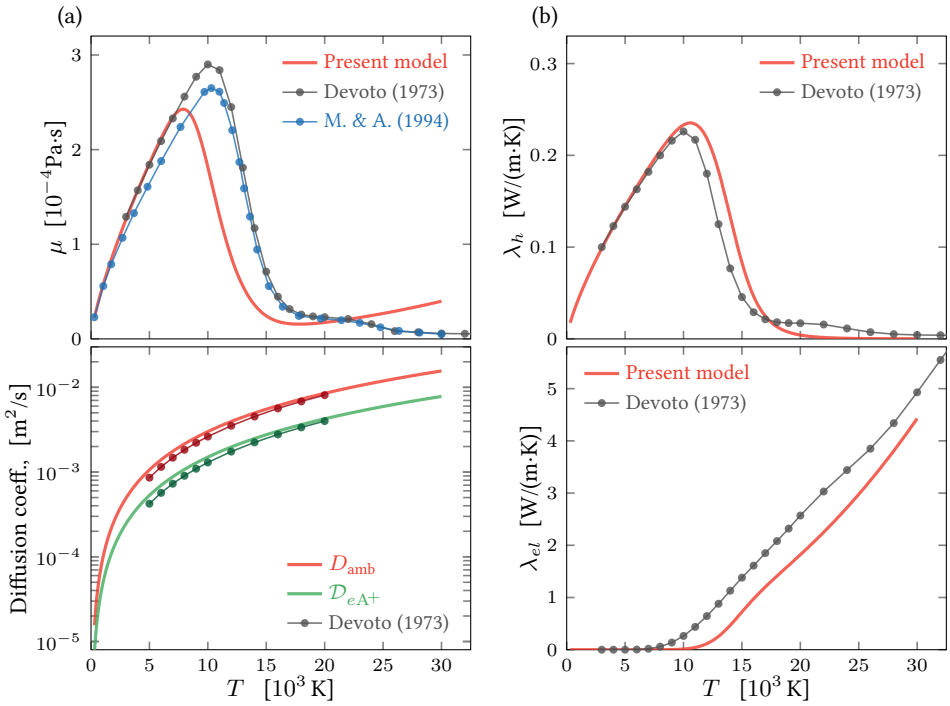

Figure C.2: Comparison of transport properties at equilibrium and atmospheric pressure with detailed calculations by Devoto [110] and Murphy and Arundelli [142], the latter abbreviated in the legend.

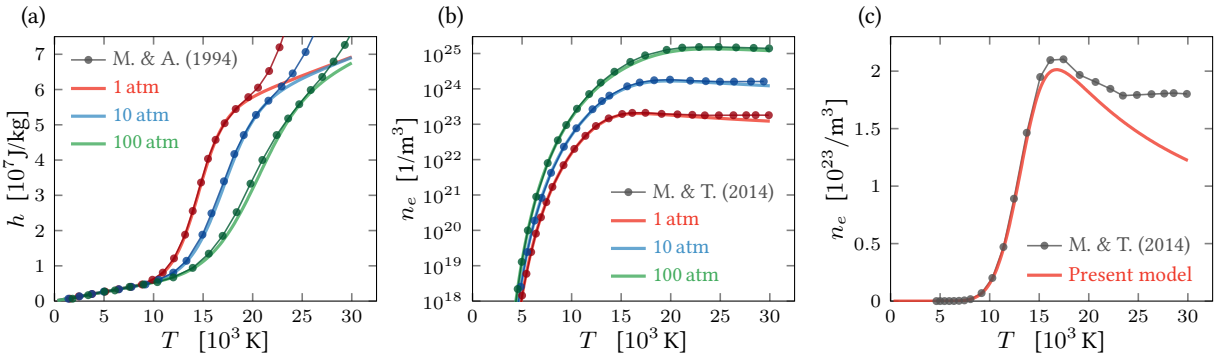

Figure C.3: Comparison of h and n_e at equilibrium with detailed calculations by Murphy and Arundelli [142] and Murphy and Tam [143], abbreviated in the legend. Atmospheric-pressure data of (b) is shown in (c) on a linear scale for clarity.

C.2 Mach 15.9 shock in argon

The reduced nonequilibrium model is compared with the detailed, two-temperature model of Kapper and Cambier [144], which includes photoionization, atom- and electron-impact processes, 31 energy levels for argon, and radiative transitions. The comparison is conducted for a Mach 15.9 shock in $T_\infty = 293.6\,\text{K}$, $p_\infty = 685.3\,\text{Pa}$ argon. As shown in figure C.4(a), there is good agreement in the length of the relaxation region behind the shock front, which results from a competition between thermal relaxation and electron-impact ionization. Though the gradual recombination beyond this region due to radiative loss is clearly not

expected to be reproduced by the reduced model, the electron avalanche in the relaxation zone produces a free-electron spatial distribution which agrees well (figure C.4c). We define the relaxation length as the distance between the shock front and the local minimum of $\partial^2 n_e/\partial x^2$.

The unsteady behavior of the shock — marked by oscillations in its strength due to coupling between gas-dynamic rarefaction waves and the temperature-sensitive ionization avalanche — occurs with a period 31 μs (figure C.5), consistent with 32.5 μs predicted by Kapper and Cambier [145].

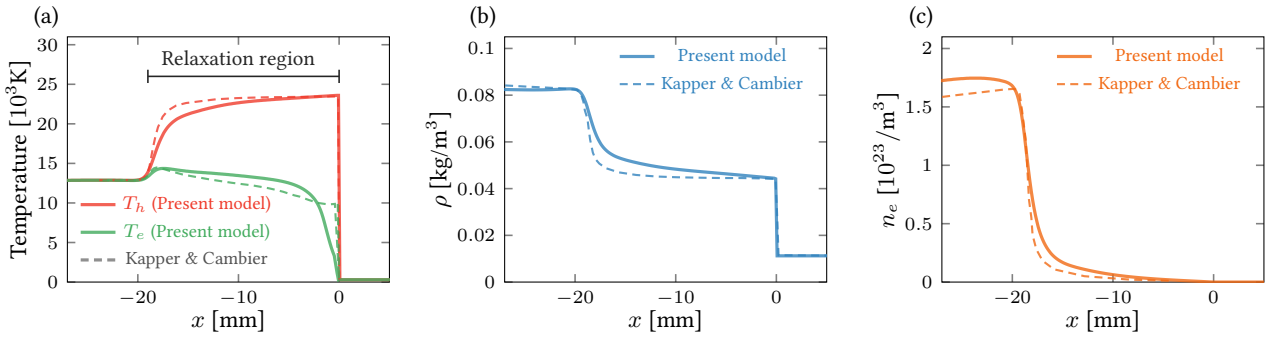

Figure C.4: Comparison of (a) temperatures, (b) density, and (c) electron number density with the detailed model of Kapper and Cambier [144] for a Mach 15.9 shock in argon.

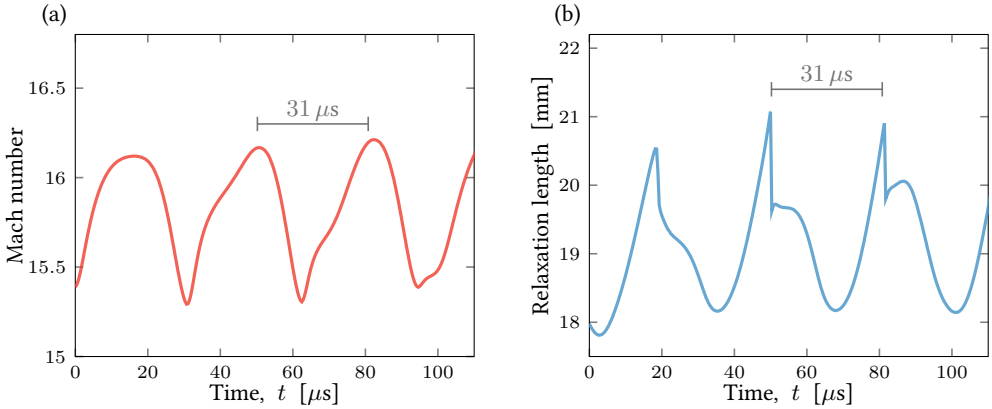

Figure C.5: Time history of (a) Mach number and (b) relaxation length of a Mach 15.9 shock in argon. The period of oscillation is indicated.

C.3 Filter and $X_{e,\infty}$ insensitivity

To verify insensitivity to the filter on $\lambda_{el}\nabla^2 T_e$ (section 5.1.1) and choice of $X_{e,\infty} = 10^{-8}$, we use a one-dimensional spherically symmetric case at $p_\infty = 0.5\,\text{atm}$ and $T_0 = 30\,000\,\text{K}$. Table C.1 summarizes the parameters used, and figure C.6 compares the results at $t = 6.3\,\mu\text{s}$. The data for cases 1 and 2 collapse to plotting accuracy. Case 3 with $X_{e,\infty} = 10^{-12}$ exhibits minor departure from cases 1 and 2 at the perimeter of the kernel, where there is a small peak in T_e. The feature itself does not result from the filter or $X_{e,\infty}$

but coincides with a region with trace electrons, where thermal relaxation with heavy particles is slow, and can lead to discrepancy between T_h and T_e. It is unclear whether this would manifest at these conditions using a more detailed plasma model, though seemingly similar thermal nonequilibrium in cold gas can occur in plasma-arc simulations [146, 147]. An artificial increase in relaxation rate was employed in those cases to suppress this nonequilibrium, though for this work the relaxation rates in (5.6) are unmodified. It is unlikely this small feature affects results: despite the apparent change in T_e at the kernel perimeter, energetically this is a small effect, as only trace electrons are available to carry the electronic energy, which monotonically decreases (figure C.7).

Case	$\lambda_{el}\nabla^2 T_e$ filter	$\mathcal{C}$	$X_{e,\infty}$
1	Yes	8.0	10^{-8}
2	No	0.8	10^{-8}
3	No	0.8	10^{-12}

Table C.1: Cases used to test sensitivity to the filter and $X_{e,\infty}$. For all cases, the mesh spacing is $\Delta r = 1.4\,\mu$m.

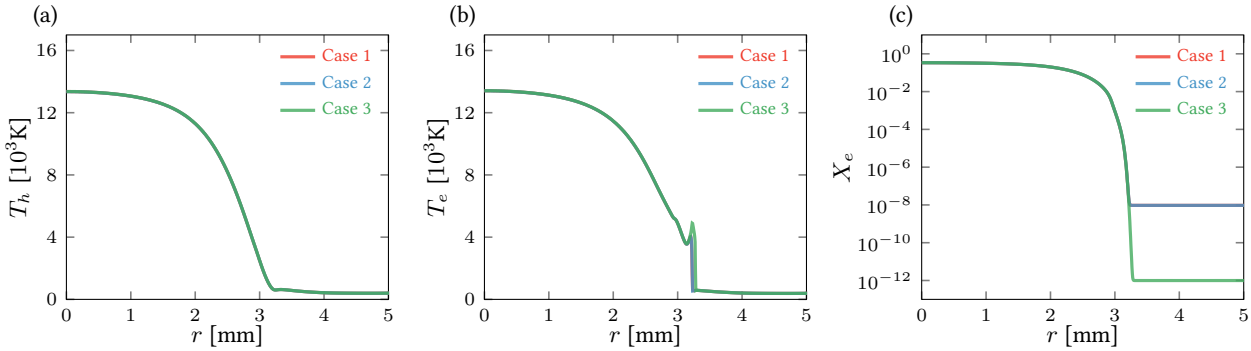

Figure C.6: Comparison at $t = 6.3\,\mu$s of (a) T_h, (b) T_e, and (c) X_e for the cases in table C.1.

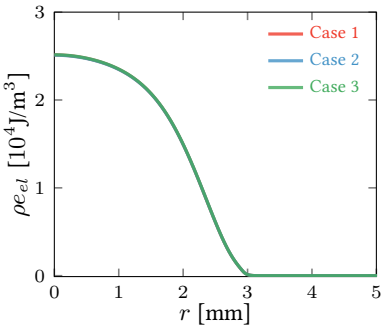

Figure C.7: Comparison at $t = 6.3\,\mu$s of ρe_{el} for the cases in table C.1.

References

[1] R. G. Meyerand and A. F. Haught. Gas breakdown at optical frequencies. *Physical Review Letters*, 11 (9):401, 1963. doi: 10.1103/PhysRevLett.11.401.

[2] C. G. Morgan. Laser-induced breakdown of gases. *Reports on Progress in Physics*, 38(5):621, 1975.

[3] S. S. Harilal, B. E. Brumfield, and M. C. Phillips. Lifecycle of laser-produced air sparks. *Physics of Plasmas*, 22(6):063301, 2015. doi: 10.1063/1.4922076.

[4] J. R. Wilson. Laser-induced multiple breakdown in gases. *Journal of Physics D: Applied Physics*, 3 (12):2005, 1970.

[5] R. Adelgren, G. Elliot, D. Knight, A. Zheltovodov, and T. Beutner. Energy deposition in supersonic flows. In *39th Aerospace Sciences Meeting and Exhibit*, page 885, 2001.

[6] N. G. Glumac and G. S. Elliott. The effect of ambient pressure on laser-induced plasmas in air. *Optics and Lasers in Engineering*, 45(1):27–35, 2007. doi: 10.1016/j.optlaseng.2006.04.002.

[7] N. G. Glumac, G. S. Elliott, and M. Boguszko. Temporal and spatial evolution of a laser spark in air. *AIAA Journal*, 43(9):1984–1994, 2005. doi: 10.2514/1.14886.

[8] A. Munafò, A. Alberti, C. Pantano, J. B. Freund, and M. Panesi. A computational model for nanosecond pulse laser-plasma interactions. *Journal of Computational Physics*, page 109190, 2019. doi: 10.1016/j.jcp.2019.109190.

[9] S. Brieschenk, S. O'Byrne, and H. Kleine. Visualization of jet development in laser-induced plasmas. *Optics Letters*, 38(5):664–666, 2013. doi: 10.1364/OL.38.000664.

[10] P. D. Ronney. Laser versus conventional ignition of flames. *Optical Engineering*, 33(2):510–522, 1994.

[11] P. Kafalas and A. P. Ferdinand. Fog droplet vaporization and fragmentation by a 10.6-μm laser pulse. *Applied Optics*, 12(1):29–33, 1973.

[12] A. L Klein, W. Bouwhuis, C. W. Visser, H. Lhuissier, C. Sun, J. H. Snoeijer, E. Villermaux, D. Lohse, and H. Gelderblom. Drop shaping by laser-pulse impact. *Physical Review Applied*, 3(4):044018, 2015.

[13] S. G. Avila and C.-D. Ohl. Fragmentation of acoustically levitating droplets by laser-induced cavitation bubbles. *Journal of Fluid Mechanics*, 805:551–576, 2016.

[14] Vdw. erena Horneffer, N. Linz, and A. Vogel. Principles of laser-induced separation and transport of living cells. *Journal of Biomedical Optics*, 12(5):054016, 2007.

[15] Y. Tagawa, N. Oudalov, C. W. Visser, I. R. Peters, D. van der Meer, C. Sun, A. Prosperetti, and D. Lohse. Highly focused supersonic microjets. *Physical review X*, 2(3):031002, 2012.

[16] Y. Tagawa, N. Oudalov, A. El Ghalbzouri, C. Sun, and D. Lohse. Needle-free injection into skin and soft matter with highly focused microjets. *Lab on a Chip*, 13(7):1357–1363, 2013.

[17] D. Riggins, H. F. Nelson, and E. Johnson. Blunt-body wave drag reduction using focused energy deposition. *AIAA Journal*, 37(4):460–467, 1999.

[18] R. Kandala and G. V. Candler. Numerical studies of laser-induced energy deposition for supersonic flow control. *AIAA Journal*, 42(11):2266–2275, 2004. doi: 10.2514/1.6817.

[19] R. G. Adelgren, H. Yan, G. S. Elliott, D. D. Knight, T. J. Beutner, and A. A. Zheltovodov. Control of Edney IV interaction by pulsed laser energy deposition. *AIAA Journal*, 43(2):256–269, 2005.

[20] T. X. Phuoc. Laser-induced spark ignition fundamental and applications. *Optics and Lasers in Engineering*, 44(5):351–397, 2006. doi: 10.1016/j.optlaseng.2005.03.008.

[21] M. Kono, K. Niu, T. Tsukamoto, and Y. Ujiie. Mechanism of flame kernel formation produced by short duration sparks. In *Symposium (International) on Combustion*, pages 1643–1649. Elsevier, 1988.

[22] M. Thiele, J. Warnatz, and U. Maas. Geometrical study of spark ignition in two dimensions. *Combustion Theory and Modelling*, 4(4):413–434, 2000.

[23] S. P. M. Bane, J. L. Ziegler, and J. E. Shepherd. Investigation of the effect of electrode geometry on spark ignition. *Combustion and Flame*, 162(2):462–469, 2015.

[24] J. M. Picone and J. P. Boris. Vorticity generation by asymmetric energy deposition in a gaseous medium. *The Physics of Fluids*, 26(2):365–382, 1983. doi: 10.1063/1.864173.

[25] T. A. Spiglanin, A. Mcilroy, E. W. Fournier, R. B. Cohen, and J. A. Syage. Time-resolved imaging of flame kernels: Laser spark ignition of H_2/O_2/Ar mixtures. *Combustion and Flame*, 102(3):310–328, 1995. doi: 10.1016/0010-2180(94)00278-Z.

[26] M. H. Morsy and S. H. Chung. Numerical simulation of front lobe formation in laser-induced spark ignition of CH_4/air mixtures. *Proceedings of the Combustion Institute*, 29(2):1613–1619, 2002.

[27] D. Bradley, C. G. W. Sheppard, I. M. Suardjaja, and R. Woolley. Fundamentals of high-energy spark ignition with lasers. *Combustion and Flame*, 138(1-2):55–77, 2004. doi: 10.1016/j.combustflame.2004.04.002.

[28] S. S. Harilal, G. V. Miloshevsky, P. K. Diwakar, N. L. LaHaye, and A. Hassanein. Experimental and computational study of complex shockwave dynamics in laser ablation plumes in argon atmosphere. *Physics of Plasmas*, 19(8):083504, 2012.

[29] V. Svetsov, M. Popova, V. Rybakov, V. Artemiev, and S. Medveduk. Jet and vortex flow induced by anisotropic blast wave: experimental and computational study. *Shock Waves*, 7(6):325–334, 1997.

[30] L. L. Massa and J. B. Freund. An integrated predictive simulation model for the plasma-assisted ignition of a fuel jet in a turbulent crossflow. In *54th AIAA Aerospace Sciences Meeting*, page 2154, 2016.

[31] J. R. Blake and D. C. Gibson. Cavitation bubbles near boundaries. *Annual Review of Fluid Mechanics*, 19(1):99–123, 1987.

[32] M. S. Plesset and T. P. Mitchell. On the stability of the spherical shape of a vapor cavity in a liquid. *Quarterly of Applied Mathematics*, 13(4):419–430, 1956.

[33] J. M. Picone and J. P. Boris. Vorticity generation by shock propagation through bubbles in a gas. *Journal of Fluid Mechanics*, 189:23–51, 1988.

[34] D. Ranjan, J. Niederhaus, B. Motl, M. Anderson, J. Oakley, and R. Bonazza. Experimental investigation of primary and secondary features in high-mach-number shock-bubble interaction. *Physical Review Letters*, 98(2):024502, 2007.

[35] G. Lacaze, B. Cuenot, T. Poinsot, and M. Oschwald. Large eddy simulation of laser ignition and compressible reacting flow in a rocket-like configuration. *Combustion and Flame*, 156(6):1166–1180, 2009.

[36] S. Brieschenk, S. O'Byrne, and H. Kleine. Laser-induced plasma ignition studies in a model scramjet engine. *Combustion and Flame*, 160(1):145–148, 2013.

[37] L. L. Massa and J. B. Freund. Plasma-combustion coupling in a dielectric-barrier discharge actuated fuel jet. *Combustion and Flame*, 184:208–232, 2017.

[38] N. Gibbons, R. Gehre, S. Brieschenk, and V. Wheatley. Blast wave-induced mixing in a laser ignited hypersonic flow. *Journal of Fluids Engineering*, 140(5):050902, 2018.

[39] R. W. Schmieder. Laser spark ignition and extinction of a methane-air diffusion flame. *Journal of Applied Physics*, 52(4):3000–3003, 1981.

[40] C. Dumitrache, R. VanOsdol, C. M. Limbach, and A. P. Yalin. Control of early flame kernel growth by multi-wavelength laser pulses for enhanced ignition. *Scientific Reports*, 7(1):10239, 2017. doi: 10.1038/s41598-017-10457-0.

[41] H. Torikai, Y. Soga, and A. Ito. Schlieren visualization of blast extinguishment with laser-induced breakdown. *Proceedings of the Combustion Institute*, 36(2):3297–3304, 2017. doi: 10.1016/j.proci.2016.06.131.

[42] J. E. Retter, N. G. Glumac, and G. S. Elliott. XPACC: Stand burner ignition profiles. *Tech. Rep.* University of Illinois at Urbana-Champaign, 2017*a*.

[43] E. Mastorakos. Ignition of turbulent non-premixed flames. *Progress in Energy and Combustion Science*, 35(1):57–97, 2009.

[44] R. Owston and J. Abraham. Flame propagation in stratified hydrogen–air mixtures: Spark placement effects. *International Journal of Hydrogen Energy*, 34(15):6532–6544, 2009.

[45] E. S. Richardson and E. Mastorakos. Numerical investigation of forced ignition in laminar counterflow non-premixed methane-air flames. *Combustion Science and Technology*, 179(1-2):21–37, 2007.

[46] N. Chakraborty, E. Mastorakos, and R. S. Cant. Effects of turbulence on spark ignition in inhomogeneous mixtures: a direct numerical simulation (DNS) study. *Combustion Science and Technology*, 179 (1-2):293–317, 2007.

[47] A. Neophytou, E. Mastorakos, and R. S. Cant. DNS of spark ignition and edge flame propagation in turbulent droplet-laden mixing layers. *Combustion and Flame*, 157(6):1071–1086, 2010.

[48] D. Patel and N. Chakraborty. Localised forced ignition of globally stoichiometric stratified mixtures: A numerical investigation. *Combustion Theory and Modelling*, 18(6):627–651, 2014.

[49] C. Heeger, B. Böhm, S. F. Ahmed, R. Gordon, I. Boxx, W. Meier, A. Dreizler, and E. Mastorakos. Statistics of relative and absolute velocities of turbulent non-premixed edge flames following spark ignition. *Proceedings of the Combustion Institute*, 32(2):2957–2964, 2009.

[50] S. F. Ahmed, R. Balachandran, and E. Mastorakos. Measurements of ignition probability in turbulent non-premixed counterflow flames. *Proceedings of the Combustion Institute*, 31(1):1507–1513, 2007.

[51] M. N. Shneider, A. M. Zheltikov, and R. B. Miles. Tailoring the air plasma with a double laser pulse. *Physics of Plasmas*, 18(6):063509, 2011. doi: 10.1063/1.3601764.

[52] A. A. Tropina, R. B. Miles, and M. N. Shneider. Mathematical model of dual-pulse laser ignition. *Journal of Propulsion and Power*, 34(2):408–414, 2018. doi: 10.2514/1.B36687.

[53] A. Alberti, A. Munafò, C. Pantano, J. B. Freund, and M. Panesi. Collinear dual-pulse laser optical breakdown and energy deposition. *Journal of Physics D: Applied Physics*, 53(20):205202, 2020.

[54] M. S. Bak, L. Wermer, and S. Im. Schlieren imaging investigation of successive laser-induced breakdowns in atmospheric-pressure air. *Journal of Physics D: Applied Physics*, 48(48):485203, 2015. doi: 10.1088/0022-3727/48/48/485203.

[55] B. An, Z. Wang, L. Yang, G. Wu, J. Zhu, and X. Li. Experimental investigation of the shock loss and temporal evolution of hot plume resulting from dual-pulse laser-induced breakdown in quiescent air. *Journal of Applied Physics*, 122(19):193301, 2017. doi: 10.1063/1.4990096.

[56] L. Wermer, S.-K. Im, and M. S. Bak. Schlieren imaging investigation of successive laser-induced breakdowns in air. In *54th AIAA Aerospace Sciences Meeting*, page 0458, 2016. doi: 10.2514/6.2016-0458.

[57] L. Wermer and S.-K. Im. Plasma and flow induced by single- and dual-pulse laser-induced breakdown in stationary air. *Plasma Sources Science and Technology*, 28(6):065004, 2019. doi: 10.1088/1361-6595/ab1cfe.

[58] H. Kojima, E. Takahashi, and H. Furutani. Breakdown plasma and vortex flow control for laser ignition using a combination of nano- and femto-second lasers. *Optics Express*, 22(101):A90–A98, 2013. doi: 10.1364/OE.22.000A90.

[59] C. M. Limbach. *Characterization of Nanosecond, Femtosecond and Dual Pulse Laser Energy Deposition in Air for Flow Control and Diagnostic Applications*. PhD thesis, Princeton University, 2015.

[60] C. Dumitrache and A. P. Yalin. Numerical modeling of the hydrodynamics induced by dual-pulse plasma. In *2018 AIAA Aerospace Sciences Meeting*, page 0689, 2018. doi: 10.2514/6.2018-0689.

[61] L. Wermer, J. Hansson, and S.-K. Im. Dual-pulse laser-induced spark ignition and flame propagation of a methane diffusion jet flame. *Proceedings of the Combustion Institute*, 36(3):4427–4434, 2017. doi: 10.1016/j.proci.2016.07.115.

[62] L. Wermer, J. K. Lefkowitz, T. Ombrello, and S.-K. Im. Ignition enhancement by dual-pulse laser-induced spark ignition in a lean premixed methane-air flow. *Proceedings of the Combustion Institute*, 37(4):5605–5612, 2019. doi: 10.1016/j.proci.2018.06.025.

[63] H. Zhao, N. Zhao, T. Zhang, S. Wu, G. Ma, C. Yan, and Y. Ju. Studies of multi-channel spark ignition of lean n-pentane/air mixtures in a spherical chamber. *Combust. Flame*, 212:337–344, 2020. doi: 10.1016/j.combustflame.2019.11.022.

[64] M. Weinrotter, H. Kopecek, M. Tesch, E. Wintner, M. Lackner, and F. Winter. Laser ignition of ultra-lean methane/hydrogen/air mixtures at high temperature and pressure. *Experimental Thermal and Fluid Science*, 29(5):569–577, 2005. doi: 10.1016/j.expthermflusci.2004.08.002.

[65] N. Pavel, M. Tsunekane, and T. Taira. Composite, all-ceramics, high-peak power Nd: YAG/Cr 4+: YAG monolithic micro-laser with multiple-beam output for engine ignition. *Optics Express*, 19(10): 9378–9384, 2011. doi: 10.1364/OE.19.009378.

[66] E. Lyon, Z. Kuang, H. Cheng, V. Page, T. Shenton, and G. Dearden. Multi-point laser spark generation for internal combustion engines using a spatial light modulator. *Journal of Physics D: Applied Physics*, 47(47):475501, 2014. doi: 10.1088/0022-3727/47/47/475501.

[67] P. S. Hsu, S. Roy, Z. Zhang, J. Sawyer, M. N. Slipchenko, J. G. Mance, and J. R. Gord. High-repetition-rate laser ignition of fuel–air mixtures. *Optics Letters*, 41(7):1570–1573, 2016. doi: 10.1364/OL.41.001570.

[68] S. H. Lee, H. Do, and J. J. Yoh. Simultaneous optical ignition and spectroscopy of a two-phase spray flame. *Combustion and Flame*, 165:334–345, 2016. doi: 10.1016/j.combustflame.2015.12.016.

[69] H. M. Jun, S. W. Suh, and J. J. Yoh. Two-dimensional measurement of hydrocarbon fuel concentration using multiple laser-induced plasma-forming regions. *Optics Express*, 27(4):5144–5153, 2019. doi: 10.1364/OE.27.005144.

[70] A. Alberti, A. Munafò, M. Koll, M. Nishihara, C. Pantano, J. B. Freund, G. S. Elliott, and Marco Panesi. Laser-induced non-equilibrium plasma kernel dynamics. *Journal of Physics D: Applied Physics*, 2020. doi: 10.1088/1361-6463/ab492a.

[71] C. M. Limbach. *Characterization of nanosecond, femtosecond and dual pulse laser energy deposition in air for flow control and diagnostic applications*. PhD thesis, Princeton University, 2015.

[72] M. Nishihara, J. B. Freund, N. G. Glumac, and G. S. Elliott. Influence of mode-beating pulse on laser-induced plasma. *Journal of Physics D: Applied Physics*, 51(13):135601, 2018. doi: 10.1088/1361-6463/aaad87.

[73] A. Alberti, A. Munafò, M. Koll, M. Nishihara, C. Pantano, J. B. Freund, G. S. Elliott, and M. Panesi. Laser-induced non-equilibrium plasma kernel dynamics. *Journal of Physics D: Applied Physics*, 2019.

[74] D. V. Gaitonde and M. R. Visbal. Pade-type higher-order boundary filters for the Navier–Stokes equations. *AIAA Journal*, 38(11):2103–2112, 2000.

[75] S. K. Lele. Compact finite difference schemes with spectral-like resolution. *Journal of Computational Physics*, 103(1):16–42, 1992. doi: 10.1016/0021-9991(92)90324-R.

[76] D. V. Gaitonde and M. R. Visbal. High-order schemes for Navier–Stokes equations: algorithm and implementation into FDL3DI. Technical report, Air Force Research Lab Wright-Patterson AFB OH Air Vehicles Directorate, 1998.

[77] J. Liu and W. Wang. Characterization and regularity for axisymmetric solenoidal vector fields with application to Navier–Stokes equation. *SIAM Journal on Mathematical Analysis*, 41(5):1825–1850, 2009. doi: 10.1137/080739744.

[78] J. B. Freund. Proposed inflow/outflow boundary condition for direct computation of aerodynamic sound. *AIAA Journal*, 35(4):740–742, 1997. doi: 10.2514/2.167.

[79] T. Colonius. Modeling artificial boundary conditions for compressible flow. *Annu. Rev. Fluid Mech.*, 36:315–345, 2004. doi: 10.1146/annurev.fluid.36.050802.121930.

[80] K. W. Thompson. Time-dependent boundary conditions for hyperbolic systems, II. *Journal of Computational Physics*, 89(2):439–461, 1990. doi: 10.1016/0021-9991(90)90152-Q.

[81] T. J. Poinsot and S. K. Lele. Boundary conditions for direct simulations of compressible viscous flows. *Journal of Computational Physics*, 101(1):104–129, 1992.

[82] P. A. Thompson. *Compressible-fluid dynamics*. McGraw-Hill, 1971.

[83] M. D. Koll, G. S. Elliott, and J. B. Freund. Particle image velocimetry of a nano-second laser induced breakdown in air. In *AIAA Scitech 2020 Forum*, pages 2047–2058, 2020.

[84] P. Gregorčič, J. Diaci, and J. Možina. Two-dimensional measurements of laser-induced breakdown in air by high-speed two-frame shadowgraphy. *Applied Physics A*, 112(1):49–55, 2013.

[85] P. J. Archer, T. G. Thomas, and G. N. Coleman. Direct numerical simulation of vortex ring evolution from the laminar to the early turbulent regime. *Journal of Fluid Mechanics*, 598:201–226, 2008.

[86] C. Truesdell. On curved shocks in steady plane flow of an ideal fluid. *Journal of the Aeronautical Sciences*, 19(12):826–828, 1952.

[87] M.J. Lighthill. Dynamics of a dissociating gas part I: equilibrium flow. *Journal of Fluid Mechanics*, 2 (1):1–32, 1957.

[88] W. D. Hayes. The vorticity jump across a gasdynamic discontinuity. *Journal of Fluid Mechanics*, 2 (6):595–600, 1957.

[89] M. P. Friedman. A simplified analysis of spherical and cylindrical blast waves. *Journal of Fluid Mechanics*, 11(1):1–15, 1961.

[90] H. L. Brode. Numerical solutions of spherical blast waves. *Journal of Applied Physics*, 26(6):766–775, 1955.

[91] D. W. Boyer. An experimental study of the explosion generated by a pressurized sphere. *Journal of Fluid Mechanics*, 9(3):401–429, 1960.

[92] Y. Ling and S. Balachandar. Asymptotic scaling laws and semi-similarity solutions for a finite-source spherical blast wave. *Journal of Fluid Mechanics*, 850:674–707, 2018.

[93] C. M. Limbach and R. B. Miles. Rayleigh scattering measurements of heating and gas perturbations accompanying femtosecond laser tagging. *AIAA Journal*, 55(1):112–120, 2017. doi: 10.2514/1.J054772.

[94] C. M. Limbach and R. B. Miles. Characterization of dissociation and gas heating in femtosecond laser plasma with planar Rayleigh scattering and rayleigh scattering polarimetry. In *53rd AIAA Aerospace Sciences Meeting*, page 0932, 2015. doi: 10.2514/6.2015-0932.

[95] C. Butte, P. Lokini, C. Dumitrache, and A. P. Yalin. Single and dual-pulse laser ignition of methane-air and hydrogen-air mixtures. In *AIAA Scitech 2020 Forum*, page 1893, 2020. doi: 10.2514/6.2020-1893.

[96] H. G. Hornung and D. W. Schwendeman. Oblique shock reflection from an axis of symmetry: Shock dynamics and relation to the guderley singularity. *Journal of Fluid Mechanics*, 438:231–245, 2001. doi: 10.1017/S0022112001004360.

[97] V. Hohreiter, J. E. Carranza, and D. W. Hahn. Temporal analysis of laser-induced plasma properties as related to laser-induced breakdown spectroscopy. *Spectrochimica Acta Part B: Atomic Spectroscopy*, 59(3):327–333, 2004. doi: 10.1016/j.sab.2003.12.015.

[98] A. L. Sánchez and F. A. Williams. Recent advances in understanding of flammability characteristics of hydrogen. *Progress in Energy and Combustion Science*, 41:1–55, 2014.

[99] J. P. Appleton and K. N. C. Bray. The conservation equations for a non-equilibrium plasma. *Journal of Fluid Mechanics*, 20(4):659–672, 1964.

[100] J.-H. Lee. Basic governing equations for the flight regimes of aeroassisted orbital transfer vehicles. *Thermal Design of Aeroassisted Orbital Transfer Vehicles*, 96:3–53, 1985.

[101] P. A. Gnoffo, R. N. Gupta, and J. L. Shinn. Conservation equations and physical models for hypersonic air flows in thermal and chemical nonequilibrium. 1989.

[102] M. I. Hoffert and H. Lien. Quasi-one-dimensional, nonequilibrium gas dynamics of partially ionized two-temperature argon. *The Physics of Fluids*, 10(8):1769–1777, 1967.

[103] W. G. Vincenti and C. H. Kruger. Introduction to physical gas dynamics. *John Wlley & Sons, Inc.*, 1965.

[104] A. Kramida, Y. Ralchenko, and J. Reader. *NIST Atomic Spectra Database (version 5.7.1). [Online].* National Institute of Standards and Technology, Gaithersburg MD, 20899. URL `https://doi.org/10.18434/T4W30F`. Accessed on 7/13/2020.

[105] A. Mani, J. Larsson, and P. Moin. Suitability of artificial bulk viscosity for large-eddy simulation of turbulent flows with shocks. *Journal of Computational Physics*, 228(19):7368–7374, 2009.

[106] S. Kawai, S. K. Shankar, and S. K. Lele. Assessment of localized artificial diffusivity scheme for large-eddy simulation of compressible turbulent flows. *Journal of Computational Physics*, 229(5):1739–1762, 2010.

[107] R. J. Kee, M. E. Coltrin, and P. Glarborg. *Chemically reacting flow: theory and practice*. John Wiley & Sons, 2005.

[108] R. S. Devoto. Simplified expressions for the transport properties of ionized monatomic gases. *The Physics of Fluids*, 10(10):2105–2112, 1967.

[109] R. N. Gupta, J. M. Yos, R. A. Thompson, and K.-P. Lee. A review of reaction rates and thermodynamic and transport properties for an 11-species air model for chemical and thermal nonequilibrium calculations to 30000 k. 1990.

[110] R. S. Devoto. Transport coefficients of ionized argon. *The Physics of Fluids*, 16(5):616–623, 1973.

[111] Y. Enomoto. Wall boundary layer effects on ionizing shock structure in argon. *Journal of the Physical Society of Japan*, 35(4):1228–1233, 1973.

[112] I. I. Glass and W. S. Liu. Effects of hydrogen impurities on shock structure and stability in ionizing monatomic gases. part 1. argon. *Journal of Fluid Mechanics*, 84(1):55–77, 1978.

[113] W. S. Liu, B. T. Whitten, and I. I. Glass. Ionizing argon boundary layers. part 1. quasi-steady flat-plate laminar boundary-layer flows. *Journal of Fluid Mechanics*, 87(4):609–640, 1978.

[114] A. Fridman and L. A. Kennedy. *Plasma Physics and Engineering (2nd ed.)*. CRC press, 2015.

[115] R. S. Devoto. Transport properties of ionized monatomic gases. *Physics of Fluids*, 9(6):1230–1240, 1966.

[116] Y.B. Zeldovich and Y.P. Raizer. *Physics of Shock Waves and High-temperature Hydrodynamic Phenomena*. Number v. 1. Academic Press, 1966.

[117] Ş Yalçin, DR Crosley, GP Smith, and Gregory W Faris. Influence of ambient conditions on the laser air spark. *Applied Physics B: Lasers and Optics*, 68(1):121–130, 1999.

[118] F. M. White. *Viscous fluid flow*, volume 3. McGraw-Hill, Inc., 2 edition, 1991.

[119] J. B. Freund. *Compressibility effects in a turbulent annular mixing layer*. PhD thesis, 1997.

[120] S. Brieschenk, S. O'Byrne, and H. Kleine. Ignition characteristics of laser-ionized fuel injected into a hypersonic crossflow. *Combustion and Flame*, 161(4):1015–1025, 2014.

[121] Joseph O Hirschfelder, Charles F Curtiss, and Robert Byron Bird. *Molecular theory of gases and liquids*. John Wiley & Sons, Inc., 1967.

[122] T. Poinsot and D. Veynante. *Theoretical and numerical combustion*. RT Edwards, Inc., 2005.

[123] B. J. McBride, M. J. Zehe, and S. Gordon. Nasa glenn coefficients for calculating thermodynamic properties of individual species. 2002.

[124] David G. Goodwin, Raymond L. Speth, Harry K. Moffat, and Bryan W. Weber. Cantera: An object-oriented software toolkit for chemical kinetics, thermodynamics, and transport processes. `https://www.cantera.org`, 2018. Version 2.3.0.

[125] W. G. Lindstrom, P. J. and. Mallard. *NIST Chemistry WebBook, NIST Standard Reference Database Number 69*. National Institute of Standards and Technology, Gaithersburg MD, 20899. URL `https://doi.org/10.18434/T4D303`. Accessed on 6/11/2020.

[126] K. K. Kuo. *Principles of Combustion*. John Wiley & Sons, Inc., 2 edition, 2005.

[127] J. C Sutherland and C. A. Kennedy. Improved boundary conditions for viscous, reacting, compressible flows. *Journal of Computational Physics*, 191(2):502–524, 2003.

[128] M. Matalon. Intrinsic flame instabilities in premixed and nonpremixed combustion. *Annu. Rev. Fluid Mech.*, 39:163–191, 2007.

[129] J. F. MacArt, J. M. Wang, P. P. Popov, and J. B. Freund. Detailed simulation of ignition, flame acceleration, and instability transition following a laser-induced breakdown. *Proceedings of the Combustion Institute*, 2020. (In review).

[130] H. G. Im, J. H. Chen, and C. K. Law. Ignition of hydrogen-air mixing layer in turbulent flows. In *Symposium (International) on Combustion*, volume 27, pages 1047–1056. Elsevier, 1998.

[131] T. P. Coffee, A. J. Kotlar, and M. S. Miller. The overall reaction concept in premixed, laminar, steady-state flames. I. stoichiometries. *Combustion and Flame*, 54(1-3):155–169, 1983.

[132] R. W. Bilger. The structure of turbulent nonpremixed flames. In *Symposium (International) on Combustion*, volume 22, pages 475–488. Elsevier, 1988.

[133] R. Hilbert and D. Thévenin. Autoignition of turbulent non-premixed flames investigated using direct numerical simulations. *Combustion and Flame*, 128(1-2):22–37, 2002.

[134] S. Ghosh and K. Mahesh. Numerical simulation of the fluid dynamic effects of laser energy deposition in air. *Journal of Fluid Mechanics*, 605:329–354, 2008. doi: 10.1017/S0022112008001468.

[135] S. Ghosh and K. Mahesh. DNS of the thermal effects of laser energy deposition in isotropic turbulence. *Journal of Fluid Mechanics*, 654:387–416, 2010. doi: doi:10.1017/S0022112010000649.

[136] Wolfram Research Inc. Mathematica. *Wolfram Research, Inc., Champaign, Illinois*, 2020. URL `https://www.wolfram.com/mathematica`.

[137] C.-W. Shu and S. Osher. Efficient implementation of essentially non-oscillatory shock-capturing schemes, II. In *Upwind and High-Resolution Schemes*, pages 328–374. Springer, 1989.

[138] E. F. Toro. *Riemann solvers and numerical methods for fluid dynamics: a practical introduction*. Springer Science & Business Media, 2013.

[139] B. J. McBride, S. Gordon, and M. A. Reno. Coefficients for calculating thermodynamic and transport properties of individual species. 1993.

[140] P. Boivin, C. Jiménez, A. L. Sánchez, and F. A. Williams. An explicit reduced mechanism for h2–air combustion. *Proceedings of the Combustion Institute*, 33(1):517–523, 2011.

[141] A. W. Cook. Enthalpy diffusion in multicomponent flows. *Physics of Fluids*, 21(5):055109, 2009.

[142] A. B. Murphy and C. J. Arundelli. Transport coefficients of argon, nitrogen, oxygen, argon-nitrogen, and argon-oxygen plasmas. *Plasma Chemistry and Plasma Processing*, 14(4):451–490, 1994.

[143] A. B. Murphy and E. Tam. Thermodynamic properties and transport coefficients of arc lamp plasmas: argon, krypton and xenon. *Journal of Physics D: Applied Physics*, 47(29):295202, 2014.

[144] M. G. Kapper and J.-L. Cambier. Ionizing shocks in argon. Part I: Collisional-radiative model and steady-state structure. *Journal of Applied Physics*, 109(11):113308, 2011.

[145] M. G. Kapper and J.-L. Cambier. Ionizing shocks in argon. Part II: Transient and multi-dimensional effects. *Journal of Applied Physics*, 109(11):113309, 2011.

[146] J. Haidar. Non-equilibrium modelling of transferred arcs. *Journal of Physics D: Applied Physics*, 32 (3):263, 1999.

[147] J. P. Trelles, J. V. R. Heberlein, and E. Pfender. Non-equilibrium modelling of arc plasma torches. *Journal of Physics D: Applied Physics*, 40(19):5937, 2007.